

TECHNISCHE UNIVERSITÄT MÜNCHEN

MAX-PLANCK-INSTITUT FÜR PHYSIK

**Low-Threshold Detectors for
Low-Mass Direct Dark Matter
Search with CRESST-III**

DISSERTATION

VON

ANJA TANZKE

TECHNISCHE UNIVERSITÄT MÜNCHEN

MAX-PLANCK-INSTITUT FÜR PHYSIK
Werner-Heisenberg-Institut

**Low-Threshold Detectors for Low-Mass Direct Dark Matter
Search with CRESST-III**

Anja Tanzke

Vollständiger Abdruck der von der Fakultät für Physik der Technischen Universität München zur Erlangung des akademischen Grades eines

Doktors der Naturwissenschaften (Dr. rer. nat.)

genehmigten Dissertation.

Vorsitzender: Univ.-Prof. Dr. Alejandro Ibarra

Prüfer der Dissertation: 1. Hon.-Prof. Allen Caldwell, Ph.D.
2. Univ.-Prof. Dr. Stefan Schönert

Die Dissertation wurde am 24.11.2016 bei der Technischen Universität München eingereicht und durch die Fakultät für Physik am 25.01.2017 angenommen.

Abstract

There is compelling evidence for the existence of dark matter which exceeds the amount of baryonic matter in our universe by a factor of ~ 5 (see chapter 1). Despite large experimental efforts in the last decades, the nature of dark matter has not yet been revealed.

The CRESST experiment is one of several experiments that aim for directly detecting dark matter particles via elastic scattering off nuclei in a target material. CRESST uses scintillating CaWO_4 single crystals with a mass of 24–300 g as target material. The dedicated experimental setup that is necessary to operate the sensitive detectors in a low-background environment, is described in chapter 2. For the detection of the temperature rise caused by an energy deposition, every crystal is equipped with a sensitive thermometer made of a transition edge sensor (TES). Each of these phonon detectors is paired with a light detector based on the same technique, which allows to measure the scintillation light in addition to the phonon signal. Both detectors are surrounded by a reflective and scintillating housing. Together this unit forms a detector module. Different types of particle interactions produce a different amount of scintillation light. Therefore, the simultaneous operation of phonon and light detectors allows for an active background discrimination on an event-by-event basis.

The previous data taking phase of the experiment, denoted as CRESST-II phase 2 (2013–2015), successfully operated detectors with a crystal mass of 250–300 g. Low energy thresholds down to 307 eV allowed to explore new parameter space for elastic spin-independent dark matter particle-nucleon interaction down to $\sim 0.5 \text{ GeV}/c^2$. For dark matter particle masses smaller than $\sim 1.7 \text{ GeV}/c^2$ a world leading exclusion limit has been set.

In chapter 3 the dominant parameters for the sensitivity of the CRESST experiment in particular in the low-mass region are investigated. It is found that the background level and the exposure play a minor role only, while a reduction of the energy threshold of the phonon detector can drastically increase the sensitivity for low-mass dark matter. For this reason, the CRESST collaboration aims at operating phonon detectors with a threshold for recoiling nuclei of $< 100 \text{ eV}$. This new stage of the experiment, named CRESST-III, is dedicated to explore the low-mass dark matter region.

The goal of the present work is the optimization of the CRESST-II detectors for CRESST-III. Therefore, a detailed understanding of the detector physics is necessary. The model describing the evolution of the signal in the detector as well as the noise sources relevant for the detectors are reviewed in chapter 4. The noise level observed with a phonon detector in different setups is investigated and compared. While the noise is strongly influenced by the rate observed in the respective setup, the signal is in good assumption independent of the setup. This allows to infer the expected performance in the main CRESST setup from a measurement in a test setup above ground.

To achieve the goal of a phonon detector threshold of $< 100 \text{ eV}$ it is aimed for an increase of the signal height in order to enhance the signal-to-noise ratio. A reduction of the crystal mass to 24 g accompanied by an optimization of the crystal geometry increases the signal of the phonon detector (see chapter 5). Moreover, the TES structure

needs to be adapted to the new crystal geometry to achieve the desired increase of the signal level. In the present work different TES structures are developed and compared. With an adaptation of the light detector to the size of the crystal it is expected to improve the light detector performance further.

A change of the crystal geometry requires an adjustment of the housing (see chapter 6). In the new design, the crystal as well as the light detector are held by scintillating CaWO_4 sticks which are pressed against the detectors by bronze clamps located outside of the module housing. In this way, the design features a fully-scintillating inner detector housing. However, due to the low threshold of the phonon detector, α -induced recoil events on the surface of the sticks extending outside the housing can cause an additional background in the region of interest. To prevent this, each of the three phonon detector holding sticks is equipped with a TES. With the resulting signal energy depositions in the sticks can be vetoed efficiently. These instrumented sticks are referred to as iSticks and they are operated in parallel in one readout circuit.

Measurements with prototype modules in a test setup in Munich allowed to determine the detector performance of all three channels (phonon detector, light detector and iSticks, see chapter 7). Two different phonon detectors have been tested above ground and threshold values of $E_{thr} = 136 \text{ eV}$ and $E_{thr} = 195 \text{ eV}$ have been reached. Considering the lower noise conditions in the main CRESST setup compared to the test setup it is expected that thresholds of 16–60 eV are in reach. Also the light detector and the iSticks were operated successfully in the test measurements and their performance is evaluated. The threshold of the iStick channel has been verified being low enough to veto all events occurring in the sticks.

Suggestions for additional future investigations and improvements are discussed in chapter 8. Due to the promising results obtained in the present work, ten such modules have been installed in the main CRESST setup. CRESST-III has started recently with the potential to increase the sensitivity in the low-mass dark matter region by more than four orders of magnitude and to explore masses down to $\sim 0.1 \text{ GeV}/c^2$.

Zusammenfassung

Es gibt überzeugende Beweise für die Existenz von dunkler Materie, welche die Menge baryonischer Materie in unserem Universum etwa um einen Faktor fünf überschreitet (siehe Kapitel 1). Trotz großer experimenteller Anstrengungen in den letzten Jahrzehnten, konnte die Frage nach der Natur dunkler Materie noch nicht geklärt werden.

Das CRESST Experiment ist eines von mehreren Experimenten, die anstreben dunkle Materie mittels elastischer Kernrückstöße in einem Targetmaterial direkt nachzuweisen. CRESST verwendet als Targetmaterial szintillierende CaWO_4 -Einkristalle mit einer Masse von 24–300 g. Der experimentelle Aufbau, der notwendig ist, um die empfindlichen Detektoren in einer Umgebung mit niedriger Untergrundrate zu betreiben, ist in Kapitel 2 beschrieben. Um die Temperaturerhöhung, die durch eine Energiedeposition verursacht wird, nachzuweisen, ist jeder Kristall mit einem empfindlichen Thermometer, bestehend aus einem Phasenübergangsthermometer (TES), ausgestattet. Jeder dieser Phonondetektoren ist mit einem Lichtdetektor, der auf dem gleichen Prinzip beruht, paarweise zusammengefügt. Dieser erlaubt neben dem Phononsignal das Szintillationslicht zu messen. Beide Detektoren sind von einem reflektierenden und szintillierenden Gehäuse umgeben. Diese Einheit bildet zusammen ein Detektormodul. Wechselwirkungen verschiedener Teilchen produzieren eine unterschiedliche Menge Szintillationslicht. Daher erlaubt das gleichzeitige Betreiben des Phonon- und des Lichtdetektors eine aktive Untergrundunterscheidung für jedes einzelne Ereignis.

In der vorherigen Phase des Experiments (Datennahme von 2013-2015), welche als CRESST-II Phase 2 bezeichnet wird, wurden Detektoren mit einer Masse von 250–300 g betrieben. Niedrige Energieschwellen von bis zu 307 eV ermöglichten es neuen Parameterraum für elastische spinunabhängige Kernrückstöße von dunkler Materie bis hinab zu Massen von $\sim 0.5 \text{ GeV}/c^2$ zu untersuchen. Zudem wurde ein weltweit führendes Ausschlusslimit für dunkle Materie mit einer Masse von unter $\sim 1.7 \text{ GeV}/c^2$ gesetzt.

In Kapitel 3 werden die Parameter, welche die Sensitivität des CRESST Experiments insbesondere im Bereich niedriger Massen dominieren, untersucht. Dabei wird beobachtet, dass das Untergrundniveau und die Exposition eine untergeordnete Rolle spielen, während die Reduktion der Energieschwelle des Phonondetektors die Sensitivität für dunkle Materie mit niedriger Masse drastisch erhöht. Aus diesem Grund beabsichtigt die CRESST Kollaboration Phonondetektoren mit einer Energieschwelle für Kernrückstöße von $< 100 \text{ eV}$ in einer neuen Stufe des Experiments (CRESST-III) zu betreiben, um den Parameterbereich für dunkle Materie mit niedrigen Massen zu untersuchen.

Ziel dieser Arbeit ist die Optimierung der CRESST-II Detektoren für CRESST-III. Dafür ist ein eingehendes Verständnis der Detektorphysik notwendig. Über das Modell, das die Entwicklung des Signals im Detektor beschreibt, sowie die relevanten Rauschquellen wird in Kapitel 4 ein Überblick gegeben. Das Rauschen, das mit Phonondetektoren in verschiedenen experimentellen Aufbauten beobachtet wird, wird untersucht und verglichen. Während das Rauschen stark von der Rate im jeweiligen Aufbau beeinflusst wird, ist die Signalhöhe näherungsweise unabhängig davon. Daher ist es möglich,

von einer Messung im Testaufbau, der sich über Tage befindet, auf die erwartete Performance im CRESST Hauptaufbau zu schließen.

Um das Ziel einer Phonondetektorschwelle von < 100 eV zu erreichen, wird eine Vergrößerung der Signalhöhe angestrebt, um dadurch das Signal-Rausch-Verhältnis zu erhöhen. Mit einer Reduzierung der Kristallmasse auf 24 g einhergehend mit einer Optimierung der Geometrie kann die Signalhöhe des Phonondetektors vergrößert werden (siehe Kapitel 5). Darüber hinaus muss die TES-Struktur an die neue Kristallgeometrie angepasst werden, um die gewünschte Erhöhung des Signals zu erreichen. Verschiedene TES-Strukturen werden im Rahmen dieser Arbeit entwickelt und verglichen. Durch eine Anpassung des Lichtdetektors an die Kristallgröße wird auch eine Verbesserung der Lichtdetektor-Performance erwartet.

Das Gehäuse muss ebenfalls an die neue Kristallgeometrie angepasst werden (siehe Kapitel 6). In dem neuen Design werden sowohl der Kristall als auch der Lichtdetektor von szintillierenden CaWO_4 -Stäbchen gehalten. Diese Stäbchen werden von Bronzeclammern außerhalb des Gehäuses gegen die Detektoren gedrückt. Damit ist dieses Modul mit einem vollständig szintillierendem inneren Gehäuse ausgestattet. Aufgrund der niedrigen Schwelle des Phonondetektors können allerdings α -induzierte Ereignisse auf der Oberfläche der Stäbchen, die aus dem Gehäuse herausragen, zusätzlichen Untergrund erzeugen. Um dies zu verhindern ist jedes der drei Haltestäbchen des Phonondetektors mit einem TES ausgestattet. Mit dem resultierenden Signal können Energiedepositionen in den Stäbchen effektiv unterschieden werden. Diese instrumentierten Stäbchen werden als iSticks bezeichnet und in einem Auslesestromkreis parallel betrieben.

Mit Messungen von Prototypen des Modules in einem Testaufbau in München war es möglich die Detektorperformance aller drei Kanäle (Phonondetektor, Lichtdetektor und iSticks) zu bestimmen (siehe Kapitel 7). Zwei verschiedenen Phonondetektoren wurden in einem Testaufbau, welcher sich über Tage befindet, gemessen und Energieschwellen von $E_{thr} = 136$ eV und $E_{thr} = 195$ eV wurden erreicht. Aufgrund der im Vergleich zum Testaufbau besseren Rauschbedingungen wird erwartet im Hauptaufbau von CRESST Schwellen von 16–60 eV zu erreichen. Der Lichtdetektor und die iSticks wurden in diesen Testmessungen ebenfalls erfolgreich betrieben und ihre Performance wurde analysiert. Die Schwelle des iStick-Kanals war niedrig genug, um alle Ereignisse, die sich in den Stäbchen ereigneten, zu unterscheiden.

Vorschläge für zukünftige Untersuchungen und Verbesserungen werden in Kapitel 8 diskutiert. Aufgrund der vielversprechenden Resultate dieser Arbeit wurden zehn dieser Module im Hauptaufbau von CRESST eingebaut. CRESST-III startete kürzlich und besitzt das Potential die Sensitivität im Bereich leichter dunkler Materie um mehr als vier Größenordnungen zu erhöhen und Massen bis hinab zu ~ 0.1 GeV/ c^2 zu untersuchen.

Contents

1	Dark Matter	1
1.1	Evidence for Dark Matter	1
1.1.1	Rotation Curves of Galaxies	1
1.1.2	Galaxy Clusters	2
1.1.3	Cosmic Microwave Background	3
1.1.4	Structure Formation	4
1.2	Candidates for Dark Matter	5
1.2.1	Weakly Interacting Massive Particles	6
1.2.2	Asymmetric Dark Matter	6
1.3	Methods for the Detection of Dark Matter	7
1.4	Direct Detection of Dark Matter	9
1.4.1	Detection Rates and Energy Spectrum	9
1.4.2	Detector Effects	12
1.4.3	Experimental Requirements and Signatures	14
1.4.4	Experimental Techniques for Direct Dark Matter Search	14
2	The CRESST Experiment	19
2.1	Experimental Setup	19
2.1.1	Background Reduction	19
2.1.2	Cryostat and Experimental Volume	22
2.2	Cryogenic CRESST Detectors	23
2.2.1	Cryogenic Calorimeter	23
2.2.2	Transition Edge Sensors	24
2.2.3	Detector Module	25
2.3	Active Background Discrimination	27
2.3.1	Light-Phonon Technique	28
2.3.2	Surface Background Discrimination	32
2.4	Data Taking	34
2.4.1	SQUID-based Readout	34
2.4.2	Detector Operation and Data Acquisition	34
2.5	Basic Concepts of Data Analysis	37
2.5.1	Pulse Height Evaluation	37
2.5.2	Energy Calibration	39
2.5.3	Cuts	40
2.6	Status and Future Strategy of the CRESST experiment	41
2.6.1	CRESST-II Phase 2	41
2.6.2	Future Strategy of CRESST-III	45

3	Sensitivity Projections for CRESST-III	47
3.1	Method and Assumptions	47
3.2	Impact of Relevant Parameters	50
3.2.1	Exposure	50
3.2.2	Background	52
3.2.3	Threshold	52
3.3	Future Potential of CRESST-III	54
4	Detector Model	59
4.1	Components of the Detector Module	59
4.1.1	Phonon Detector	59
4.1.2	Light Detector	60
4.2	Thermal Model of the Detector	61
4.2.1	Heat Capacities	62
4.2.2	Non-thermal and Thermal Phonons	63
4.2.3	Thermal Couplings	64
4.2.4	Model Assumptions	67
4.2.5	Signal Formation	69
4.2.6	Electrothermal Feedback	73
4.2.7	Phonon Collectors	74
4.3	Noise	75
4.3.1	Noise Sources	75
4.4	Measured Noise Contribution	79
4.4.1	Baseline Noise	79
4.4.2	Measured Noise Spectra	79
4.5	Signal-to-Noise Ratio and Threshold	82
5	Detector Optimization for Low-Mass Dark Matter	85
5.1	Absorber Crystal	85
5.1.1	Influence of the Absorber Crystal Geometry on the Signal Height	85
5.1.2	Optimized Crystal Geometry for a Large Signal	88
5.2	Phonon Detector Thermometer	89
5.2.1	TES Structure for a Detector Operated in Bolometric Mode	89
5.2.2	TES Structure for a Detector Operated in Calorimetric Mode	90
5.2.3	Operation Mode for the Phonon Detector with a small Crystal	92
5.3	Implications for the Light Channel	92
5.3.1	Light Output of the Crystal	93
5.3.2	Light Detector Geometry	93
6	The CRESST-III Low-Mass Dark Matter Detector Module	95
6.1	Detectors	95
6.2	Detector Holder Concept	96
6.2.1	Requirements for the Detector Holder	96
6.2.2	Fully-Scintillating Housing	97
6.3	Instrumented Holding Sticks	99
6.3.1	Realization	100

6.3.2	Readout Scheme	102
7	First Measurements with a Prototype Module	105
7.1	Measurements and Data Analysis	105
7.2	Phonon Detector Performance	106
7.2.1	Calorimetric Detector Operation	107
7.2.2	Energy Threshold	109
7.2.3	Thermalization of Non-Thermal Phonons	110
7.2.4	Thermometer Area	115
7.3	Light Detector Performance	115
7.4	iStick Channel	118
7.4.1	Setup of the iStick Channel	118
7.4.2	Signal of the iStick Channel	119
7.4.3	Energy Threshold and Resolution of the iStick Channel	120
7.4.4	Discrimination of Events Occurring in the iSticks	122
7.4.5	Light Signal of Stick Events	124
7.4.6	Discrimination of the individual iSticks	125
7.4.7	Light Detector Holding Sticks	129
7.5	Summary	130
8	Conclusion and Perspectives	133
A	Baseline Noise Determined with Artificial Pulses	139
B	Parametrization of the Recoil Bands	141

Chapter 1

Dark Matter

From astronomical observations there is evidence that most of the matter density in the Universe is made up of non-luminous matter that at least interacts gravitationally, the so-called dark matter. These observations exclude that dark matter consists of baryons or other known particles. It was shown that dark matter accounts for about five times more energy than the known baryonic matter in the Universe [1].

Dark matter influenced the Universe on all time scales, from the big bang nucleosynthesis up to the present time. Therefore, it can be found on all astronomical length scales from galaxies and clusters up to cosmic scales. The properties of dark matter determine how the Universe evolved and what its structure looks like today. Different observations give a consistent picture of the influence of dark matter on the Universe and allow to infer on its properties and give constraints on them.

Some examples for observations of dark matter and the conclusions that have been drawn from them are discussed in section 1.1. However, from these observations not enough information can be gathered to identify the nature of the particles that make up dark matter. At the same time there are theories for new particles that can solve problems arising in the standard model of particle physics and that need new physics beyond the standard model. Some of these proposed particles have properties that also fulfill the constraints on dark matter and, therefore, are considered as dark matter candidates (see section 1.2). Numerous experiments try to detect dark matter with different techniques (see section 1.3). One approach is the direct detection of dark matter, which is discussed in section 1.4.

1.1 Evidence for Dark Matter

In 1933 Fritz Zwicky observed that the velocity distribution of galaxies in the Coma cluster cannot be explained solely by the luminous matter [2]. This was one of the first indications for the existence of dark matter. Since then, numerous observations were made that provide overwhelming evidence for dark matter.

1.1.1 Rotation Curves of Galaxies

The smallest length scales where direct evidence for dark matter can be observed are individual galaxies. The measurement of rotation curves which describe the orbital velocity of stars around the galactic center as a function of their distance r from the galactic center, gives hints about the presence of a mass component in addition to the luminous matter. The measured rotation curves show discrepancies with respect to the

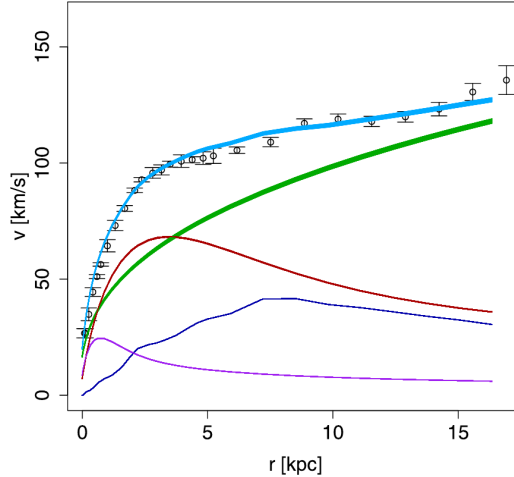


Figure 1.1: Rotation curve of the spiral galaxy M33. The observed velocity distribution of the stars is shown by black data points [3]. The expected contribution from the observed luminous matter is shown in purple for the inner stellar component, red for the the outer stellar component, and dark blue for the gas contribution. The best fit to the data points is shown in light blue and results in contribution of dark matter (green) that is needed to explain to the measured rotation curve. Image taken from [4].

expectations based on the observations of luminous matter. In spiral galaxies most of the luminous mass is clustered in the central bulge of the galaxy. Outside of it the velocities of stars are expected to fall off with $v \sim 1/\sqrt{r}$, which is in contrast to the observations.

As an example, the rotation curve of the spiral galaxy M33 is shown in figure 1.1. The measurement of the rotation curves (e.g. performed by measuring the Doppler shift of the 21 cm line of hydrogen) is shown by black data points [3]. It can be seen that the rotation curve remains flat also for large radii. Consequently, the rotation curve can only be explained by an additional contribution from dark matter in form of a large halo around the galaxy. From a fit of the data the distributions of the different mass components can be extracted. This shows that dark matter has the largest contribution to the velocities for large radii, which allows to deduce the mass distribution of dark matter. The measured rotation curve can only be explained with dark matter forming a large halo around the luminous matter.

1.1.2 Galaxy Clusters

Observations of galaxy clusters also hint to the existence of an additional dark matter component. A direct observational evidence for dark matter was found in the Bullet Cluster, which actually consists of two galaxy clusters that collided ~ 100 Myr ago [5]. In a collision of galaxy clusters the stars in the galaxies pass through each other collisionless, while the intracluster plasma is slowed down due to friction. Thereby, the plasma was heated up which allows to measure its distribution via X-ray emission. A typical galaxy cluster contains much more mass in the form of gas than stars. Thus,

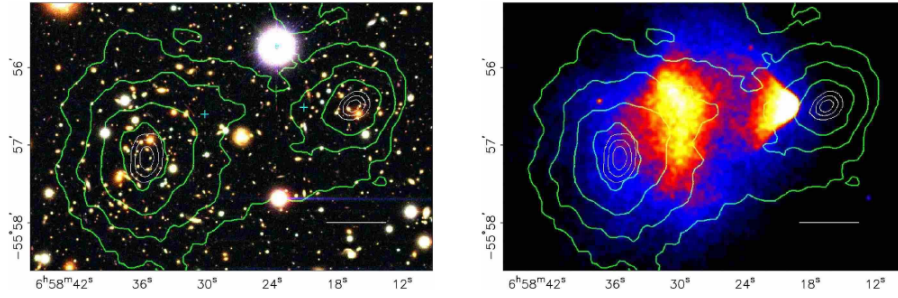


Figure 1.2: An optical image of the Bullet Cluster is shown in the left picture, with the white bar indicating a length of 200 kpc at the distance of the cluster. The right image shows the X-rays emitted by the intracluster plasma. The gravitational potential is shown as overlaid green contours in both images. It can be seen that the gravitational potential is spatially coincident with the galaxies, but not with the plasma. Image taken from [5].

it is expected that the location of the center of mass is coincident with the location of the gas.

In figure 1.2 an optical picture of the Bullet Cluster (left image) and an image of the X-rays emitted by the plasma (right image) are shown. As expected, the plasma spatially decoupled from the galaxies and was left behind during the collision. Additionally, the gravitational potential was measured with weak gravitational lensing, which measures the distortions of images of background galaxies caused by the gravitational deflection of light due to the cluster's mass. The gravitational potential is visualized by green contours overlaid in both images. It can be seen that it is overlapping with the distribution of visible galaxies but not with the plasma.

Since the gravitational potential is spatially coincident with the galaxies but not with the plasma, an even more massive component must be present in the cluster, that cannot be seen and is hardly interacting. This is another evidence for dark matter and was observed in several other merging galaxy clusters [6].

1.1.3 Cosmic Microwave Background

About 380,000 years after the Big Bang electrons and protons combined to form neutral hydrogen and the Universe became transparent for photons. The photons from this time are still observable today as the cosmic microwave background (CMB) and form a perfect black body spectrum with today's temperature of $T = (2.72548 \pm 0.00057)$ K [8]. The spectrum of the CMB is uniform over the whole sky with only tiny fluctuations of the level of 10^{-5} (see figure 1.3). Due to gravitational redshifting of the photons occurring at the surface of the last scattering, the observed structure in the CMB appears. This makes the CMB a probe of the matter distribution at that time.

From the angular variations of the temperature, among other parameters, the distribution of the gravitating matter in the Universe can be determined. The latest and most precise measurement of the CMB was done by the Planck satellite. In figure 1.3 a sky map of the CMB temperature fluctuations observed between 2009 and 2013 is shown [1].

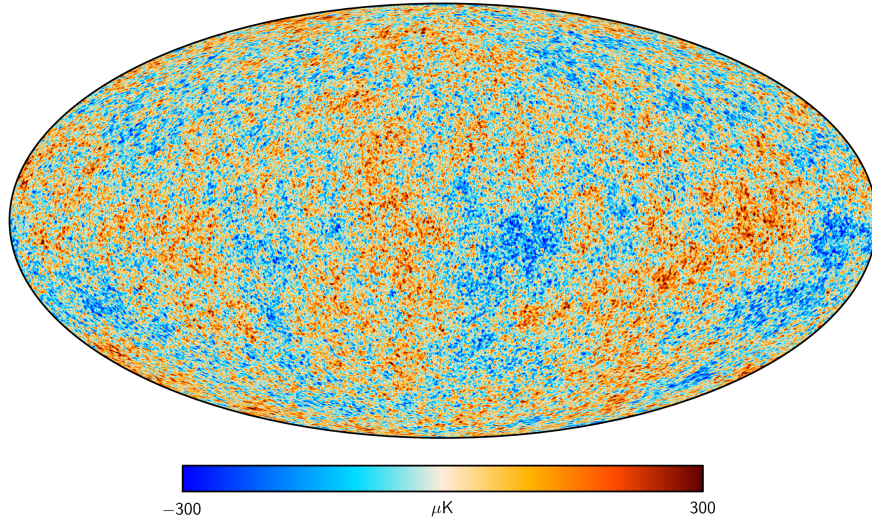


Figure 1.3: Sky map of the CMB temperature fluctuations observed by the Planck satellite with foregrounds subtracted. Color-coded are the variations of the mean temperature of $T \approx 2.7\text{ K}$ on the level of $\pm 300\ \mu\text{K}$. Image taken from [7].

The measurement can be well fitted by the ΛCDM model which describes the Universe to be dominated by dark energy (Λ) and non-relativistic cold dark matter (CDM) [9]. Within the standard model of cosmology the total energy content of the Universe can be described by $\Omega_{tot} = \Omega_M + \Omega_\Lambda$ with the energy density of dark energy Ω_Λ and the matter density Ω_M being the sum of contributions from all matter species, in particular baryonic matter, neutrinos, and dark matter. The data of Planck is consistent with $\Omega_{tot} = 1$ which shows that the Universe is spatially flat [9].

Among many other results, from the data of the Planck satellite the contents of the Universe were determined [10]:

- The major component of the Universe is the completely unknown dark energy with $\Omega_\Lambda = 0.692$.
- The largest part of the matter content is non-baryonic cold dark matter with $\Omega_{\text{CDM}} = 0.259$.
- Only a small fraction of the Universe is baryonic matter: $\Omega_B = 0.049$.

The CMB, being a snapshot of the early Universe, shows evidence for dark matter on a cosmic scale. Only about one fifth of the matter in the Universe is baryonic matter.

1.1.4 Structure Formation

While the CMB shows a picture of the early near-uniform Universe, today's cosmic structure and the distribution of galaxies can be observed in great detail with powerful telescopes like the Sloan Digital Sky Survey (SDSS) [11]. The large scale structure, that is observed today, evolved from the tiny density fluctuations in the early Universe

visible in the CMB. This evolution can be modeled with large computer simulations (like e.g. the Millennium Simulation [12]).

From these simulations, it is not possible to reproduce today's large scale matter distribution when only baryonic matter is included. Instead, there needs to be a significant amount of non-baryonic matter, that clumps together earlier than baryonic matter, which is driven apart by electromagnetic radiation and, thus, cannot form large structures. Dark matter fulfills this requirement as it is able to clump together early. Then, Baryonic matter will follow the gravitational potential of dark matter and can create the observed structure.

With an amount of dark matter that is similar to the fraction of dark matter determined by the CMB, the simulated large-scale structure of the Universe matches the one observed today [13]. This implies that the density of dark matter observed at different time scales of the Universe is consistent.

1.2 Candidates for Dark Matter

All this compelling evidence for the existence of dark matter, raises the question about its nature. The different observations impose constraints on the possible dark matter candidates. Therefore, before discussing possible particles that could make up dark matter, the properties of dark matter are summarized:

- Different observations, like the CMB or the structure formation of the Universe, show that dark matter must be *non-baryonic*. These observations also indicate that dark matter particles must have been non-relativistic at the time of the decoupling of matter and radiation, a property that is referred to as *cold dark matter* (CDM).
- Since dark matter could not yet be detected directly, it must interact very rarely with ordinary matter. It cannot couple to photons, which means dark matter must be *electromagnetically neutral*. Otherwise it would have been seen either through absorption or emission of radiation. Dark matter must also be *color neutral* since no participation in the strong interaction has been observed. A participation in the *weak interaction* is possible but not necessary. However, this would give the possibility to detect dark matter in a direct detection experiment.
- Observations show that it *interacts gravitationally*, which also means that it must have a mass.
- There is evidence for dark matter on all time scales of the Universe, which implies that it is *stable on cosmological times*.

The only particle from the standard model of particle physics that fulfills most of these requirements is the neutrino. However, due to its small mass it is relativistic at the time of the decoupling and cannot form the observed structure of our Universe. Moreover, it can be shown that the neutrino contribution to the energy density is too small to make up a substantial amount of dark matter. The upper bounds on the neutrino masses from particle physics limit the neutrino relic density to $\Omega_\nu = \sum m_\nu / 47 \text{ eV} < 0.042$ [14].

Therefore the evidence for dark matter is also a clear hint for physics beyond the standard model. Numerous candidate particles from theory that could explain dark matter are existing. In the following only the candidates most relevant for a direct detection experiment are explained.

1.2.1 Weakly Interacting Massive Particles

One class of candidates for dark matter are Weakly Interacting Massive Particles (WIMPs) [9, 15]. They interact with a cross section typical for the electroweak interaction and can have masses in the range of a few GeV up to TeV. Hence, they are heavy enough to move with non-relativistic velocities at the time of the freeze-out and, therefore, represent CDM.

WIMPs are thermal relic particles, which means they were produced in the Big Bang and were in thermal equilibrium until the temperature of the Universe dropped below the particles mass. Afterwards, their number decreased due to annihilation reactions with their antiparticle. However, as the Universe is not only cooling but also expanding, at some point the WIMP gas became so diluted that the particles could not find each other anymore to annihilate. At this time the particles froze out and, if these particles are stable, their number density stays constant.

A special feature of the WIMPs is, that their density at the time of the freeze out is consistent with the density that is required for dark matter from cosmological observations. This fact is also called the *WIMP miracle*.

Particles with the properties of WIMPs arise from different extensions to the standard model. A popular one is the introduction of supersymmetry (SUSY) in order to solve the gauge hierarchy problem [9]. In SUSY every SM particle has a new partner particle, which has the same quantum numbers and interacts in the same way, but differs in spin by 1/2, introducing a fermionic super partner to a boson and vice versa. In many SUSY models a newly introduced quantum number (R-parity) is conserved which leads to the lightest supersymmetric particle (LSP) not being able to decay into a SM particle. The LSP is a promising WIMP dark matter candidate.

There are also other theories that introduce particles with WIMP properties like models with spatial extra dimensions. For details on WIMP candidates and more examples see e. g. [9, 15].

Due to the Lee-Weinberg limit the mass has to be greater than a lower bound of $\sim 2 \text{ GeV}/c^2$ since lighter particles would lead to an overclosure of the Universe [16]. In conclusion, WIMPs are well motivated candidates for dark matter particles with large masses.

1.2.2 Asymmetric Dark Matter

The motivation for models of asymmetric dark matter (ADM) [17, 18] follows from the observation that the mass density of dark matter is only about a factor of five higher than the density of baryonic matter: $\Omega_{DM} \simeq 5\Omega_{baryonic}$. This similarity may not be coincidence but suggests that there is a strong relation between the origin and cosmological history of dark matter and baryonic matter.

The ADM hypothesis states that the dark matter density has a similar origin as the density of baryonic matter, which has been established due to the baryon asymmetry of the Universe. Analogous there might be a dark matter particle-antiparticle asymmetry and these two asymmetries were related in the early Universe but decoupled later.

There exist a number of theories for ADM that involve dark matter particles with a mass typically in the range of 1 to 15 GeV/ c^2 [19]. ADM theories present a variety of possibilities, ranging from simple solutions with dark matter constituting of one particle and its antiparticle with an asymmetry in their number density that developed in the early Universe up to more complicate solutions where dark matter consists of more than one stable particle with different states and interactions. Dark matter and the baryonic matter may even have been interacting in the early Universe in some models and many scenarios relate the origin of the dark matter mass to the standard model scales.

Baryonic matter and ADM can interact gravitationally and also weakly, which is a requirement for direct detection. If the mass of the mediator of the dark matter-nucleus scattering is large, the same analysis and bounds as for WIMPs apply for direct detection of these particles [17].

An overview of the theories that include ADM as well as information on the phenomenology and bounds of ADM can e.g. be found in [17, 18].

Other Candidates

There are many other candidates for dark matter predicted from extensions of the standard model, which are not explained in detail here. An extensive review of many other candidates can be found in e.g. [9, 15], while only two more well motivated candidates should be mentioned in the following. Like WIMPs they arise from theories not related to solve the dark matter problem, but nonetheless were found to be a candidate for dark matter and gained more and more interest in the past.

The first example is the *axion*, that is suggested to solve the strong CP problem [20]. Dedicated experiments are trying to detect them, using the fact that they are expected to convert to photons in the presence of a magnetic field through the Primakoff effect [15].

Another candidate arises from an extension of the standard model that suggests, that next to the left-handed neutrinos present in the standard model, also right-handed neutrinos are existing. These right-handed neutrinos do not interact with the standard model particles but can mix with the left-handed neutrinos, due to neutrino oscillations. These particles are called *sterile neutrinos* and are more heavy than left-handed neutrinos. They may have astrophysical effects, that allow to detect them [15].

1.3 Methods for the Detection of Dark Matter

There are three main strategies to gain information about the nature of dark matter, which are:

- The production of new particles in a collision of standard model particles at particle colliders,
- the search for annihilation or decay products of dark matter (indirect detection),

- and the search for interactions of dark matter with standard model particles (direct detection).

Whether it is possible to detect dark matter by one or more of these methods depends on the type and strength of interaction between dark matter and the standard model particles. A short overview on the possibilities of these methods is given in the following.

Particle Colliders

Particle colliders like the Large Hadron Collider (LHC) can in principle produce dark matter particles but due to their weak Standard-Model interactions, they escape colliders undetected. However, it is possible to probe their existence through missing-energy signals in higher order processes (mainly due to indirect production) [15, 21]. Which type of events (characterized by the number and types of jets, leptons, geometry or timing) can give constraints on dark matter particles strongly depends on the exact model.

Additionally, even if evidence for a new particle, that fits the constraints imposed on dark matter, is found in colliders, this only implies that this particle is stable enough to exit the detector but not that it is necessarily the real component of dark matter. However, with detailed studies it would be possible to determine the relic density of a new particle [15]. The consistency with the observed relic density of dark matter would provide evidence, that the particle produced in the collider is dark matter.

Indirect Detection

In dark-matter dense regions of the Universe, matter also clusters. Therefore, in regions with a large mass density, dark-matter particles might self-annihilate or decay to standard model particles which can then be detected. Thereby, dark matter may be detected indirectly. Several particles are used for indirect detection of dark matter, in particular gamma rays, neutrinos, and antiparticles such as antiprotons and positrons [21].

Charged particles undergo diffusion in the galactic magnetic field, whereas photons and neutrinos can travel through space undisturbed and, therefore, might even reveal the spatial distribution of dark matter.

Space-based satellite experiments (e.g. Fermi-LAT [22]) as well as ground-based atmospheric Cherenkov telescopes (e.g. H.E.S.S. [23]) are searching for an excess of gamma rays and antiparticles. There have been several observations of possible dark-matter annihilation signals. However, with more data these signatures seem to find explanations due to ordinary astrophysical processes. From gamma ray searches there are constraints on the annihilation cross-section for WIMP masses up to 10 TeV. In particular for antiparticle observations the propagation of cosmic rays and their production of secondary particles needs an accurate modeling in order to distinguish dark-matter contributions from background signals [21].

Additionally WIMP dark matter can be gravitationally trapped in the Sun or in the Earth and annihilate there due to the high density. Large neutrino telescopes like IceCube [24] looking for an excess of neutrinos from the Sun, are especially sensi-

tive to spin-dependent WIMP-nucleus cross section [25]. Current constraints on spin-dependent dark matter are competitive with direct detection experiments.

Indirect detection experiments typically search for WIMPs since they are expected to exist as particle and antiparticle. However, also other dark matter candidate particles could produce signals in cosmological observations [21, 26].

Direct Detection

Direct detection experiments aim to detect scatterings of dark-matter particles from the Milky Way halo off baryonic matter in a detector on Earth. Due to the weak interactions of dark matter these experiments need highly sensitive detectors and an ultra-low background. The requirements for these experiments are discussed in detail in the following. Afterwards, an overview of the experiments, aiming to detect dark matter directly, is given.

1.4 Direct Detection of Dark Matter

Observations of dark matter as described in section 1.1 show that dark matter forms a spherical halo around the luminous matter in galaxies that exceeds the visible components by many times. If dark matter particles do not only interact gravitationally with luminous matter but also interact with weak-scale cross sections, they may scatter off ordinary matter and transfer energy. This energy might be detectable in a sensitive earth-bound detector.

Direct detection experiments aim to measure the elastic scattering of dark matter particles off nuclei in dedicated detectors. As dark matter particles are bound gravitationally to the Milky Way, their velocities must be below the galactic escape velocity and, thus, their interactions with the nuclei are expected coherently. In order to estimate the requirements for such a detector the expected interaction rates and energies are evaluated in this section.

Most of the direct detection experiments are aiming to detect dark matter in the form of WIMPs. In the following a mathematical description of the rate for WIMP-nucleus scattering is derived. For more details see e.g. [27, 28].

1.4.1 Detection Rates and Energy Spectrum

A first requirement for a dark matter detector is its ability to detect low energies, as the recoil energy E_R induced by a dark matter particle of mass m_χ on a nucleus of mass m_N is given by:

$$E_R = \frac{\mu_N^2 v^2}{m_N} (1 - \cos \theta), \quad (1.1)$$

with the relative velocity v , the scattering angle θ and the reduced mass of the WIMP-nucleus system μ_N , which is defined as:

$$\mu_N = \frac{m_\chi m_N}{m_\chi + m_N}. \quad (1.2)$$

The maximal energy is transferred in the case of back scattering ($\theta = \pi$) and both particles having the same mass ($m_\chi = m_N$). For typical velocities of gravitationally bound particles ($v \approx 10^{-3}c$) the maximum recoil energy is

$$E_{R,max} = \frac{1}{2}m_\chi v^2 \approx \frac{1}{2}m_\chi \cdot 10^{-6}c^2 = \frac{1}{2} \left(\frac{m_\chi}{\text{GeV}/c^2} \right) \text{keV}. \quad (1.3)$$

Most dark matter models relevant for direct detection experiments have candidates with masses of $m_\chi \sim \mathcal{O}(10 \text{ GeV}/c^2)$ [9]. Thus, the maximum transferred energies are in the order of a few 10 keV. Consequently, direct detection experiments need to be able to detect such low energies, which means that *very sensitive detectors* and a *low threshold* are required.

Interaction Rate

The interaction rate R for WIMP-nucleus scattering in a detector with mass M_{target} made of target nuclei with mass m_N depends on the dark-matter flux through the detector Φ and the WIMP-nucleus cross section σ by

$$R = \frac{M_{target}}{m_N} \Phi \sigma. \quad (1.4)$$

The flux Φ of dark matter particles through the detector is

$$\Phi = \frac{\rho_\chi}{m_\chi} v \quad (1.5)$$

with the local dark matter mass density ρ_χ , which is derived by applying observational constraints (including the the Milky Way rotation curve) to models of the Milky Way. The value that is assumed to compare direct detection experiments is $\rho_\chi = 0.3 \frac{\text{GeV}/c^2}{\text{cm}^3}$ as found e.g. in [29].

With an elastic cross section on the electroweak scale ($\sigma \approx 10^{-38} \text{ cm}^2$), a relative velocity $v \approx 10^{-3}c$, and typical values for the mass of nucleons and dark matter particles of about $100 \text{ GeV}/c^2$ the rate for elastic scattering is $R < 10 \text{ events kg}^{-1} \text{ a}^{-1}$. This very low rate is another challenge for direct detection experiments, which requires a substantial *background reduction*.

Differential Recoil Spectrum

The low recoil energies and the total event rates are both a challenge for direct detection experiments. The quantity that is aimed to be measured is the differential event rate dR/dE_R , which can be calculated by differentiating equation 1.4 with respect to the recoil energy E_R . It has also to be taken into account that not all dark matter particles have the same velocity, but instead have a velocity distribution $f(\vec{v})$. In addition, the WIMP-nucleus cross section depends on the velocity and the recoil energy. Thus, the differential event rate can be calculated as

$$\frac{dR}{dE_R} = \frac{\rho_\chi}{m_N m_\chi} \int_{v_{min}}^{\infty} d^3v f(\vec{v}) v \frac{d\sigma(\vec{v}, E_R)}{dE_R}, \quad (1.6)$$

with v_{min} being the lowest velocity of a dark matter particle that can transfer the energy E_R to a nucleus:

$$v_{min} = \sqrt{\frac{E_R m_N}{2\mu_N^2}}. \quad (1.7)$$

In order to evaluate equation 1.6 some input from particle as well as nuclear physics is needed, which is considered in the following.

Scattering Cross Section

The WIMP-nucleus cross section can have a spin-independent and a spin-dependent contribution. The spin-independent part describes the scalar interactions, while the spin-dependent part describes the coupling of dark matter particles to the net spin of the target nuclei. In the case of CaWO_4 as target material (as in the CRESST experiment) the target nuclei have only a very small net spin and, thus, the spin-dependent part is neglected here. The spin-independent WIMP-nucleus cross section is given by [27]

$$\left(\frac{d\sigma}{dE_R}\right)_{SI} = \frac{m_N \sigma_0}{2\mu_N^2 v^2} F^2(E_R), \quad (1.8)$$

where σ_0 is the cross section at zero momentum transfer and $F(E_R)$ is the nuclear form factor for coherent interactions. In most models the WIMP coupling to neutrons and protons is similar and, therefore, the cross section scales as the square of the number of nucleons A : $\sigma_0 \sim A^2$.

Due to the dependence of σ_0 on the target nucleus, this quantity is not a good parameter to compare different experiments with different target materials. Instead, the normalized WIMP-nucleon cross section σ_{WN} , which is independent of the target material, is used by direct detection experiments to constrain the interaction strength of WIMPs. It is defined as [30]:

$$\sigma_{WN} = \left(\frac{1 + m_\chi/m_N}{1 + m_\chi/m_p}\right)^2 \frac{\sigma_0}{A^2}, \quad (1.9)$$

where m_p is the proton mass.

With the input of the cross section (equation 1.8) the differential rate (equation 1.6) can be rewritten as

$$\frac{dR}{dE_R} = \frac{\rho_\chi}{2m_\chi \mu_N^2} \sigma_0 F^2(E_R) \int_{v_{min}}^{\infty} d^3v \frac{f(\vec{v})}{v}. \quad (1.10)$$

Form Factor

At low recoil energies the nucleus can, to a good approximation, be described as a point-like object. However, for higher momentum transfers the substructure of the nucleus has to be taken into account since it leads to a loss of coherence in the WIMP-nucleus interaction. This is done by the form factor $F(E_R)$ which is formally the Fourier transformation of the nucleus' density.

In dark matter searches a simple parametrization for the form factor is used, which was initially developed by Helm [31] and investigated by Engel [32]. In this model the

nucleus is described with two density functions, that describe the nucleus as a sphere of constant density with a decrease of density at the edge of the sphere. The form factor is described by:

$$F(q) = 3 \frac{j_1(qR_0)}{qR_0} \exp\left(-\frac{1}{2}q^2 s^2\right) \quad (1.11)$$

with the first spherical Bessel function $j_1(qR_0)$ depending on the momentum transferred in the scattering process $q = \sqrt{2m_N E_R}$ and the nuclear radius R_0 and the thickness parameter for the surface of the nucleus $s \simeq 1$ fm.

Velocity Distribution

The simplest model for the velocity distribution of WIMPs is the assumption of an isothermal sphere. In this approximation the velocity distribution can be described by a Maxwell-Boltzman distribution in the rest frame of the galaxy. With a truncation of the WIMP velocities at the escape velocity v_{esc} of the Milky Way (particles with a higher velocity cannot be bound in the galaxy and, therefore, their density is negligibly small) the velocity distribution $f(\vec{v})$ is given by [30]

$$f(\vec{v}) = N \left(\frac{3}{2\pi w^2}\right)^{3/2} \exp\left(-\frac{3v^2}{2w^2}\right). \quad (1.12)$$

The normalization factor N is

$$N = \left(\operatorname{erf}(z) - \frac{2}{\sqrt{\pi}}z \exp(-z^2)\right)^{-1} \quad (1.13)$$

with

$$z = \frac{3v_{esc}^2}{2w^2}. \quad (1.14)$$

The root mean square velocity of dark matter particles w is in the model of an isothermal halo connected to the asymptotic value of the rotational velocity v_∞ by the relation $w = \sqrt{3/2}v_\infty$ [30]. In the Milky Way the rotational velocity is over large ranges $v_\infty = 220$ km/s [33] and, therefore, $w = 270$ km/s. The value of the galactic escape velocity is $v_{esc} = 544$ km/s [34].

Spectrum

With all this information together, it is possible to calculate the expected differential event rate. In figure 1.4 the expected spectra for CaWO_4 for four different WIMP masses between $3 \text{ GeV}/c^2$ and $100 \text{ GeV}/c^2$ are shown. For a compound material (like CaWO_4) the total interaction rate is the sum of the rate of the individual constituents.

The spectra show almost no features besides the exponential decay and the rate is relevant only for energies below ~ 50 keV. With a currently expected cross section of $< 10^{-7}$ pb the overall rates are very low in the order of 10 counts per kg and year.

1.4.2 Detector Effects

Up to now all considerations were performed for an ideal detector. However, in a real experiment some additional aspect have to be taken into account and are briefly discussed in the following.

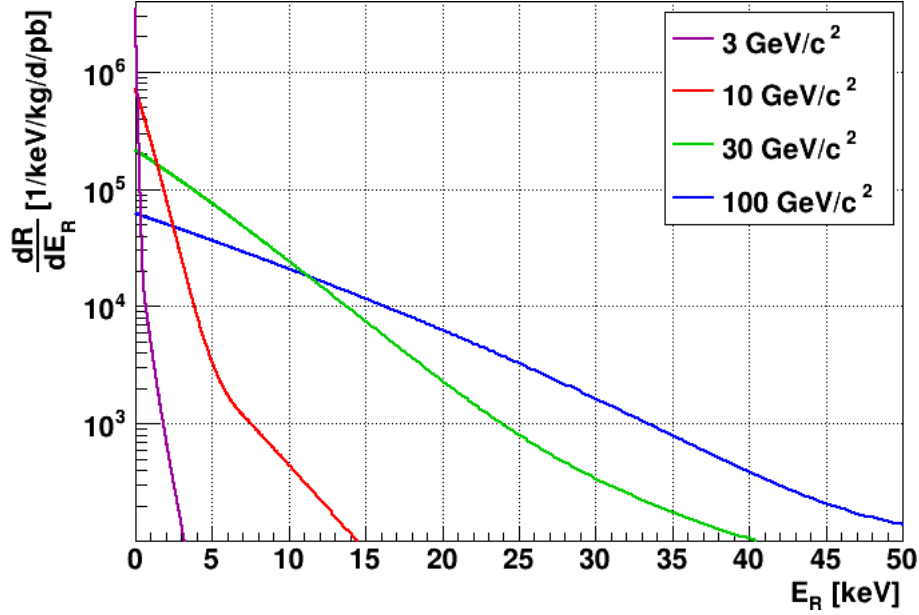


Figure 1.4: Differential event rate for WIMP masses of $3 \text{ GeV}/c^2$, $10 \text{ GeV}/c^2$, $30 \text{ GeV}/c^2$, and $100 \text{ GeV}/c^2$ scattering off CaWO_4 .

Energy Resolution

A real detector has a finite energy resolution. The energy resolution $\Delta E(E_R)$ of the detector is assumed to be Gaussian distributed and in general depends on the recoil energy E_R . Therefore, the measured differential rate $\left. \frac{dR}{dE_R} \right|_{obs}$ is a convolution of $\frac{dR}{dE_R}$ with a Gaussian function:

$$\left. \frac{dR}{dE_R} \right|_{obs} = \frac{c}{\Delta E(E_R)} \int_0^\infty dE \frac{dR}{dE} \exp\left(-\frac{(E_R - E)^2}{2\Delta E^2(E_R)}\right), \quad (1.15)$$

with a normalization constant c .

Trigger Threshold

Real detectors have a finite energy threshold, below which deposited energies cannot be registered. In CRESST the energy threshold is set by a hardware trigger.

Due to the exponential rise of the differential dark matter rate towards lower recoil energies a lower trigger threshold increases the number of expected events significantly for all dark matter masses. However, this is especially important for light dark matter particles. A particle with a mass of $3 \text{ GeV}/c^2$ is expected to induce only recoils with energies below $\sim 3 \text{ keV}$ with a relevant rate (see figure 1.4). Thus, to detect such a particle a lower threshold than $\sim 3 \text{ keV}$ is required. In conclusion, the lower the threshold of the detector the lighter the particles that are possible to be detected.

Additionally, a low threshold is also beneficial for heavy particles. Due to the exponential rate, also for a heavy particle, the number of expected recoil events is higher for a lower threshold (see figure 1.4).

1.4.3 Experimental Requirements and Signatures

In conclusion, there are the following challenges for an earth-bound direct dark matter detection experiment:

- Dark matter particles are expected to transfer low recoil energies and to have a featureless exponential spectrum. Thus the experiments need very sensitive detectors with a low threshold. The lighter the dark matter particles are, the lower the trigger threshold must be to be able to detect them.
- In order to detect such small event rates, dark matter detectors need a very low background even for very low energies.
- Dark matter particles are expected to scatter elastically off nuclei. However, the dominant background from internal and external radioactivity are γ -induced electron recoils. Therefore, many experiments have an active background suppression that allows them to distinguish between electron and nuclear recoils.

How these challenges are faced in the case of the CRESST experiment is shown in chapter 2.

In order to discover a dark matter particle it is necessary to distinguish it from background sources, that can also produce an exponential spectrum at low energies. There are several signatures that can identify a dark matter particle:

- Dark matter particles are expected to interact with different target materials in a known way, since the interaction rate has an A^2 dependence. Therefore, the expectations can be cross-checked with different target materials either from different experiments or with a *multi-element target*, as it is realized in the CRESST experiment.
- Additional to the movement of our solar system through the galaxy the earth is rotating around the sun and, therefore, an *annual modulation* of a dark matter signal is expected. However, the difference in the rate is only a few percent and, thus, this investigation needs high statistics [35].
- Due to the Earth's motion through the galaxy and its rotation there is a preferred *direction of the dark matter flux* expected. If the detector is able to detect the direction of the recoils this would be a possibility to discriminate dark matter from any terrestrial background.

1.4.4 Experimental Techniques for Direct Dark Matter Search

In the following a short overview of selected detection techniques and experiments for the direct dark matter search is given. For a more complete review see e.g. [36] and the references therein. An illustration of leading limits of several experiments is shown in figure 2.15.

In general nuclear recoils can be detected by exploiting three different detection channels, that are phonons, ionization and scintillation light. Which of them can be used depends on the target material.

Liquid Noble Gas Detectors

Liquid noble gases, such as xenon, argon and neon, are used as target material by several direct detection experiments. Single-phase detectors detect the scintillation light produced by scattering events with photomultiplier tubes (PMTs), whereas dual-phase experiments use so-called time projection chambers (TPCs). In TPCs, the simultaneously produced charge is drifted to the interface between liquid and gaseous phase by an applied electric field. Thereby, two signals are detected: The first is, as in the single-phase detectors, the scintillation light produced in the liquid phase and, additionally, a second delayed scintillation signal, which is proportional to the charge, is produced in the gaseous phase. The measurement of both signals enables a discrimination between electron and nuclear recoils.

The advantage of liquid noble gases is that the spatial position of the events can be determined which allows a surface-event rejection and thereby a self-shielding of the central volume. Furthermore, the design of the experiments allows to easily realize experiments on the ton-scale, which increases the exposure and the sensitivity to high-mass WIMPs. However, the threshold of liquid noble gas experiments is typically higher than of small-sized cryogenic detectors.

Presently, LUX, operating a dual-phase TPC with liquid xenon as target material, gives the most stringent limit for WIMP masses above $4 \text{ GeV}/c^2$ with a minimum upper limit on the cross section of $0.6 \cdot 10^{-45} \text{ cm}^2$ at a WIMP mass of $33 \text{ GeV}/c^2$ [37]. Another experiment using a LXe TPC is the XENON experiment, which set a limit with the XENON100 setup [38]. In the future XENON1T aims to study cross sections down to 10^{-47} cm^2 [39].

Cryogenic Solid State Detectors

Solid state detectors that are cooled to cryogenic temperatures are another category of direct search experiments. The targets can be semiconductors like germanium (Ge) and silicon (Si) in which ionization and/or heat can be detected or inorganic scintillators such as calcium tungstate (CaWO_4) and zinc tungstate (ZnWO_4). Cryogenic detectors can be operated with a low energy threshold and a good resolution and, therefore, are well suited for dark matter search.

Similar to liquid noble gas experiments, most of the experiments operate a two-channel detection that provides a background discrimination on event by event basis and thereby increasing the sensitivity significantly compared to a single-channel detection. However, one single-channel technique should be mentioned here first.

There are several single-channel experiments, that are using p-type point-contact, low threshold, high purity Ge detectors. The CoGeNT experiment, which has the ability to reject surface backgrounds, observe an excess of low energy events above the expected background, which can be interpreted as dark matter particle with a mass of $7\text{-}9 \text{ GeV}/c^2$ [40]. However, recent analyses of this data by a subgroup of the collaboration question this interpretation [41]. Furthermore, another experiments using the same technology, called CDEX [42], published data in 2014 that exclude the parameter space preferred by CoGeNT.

The CDMS experiment is based on a phonon-ionization detection using Ge and Si

detectors operated at mK temperatures. They can measure the phonon (heat) signal of recoil events precisely and simultaneously use the ionization signal to discriminate electron and nuclear recoils. While they published a result with an excess of events in the Si detectors in 2013 [43], the SuperCDMS upgrade, which operates Ge detectors with a new iZIP design with improved background rejection capability, could set a limit that excludes the previous result [44]. Within the SuperCDMS setup the iZIP detectors can be operated in the CDMSlite mode, which degrades the nuclear recoil discrimination but provides a lower threshold. The CDMSlite experiment published a limit exploring dark matter particle masses down to $2 \text{ GeV}/c^2$ in 2015 [45].

The CRESST-II experiment operates scintillating CaWO_4 crystals at mK temperatures, measuring the phonon signal for a precise energy measurement and additionally the scintillation light signal for electron recoil discrimination. The setup, the detection technique and the results are discussed in chapter 2. In phase 1 of CRESST-II an excess over expected background was observed, which is partly excluded by results of upgraded detectors in phase 2. Moreover, in phase 2 the low-mass parameter space was explored down to dark matter particle masses of $0.5 \text{ GeV}/c^2$.

Single-Channel Annual Modulation Searches

The DAMA/Libra experiment uses $\sim 250 \text{ kg}$ of Tl-doped NaI as target crystals to search for the annual modulation of WIMP-nucleus interactions. The scintillation signal is measured with low-background PMTs. In the total exposure with 13 annual cycles a modulation (with a phase of 147 ± 7 days which is consistent with the expected phase for dark matter of 153 days) with a statistical significance of 8.9σ is observed [46].

As a background origin of this signal is not completely ruled out, other experiments are trying to probe this WIMP claim, such as the DM-Ice project [47] that is as well using NaI crystals in the infrastructure of the IceCube experiment at the South Pole. Due to its location on the southern hemisphere (in contrast to the DAMA/LIBRA experiment located in Italy) DM-Ice can directly test if the observed modulation is due to seasonally related backgrounds, which would be out of phase in different hemispheres.

Bubble Chambers

Direct dark matter searches with bubble chambers use a superheated fluid as target material. They are weakly superheated so that an energy deposition from a nuclear recoil induces a bubble nucleation, while energy depositions on electrons, which lose their energy over a longer range, do not induce bubbles. Alpha particles, which deposit enough energy to produce bubbles, can be discriminated with acoustic signals.

One experiment operating a bubble chamber is the experiment PICO using 2 liter C_3F_8 as target and it demonstrated a good discrimination power against background events [48].

Several other techniques exist to detect dark matter directly, like the usage of CCD chips or time projection chambers to detect the directionality of nuclear recoils. An overview of the currently available and proposed experiments can be found in [36].

Prospects

The field of direct dark matter detection is an active field with many different techniques and experiments. During the last years some experiments observed signals with an excess over the expected background while other excluded the parameter space these signals hinted for. Some of these signals were clarified as background not considered before.

By now, several experiments try to reduce the sensitivity to lower dark matter particle mass regions, where CRESST and CDMSlite are the leading experiments with a sensitivity down to $0.5 \text{ GeV}/c^2$ and $1.3 \text{ GeV}/c^2$, respectively. Many experiments make efforts to explore the dark matter parameter space down to the finally limiting background of coherent neutrino nucleus scattering of solar and atmospheric neutrinos [49] within the next decade.

Chapter 2

The CRESST Experiment

CRESST (Cryogenic Rare Event Search with Superconducting Thermometers) aims to directly detect dark matter particles in the form of WIMPs. This chapter describes how the CRESST experiment is designed in order to deal with the challenges of direct dark matter detection as described in chapter 1.

The setup of the experiment and the measures taken to reduce the background are described in section 2.1. The basic working principle and the components of the detectors are explained in section 2.2. A two channel detection allows for an active background discrimination of the remaining backgrounds (section 2.3). Section 2.4 concentrates on the methods to operate the detectors and the components used for data taking. The basic principles of the CRESST data analysis are discussed in section 2.5. This chapter concludes with an overview of the results of the CRESST-II¹ data-taking phases and the future strategy of the CRESST experiment, which is the basis for this work.

2.1 Experimental Setup

Dark matter particles are expected to interact at most a few times per year in the CRESST experiment (see section 1.4). In order to be able to detect the tiny recoil energies induced by them it is crucial to reduce the background and shield the target against cosmic radiation and natural radioactivity. In the setup of the CRESST experiment (shown in figure 2.1) various layers of shieldings surround the experimental volume in the center, where the detectors are located and operated at millikelvin temperatures. All essential components of the setup are described in the following.

2.1.1 Background Reduction

All events that can deposit energy in the detectors in the same energy range as WIMP interactions are background sources for dark matter search. The relevant background sources and the measures to reduce them as much as possible are described in the following.

¹CRESST-I used sapphire crystals and a single-channel readout to search for dark matter. Its upgrade CRESST-II used mainly scintillating CaWO₄ crystals and is described in this chapter. The current stage CRESST-III is introduced at the end of this chapter. For simplicity, the general term CRESST refers to the second and third stage of CRESST, as the setup of both, except the detectors, is identical.

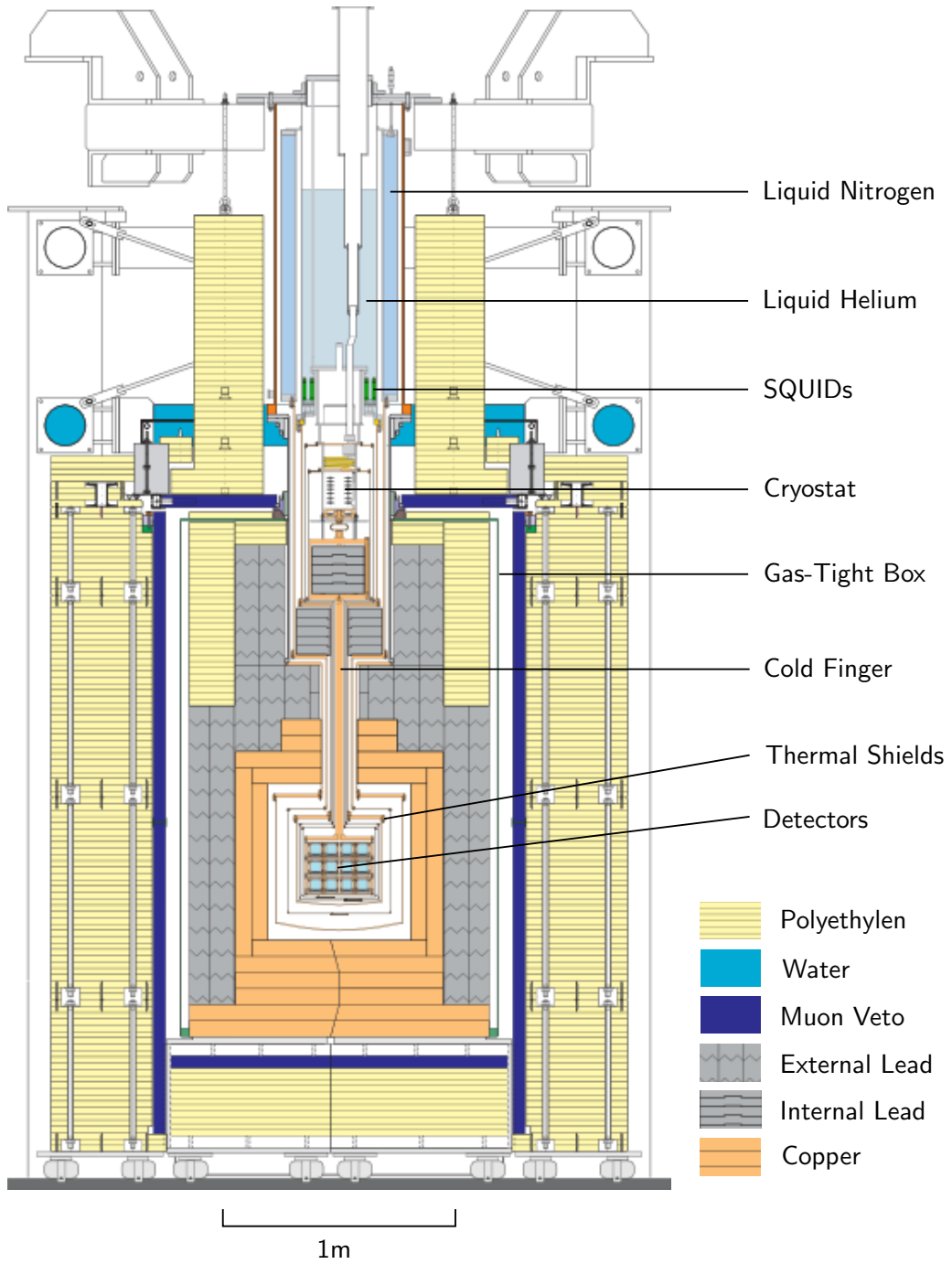


Figure 2.1: The setup of the CRESST experiment. The experimental volume where the detectors are located is in the center and cooled by the cryostat on top. To shield external backgrounds it is surrounded by several layers of shielding. For details see text.

Muons

The Earth is constantly hit by cosmic radiation, which consists mainly of protons. In the atmosphere secondary particles are produced, of which muons are the most penetrating component. In order to shield muons CRESST is located deep underground in the LNGS (Laboratori Nazionali del Gran Sasso) in central Italy. With a minimum overburden of 1400 m dolomite rock (equivalent to more than 3000 m water) the muon flux from the Earth's surface is reduced by six orders of magnitude to $\mathcal{O}(1 \text{ m}^{-2}\text{h}^{-1})$ [50]. All other components of the cosmic radiation are completely suppressed.

However, the remaining muons can still induce background events by either passing through the detectors directly or by producing secondary particles (electrons, gammas, neutrons, or nuclei) in the surrounding material. These secondaries can then reach a detector and induce background events. In order to identify muon induced events, the CRESST setup is surrounded by a *muon veto*, which consists of 20 plastic scintillator panels, each one read out by a single photomultiplier (dark blue in figure 2.1). The muon veto covers about 98.7% of the solid angle around the detectors. Whenever an event is detected in the veto, it is stored on disk and allows to reject coincident events in an offline analysis.

Gammas and Electrons

Another prominent source of background are gammas and electrons originating mainly from the natural radioactive decay chains of ^{238}U and ^{232}Th , as well as the natural isotope ^{40}K . These are present in contaminations in the rock of the underground laboratory or in the materials around the detectors. The total gamma flux in the LNGS has been measured to be about $1 \text{ cm}^{-2}\text{s}^{-1}$ with energies up to 2.7 MeV [51].

In order to shield this background the experimental volume is surrounded by a 20 cm thick lead shield with a total mass of 24 t (gray in figure 2.1). Due to its large atomic number and high density, lead provides a good stopping power for gamma radiation. However, lead also has a high intrinsic radioactivity. In particular its unstable isotope ^{210}Pb , naturally present in the ^{238}U decay chain. ^{210}Pb decays over several steps to the stable isotope ^{206}Pb under the emission of α -, β -, and γ -radiation, which can contribute to the background of the experiment.

In order to shield the background from ^{210}Pb an additional layer of shielding is placed inside the lead shield. This shield is made of 10 t and 14 cm thick highly pure copper (orange in figure 2.1). Copper can be produced with a very low intrinsic radioactivity and therefore, is also a suitable material to be used for structures in the vicinity of the detectors. In positions where the lead cannot be shielded with a copper layer, Roman lead with a very low activity is used [52].

Radon

The noble gas radon is another source of radioactivity being present in ambient air. The isotope ^{222}Rn is part of the ^{238}U decay chain and decays via α -decay in ^{218}Po . It can be washed out or diffuse out from the rock which has a high content of ^{238}U . The radon activity at the LNGS was measured to be 50 Bq per cubic meter of air [51].

The experimental volume and also the lead and copper shielding are surrounded by a gas-tight box (green box in figure 2.1), the so-called *radon box*, in order to keep the inner part of the experiment in a radon-free environment. It is constantly flushed and kept under slight overpressure with pure nitrogen gas.

As radon can be adsorbed on any surface, special care has to be taken during the preparation of the detector modules. All copper pieces of the detector holder and other structures close to the detectors are etched in nitric acid to remove surface contaminations. After etching they are stored in flow boxes flushed with clean nitrogen gas and kept as little as possible in radon-containing air.

Neutrons

As expected for WIMPs also neutrons scatter elastically off nuclei and, therefore, are a very dangerous source of background. The neutron flux in the LNGS comes from (α, n) reactions on light elements, from fission of heavy nuclei in the rock, and from muons interacting in the surrounding of the experiment. It was measured to be about $30 \text{ m}^{-2}\text{h}^{-1}$ for neutron energies of 1 to 25 MeV [53].

To prevent neutrons from reaching the detectors, an additional layer of shielding, which consists of 50 cm thick and 10 t heavy polyethylene (PE), is installed as outermost layer of the shielding (yellow in figure 2.1). At places difficult to access the shielding is improved with containers filled with PE granulate or water. Due to the high content of light hydrogen atoms, PE and water moderate neutrons to thermal energies (in the range of meV), so that they can no longer deposit measurable energies in the detectors.

In order to shield neutrons that are produced in the lead or copper shielding, another 3.5 cm of PE is installed in the outer vacuum chamber (OVC). The material was selected to be of high radiopurity (especially with a low content of ^{238}U and ^{232}Th) in order to avoid (α, n) reactions within the PE.

2.1.2 Cryostat and Experimental Volume

CRESST detectors are operated at temperatures of about 10 mK. Such low temperatures are provided by a commercial $^3\text{He}/^4\text{He}$ dilution refrigerator. The cryostat as well as its storage tanks for liquid nitrogen and liquid helium are shown in the upper half of figure 2.1. As the materials of the cryostat are not selected for low-background applications, the setup is designed so that the detectors are shielded from the radioactive contamination of the cryostat.

The detectors are mounted on a support structure made of NOSV copper, which is ultra-pure and suited for low-temperature operation [54]. This so-called carousel was constructed to hold up to 33 detector modules with a total target mass of ~ 10 kg. Figure 2.2 shows a picture of the carousel with detectors mounted. Enclosed by five thermal shields, the carousel has no line of sight to any parts of the cryostat. In order to locally separate the detectors from the cryostat, the carousel is mechanically and thermally connected to the cryostat by a 1.5 m long copper rod. This so-called *cold finger* transfers the cooling power of the cryostat to the experimental volume. Both, the cold finger and the thermal shields are made of radiopure copper. Between the experimental volume and the cryostat a shielding of high-purity lead is installed to

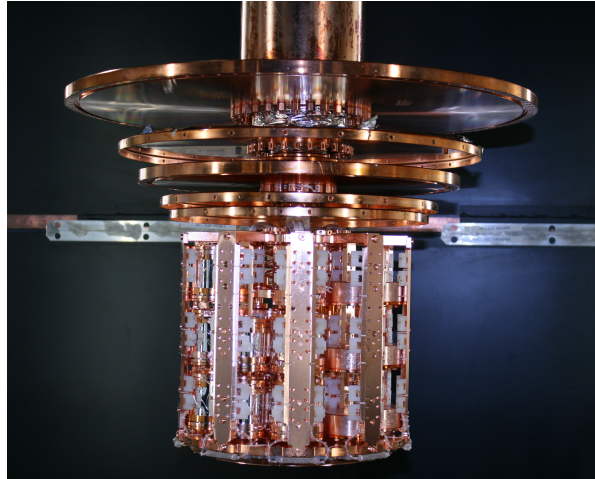


Figure 2.2: *The carousel was designed to hold up to 33 detector modules (equivalent to a total target mass of 10 kg). In the upper part of the picture the flanges for connecting the thermal shields and the vacuum chamber are visible.*

prevent the detectors of seeing background from the cryostat (see figure 2.1).

Cryogenic detectors are very sensitive to mechanical vibrations. Therefore, the whole cryostat rests on air dampers and does not touch the shielding. In order to suppress mechanical vibrations introduced by the cryostat, the carousel is decoupled from the cold finger by springs.

The complete setup including the electronics for readout of the detectors is contained in a Faraday cage to avoid electromagnetic interference. The lower part of the setup is installed in a class 100 clean room to allow for detector installation in clean conditions.

2.2 Cryogenic CRESST Detectors

Dark matter particles are expected to induce low energetic nuclear recoils (see section 1.4). Therefore, for a detection of dark matter very sensitive detectors are necessary. The working principle and the components of CRESST detectors are explained in this section.

2.2.1 Cryogenic Calorimeter

CRESST uses cryogenic calorimeters as particle detectors. Calorimeters measure the deposited energy due to a particle interaction in an absorber by detecting the resulting temperature rise with a sensitive thermometer. The output of the thermometer is a measurable electrical signal.

Cryogenic calorimeters are well suited for dark matter experiments, since they are able to detect very low energies with an excellent energy resolution [55]. Another advantage is the possibility to use a large variety of absorber materials.

A cryogenic calorimeter consists of an absorber with heat capacity C , a thermometer and a thermal link to the heat bath. An energy deposition ΔE in the absorber induces

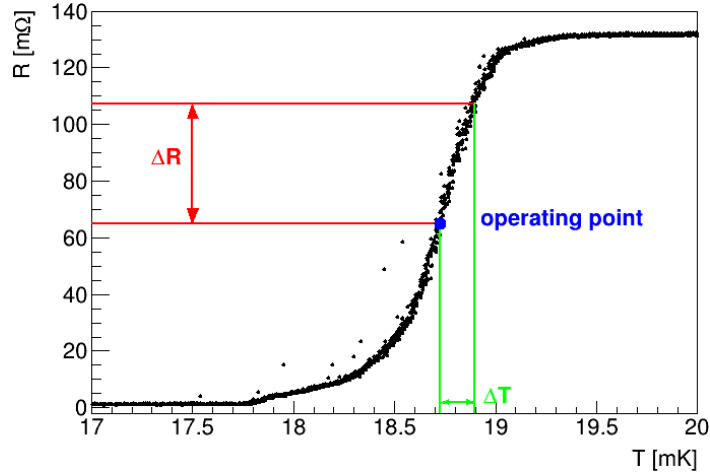


Figure 2.3: Transition curve of a typical tungsten TES used in CRESST. The TES is stabilized in its operating point in the transition from normal to superconductivity. This allows to detect small temperature rises ΔT (e.g. induced by a particle interaction) by measuring the resistance rise ΔR .

the temperature rise ΔT :

$$\Delta T = \frac{\Delta E}{C}. \quad (2.1)$$

After an energy deposition the temperature relaxes back to equilibrium via the thermal link.

To be able to measure very small energy depositions of some keV, as e.g. expected for dark matter interactions, the heat capacity needs to be sufficiently small. This can be achieved by cooling the absorber to ultra-low temperatures as for dielectric materials at low temperatures $C \sim T^3$ [56]. At 10 mK, the operating temperature of CRESST detectors, the heat capacity of a dielectric absorber is 13 orders of magnitude smaller than at room temperature. However, the temperature rise still is only in the order of μK . To detect such small temperature changes very sensitive thermometers are needed.

2.2.2 Transition Edge Sensors

A *transition edge sensor* (TES) is such a very sensitive thermometer. It consists of a thin superconducting film which is operated in its transition from normal- to superconductivity. A typical transition curve of a TES is shown in figure 2.3.

An energy deposition in the absorber crystal leads to a temperature rise in the TES, which is $\mathcal{O}(\mu\text{K})$. Due to the steep superconducting transition of the TES, a small change in temperature leads to a measurable resistance change ($\mathcal{O}(\text{m}\Omega)$).

During operation the TES is stabilized in a certain point in its superconducting transition - the *operating point*. In order to keep the TES in its operating point each TES is equipped with a heater, with which the temperature of the TES is controlled. After an energy deposition the heat has to be removed from the TES, which is achieved by a weak thermal connection to the heat bath with a temperature below the

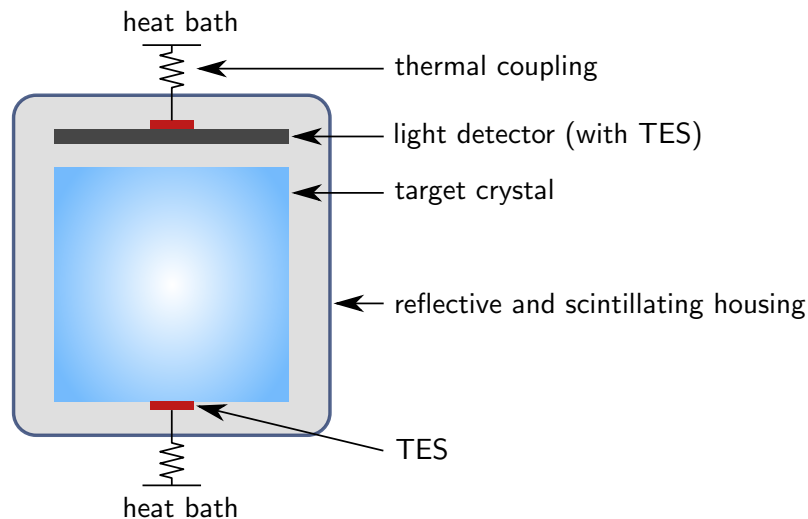


Figure 2.4: Schematic drawing of a conventional detector module. The light detector is mounted on top of the phonon detector. Both detectors are equipped with a TES thermally coupled to the heat bath. The detectors are surrounded by a reflective and scintillating housing.

transition temperature. Details about the detector operation can be found in section 2.4.

In CRESST the TES are made of a tungsten film being 200 nm thick, with a transition temperature typically between 10 and 30 mK. These films are evaporated, either directly on the absorber or on a carrier crystal which is glued on the absorber crystal with an epoxy resin. For the electrical connection, necessary for readout, an aluminum film is evaporated partly on top of the tungsten film and connected with an aluminum bond wire. The thermal connection to the heat bath is realized with a sputtered gold film and a gold bond wire.

2.2.3 Detector Module

CRESST detectors are operated as *detector modules*. A phonon detector and a light detector are mounted inside a reflective and scintillating housing and together they form a module. The setup of a conventional detector module as mounted in CRESST-II is depicted in a schematic drawing in figure 2.4. In the following all the components are explained in detail. A photograph of an opened detector module is depicted in figure 2.5.

The design introduced here describes the so-called conventional detector module. In CRESST-II phase 2 also different geometries were mounted and are described in section 2.6.

Phonon Detector

On the right side of figure 2.5 the phonon detector is visible. The target material for particle interactions used in CRESST-II is CaWO_4 (calcium tungstate). The absorber crystal is cylindrical with height and diameter of 40 mm and a mass of about 300 g. On

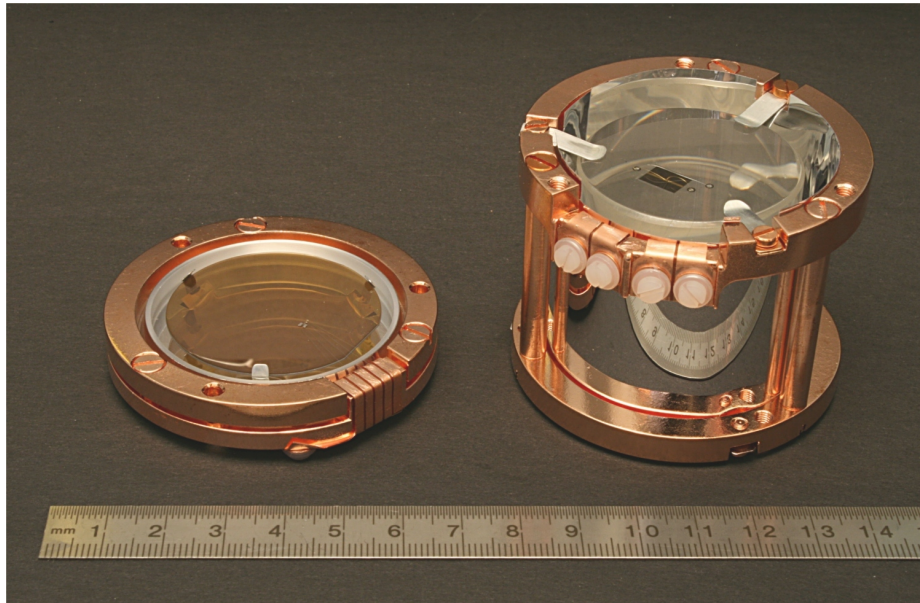


Figure 2.5: An opened conventional CRESST-II detector module. On the left side the light detector, consisting of an SOS absorber and a TES, can be seen. On the right side a phonon detector, consisting of a CaWO_4 absorber crystal and a TES can be seen. Both are mounted with non-scintillating clamps inside a reflective housing. The holder is made of radiopure copper. For operation the light detector is mounted on top of the phonon detector.

top of it the TES with a size of $6 \times 8 \text{ mm}^2$ can be seen. For readout it is electrically connected to the copper structure with thin bond wires. The crystal is held in place by six pairs of bronze clamps (partly visible in figure 2.5), which are coated with aluminum in order to make them reflective.

A recoil in the CaWO_4 crystal produces mainly phonons that are detected with the TES on the crystal. Additionally, a small fraction of the deposited energy is transformed into scintillation light, which is detected with the light detector. For e^-/γ -interactions about 1-3% of the deposited energy is detected in the form of scintillation light [57]. The maximum scintillation emission wavelength at room temperature is in the range of 420 nm to 425 nm [58]. The crystal side facing the light detector is roughened to increase the light output [59]. In figure 2.6 two scintillating CaWO_4 irradiated with UV light crystals are shown.

The setup of the CRESST detector module allows to use any inorganic scintillator as target material. Several materials such as ZnWO_4 , CaMoO_4 , CdWO_4 , titanium doped Al_2O_3 and CsI were investigated in [60–63]. However, so far CaWO_4 was found to be the most suitable material for CRESST in terms of light output at low temperatures, intrinsic radiopurity as well as the performance as cryogenic detector.

Light Detector

On the left side of figure 2.5 the light detector in its copper holder is depicted. The light absorber is made of silicon-on-sapphire (SOS), which is a sapphire wafer with a

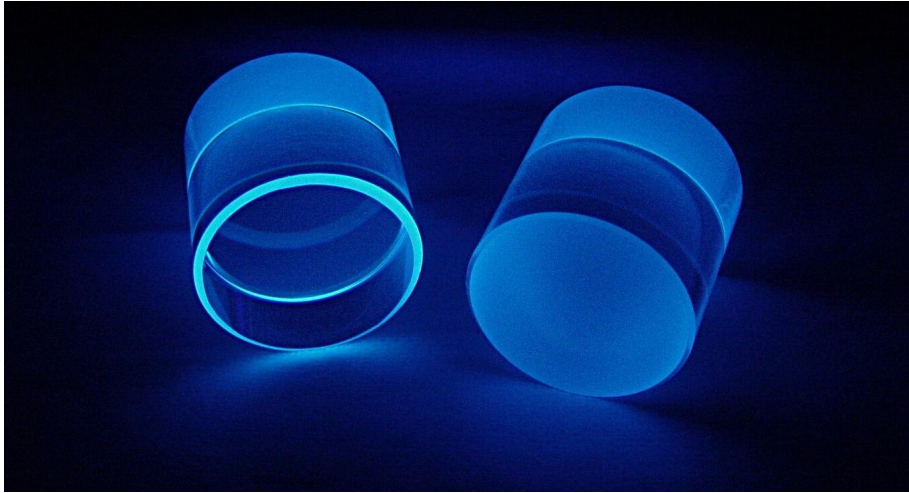


Figure 2.6: Two scintillating CaWO_4 crystal irradiated with UV light. The scintillation light is in the blue range of the visible spectrum. The front face of the right crystal is roughened which visibly homogenizes and enhances the light output.

1 μm epitaxially grown silicon layer on one side. The round absorber has a thickness of 0.46 mm and a diameter of 40 mm. The light detector is held by three bronze clamps, which can also be seen in figure 2.5.

Like the phonon detector, also the light detector is operated as cryogenic calorimeter. The light absorbed by the silicon layer is transformed into phonons, which can be absorbed by the thermometer film. The thermometer is another TES, much smaller than the one of the phonon detector. Similar to the phonon detector TES, it is also connected with bond wires to copper pads on the copper structure.

Besides the SOS-light detectors, also pure silicon is a suitable material which can be used as light absorber.

For operation the phonon detector is paired with the light detector inside a reflective and scintillating housing, which is mainly made of a polymeric foil. A high reflectivity of the surrounding materials increases the fraction of scintillation light, that can be absorbed by the light detector. The scintillation property is needed for background discrimination (see section 2.3). The surrounding supporting structure is made of highly radiopure copper.

2.3 Active Background Discrimination

Despite the massive shielding around the experimental setup, the background rate is still much higher than the expected dark matter interaction rate due to an intrinsic contamination of the crystals and the detector housing. However, the scintillation property of the target crystal and the pairing of phonon and light detector in a module allows to actively discriminate background.

2.3.1 Light-Phonon Technique

Phonon and light detector are paired in a detector module and are read out simultaneously. When a particle interaction in the target crystal happens, two coincident signals are measured - one from the phonon and one from the light detector. The fraction of these two signals depends on the type of interaction and, therefore, this effect allows an active background discrimination.

The fraction of energy deposited in the absorber and transformed into phonons is measured by the thermometer of the phonon detector. As the relative amount of deposited energy transformed into phonons is nearly independent of the interacting particle, the phonon signal can be used to determine the total amount of the energy deposited very precisely².

On the contrary, the amount of produced scintillation light strongly depends on the type of interacting particle. Therefore, the light signal is used to discriminate between different types of interacting particles.

The principle can be seen in figure 2.7, where a target crystal was irradiated with a ^{57}Co γ -source and a ^{90}Sr β -source (left plot). The energy measured in the light channel is plotted against the energy measured in the phonon channel. Events from the electron- and γ -source, as well as the background events are located in an approximately linear band. This shows that the produced light is proportional to the energy deposited in the phonon detector. Typically, the light channel is calibrated so that this band has a slope of one. By this calibration the energy measured in the light channel is assigned with the unit keV_{ee} , where the subscript “ee” stands for electron-equivalent. Details on the calibration can be found in section 2.5.

In the measurement shown on the right side of figure 2.7 a neutron source was added and events in a second band, with a slope reduced by a factor of about ten, appear. This band is formed by neutron interactions, which produce less light than a gamma with the same energy in the phonon channel.

The reason for this difference is that the particles interact differently in the crystal. Particles that interact electromagnetically, like electrons and gammas, transfer energy on the electrons of the crystal atoms. A small fraction of this energy is transformed into scintillation light. Neutrons instead, mainly deposit energy on the oxygen nuclei, which themselves recoil in the crystal afterwards and, thereby, produce a lower amount of light. The produced scintillation light differs even for different nuclei in the way that the heavier the nucleus, the less light is produced [66]. This effect is called *light quenching* and is exploited in CRESST to distinguish different interaction types.

Light Yield - Energy Plane

The discrimination parameter used in CRESST is the *light yield* LY . The light yield of an event is defined as the energy measured in the light channel L divided by the energy measured in the phonon channel E_p :

$$LY := \frac{L}{E_p}. \quad (2.2)$$

²The fraction of energy escaping the crystal as scintillation light can even be taken into account in order to make the measured energy independent of the particle type [64].

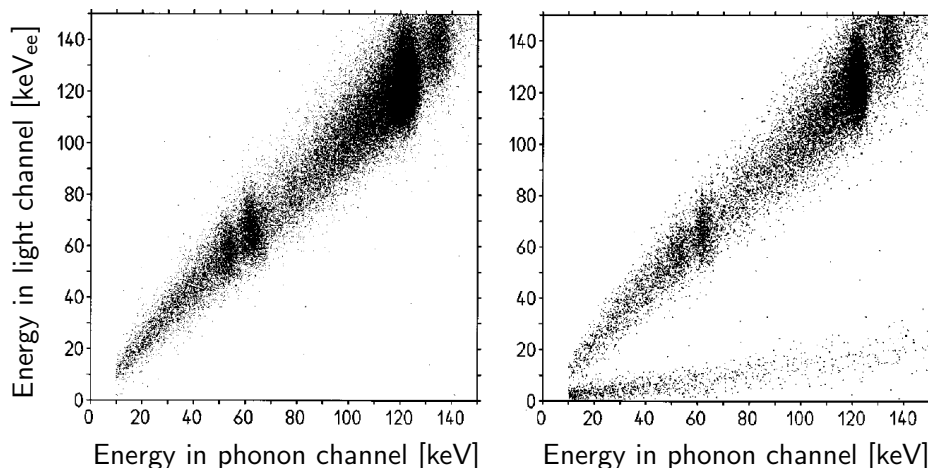


Figure 2.7: Both plots show the energy measured in the light detector against the energy measured in the phonon detector. In the measurements shown on the left the detector was irradiated with a ^{57}Co γ -source and a ^{90}Sr β -source. The electron- and γ -events, as well as the background events, appear in one band. The light channel is calibrated so that this band has a slope of one. In the measurement on the right side a neutron source was added. The neutron events appear in another band with a smaller slope. Image taken from [65].

The common way to illustrate CRESST data is in the *light yield - energy plane* where the different event populations appear in roughly horizontal bands. Figure 2.8 shows a light yield - energy plot with data of the module named TUM40 operated in the latest data taking phase of CRESST-II phase 2. Due to the calibration scheme, the main background, consisting of electron and γ -events, appears around a light yield of 1.

The other bands have reduced light-yield according to their *quenching factor* QF . A precise measurement of the quenching factors was performed in a dedicated experiment by irradiating a cryogenic detector with a fast neutron beam produced by an accelerator [68]. Although an energy dependence of the quenching factors is observed over the total measured energy range, for energies of 10–40 keV they can be approximated as constant values. These values are summarized in table 2.1. A description of the energy dependence for electron-recoils is given in appendix B. More details on the quenching factors can be found in e.g. [68, 69].

The upper and lower 90 % boundaries of the oxygen and tungsten nuclear recoil bands are drawn in black and red in figure 2.8, respectively. Thus, they enclose the region where the central 80 % of the respective events are expected. The calcium recoil band, which is located between the oxygen and tungsten band, is not drawn for reasons of clarity.

The two-channel detection enables an active discrimination on an event-by-event basis. However, the capability of this discrimination depends on several aspects. Background and signal can only reliably be discriminated where the bands are clearly separated. At low energies the different bands overlap and events inside one band can no more be attributed to a single event type. As the width of the bands is mainly given by the resolution of the light detector, the light detector determines the discrimination

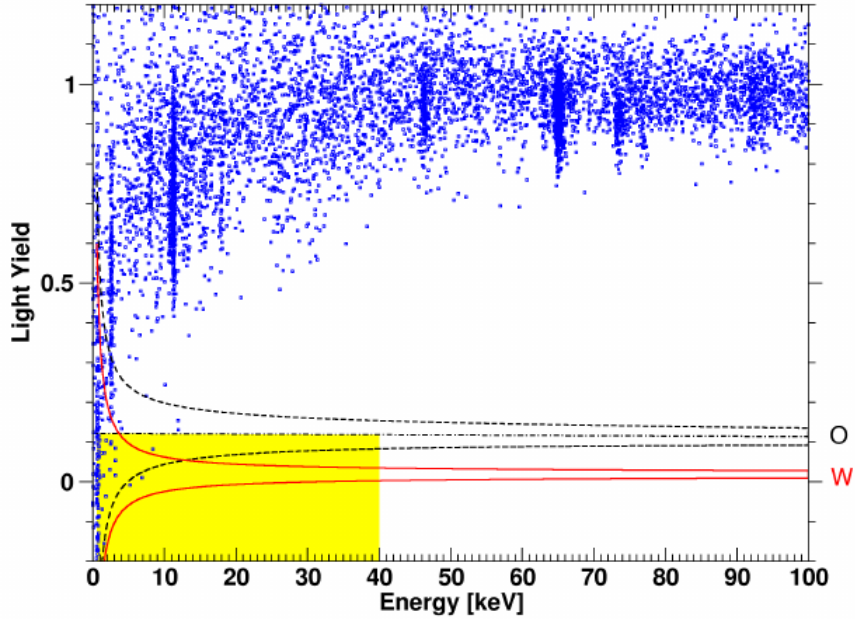


Figure 2.8: Data of the detector module TUM40 operated during CRESST-II phase 2 illustrated in the light yield - energy plane. The measured events are drawn as blue dots. The electron and γ -background appears in a roughly horizontal band around a light yield of 1. The lines correspond to the 80% boundaries of the oxygen (black) and tungsten (red) recoil bands. The calcium band, lying between the oxygen and tungsten band is not shown for clarity. Additionally the region of interest for dark matter search is marked in yellow. Image taken from [67].

power of the different bands.

Moreover, the event-by-event discrimination requires, that signal and background are expected to appear in different bands. While this is true for the dominant background due to electrons and gammas, this is not the case for neutrons. As mentioned before, neutrons scatter off nuclei like expected for dark matter and, thus, are a very dangerous background.

Due to kinematic reasons, neutrons mainly interact with oxygen nuclei. Depending on the mass of the dark matter particle, the dominant scatter partner changes. In the following the aspects, that determine the distribution of detectable dark matter recoils, are discussed.

Target Nuclei for Dark Matter Particles

As discussed in section 1.4 the expected dark matter particle-nucleus scattering cross-section scales as A^2 with the mass number A of the target nucleus. Thus, in CaWO_4 , consisting of tungsten ($A_W \approx 184$), calcium ($A_{Ca} \approx 40$), and oxygen ($A_O \approx 16$), dark matter is expected to mainly scatter off tungsten nuclei.

However, due to the finite energy threshold of the detector, interactions with an energy deposition below threshold cannot be detected. Therefore, it is necessary to

particle type	QF
e^- , γ	1
O-recoils	0.112
Ca-recoils	0.0594
W-recoils	0.0172

Table 2.1: The quenching factors (QF) for CaWO_4 in the energy region of 10–40 keV. Although a tiny energy dependence is observed, in this energy region it is valid to approximate the quenching factors as constants. Values taken from [68].

consider the number of detectable counts, i.e. the counts with an energy deposition above threshold.

In the case of a heavy dark matter particle (above $\sim 30 \text{ GeV}/c^2$) the majority of detected events is expected to be tungsten scatters, as heavy particles can transfer energy efficiently to a heavy tungsten nucleus. Thus, it is possible to only consider the tungsten band in the analysis [70]. If there is neutron background, a possible dark matter signal could be discriminated, since neutrons and dark matter scatters appear mainly in different bands.

However, a lighter dark matter particle is only able to transfer a lower amount of energy to a heavy nucleus. This energy may be below the energy threshold and therefore not detectable, whereas the energy they can transfer to a calcium or oxygen nucleus might still be in the detectable range. The amount of detectable recoil events depends on the mass of the dark matter particle and on the energy threshold of the detector.

In figure 2.9 the number of detectable recoil events for an energy thresholds of 0.3 keV (solid lines) and 10 keV (dashed lines) for dark matter particle masses of 0.5 to 1000 GeV/c^2 are shown in black. Additionally, the respective number of the counts recoiling on each nucleus are drawn in colors.

For both thresholds the fraction of tungsten events dominates for higher masses. However, below a certain mass, dark matter particles cannot transfer an energy above the threshold energy to a tungsten nucleus and then calcium and oxygen recoils dominate. This mass depends on the threshold and is at $\sim 3 \text{ GeV}/c^2$ for a threshold of 0.3 keV and $\sim 17 \text{ GeV}/c^2$ in case of a detector with a threshold of 10 keV.

In summary, this shows that it is beneficial to consider all nuclear recoil bands for dark matter search, as this not only increases the number of detectable events but, in addition, extends the range of detectable dark matter particles to lower masses. Therefore, in CRESST all three nuclear recoil bands are taken into account for the dark matter analysis [67].

Another important aspect that was already mentioned in section 1.4 and is shown also in figure 2.9 is the advantage of a low energy threshold. A lower energy threshold does not only allow to detect lighter dark matter particles but additionally increases the amount of detectable events for all masses.

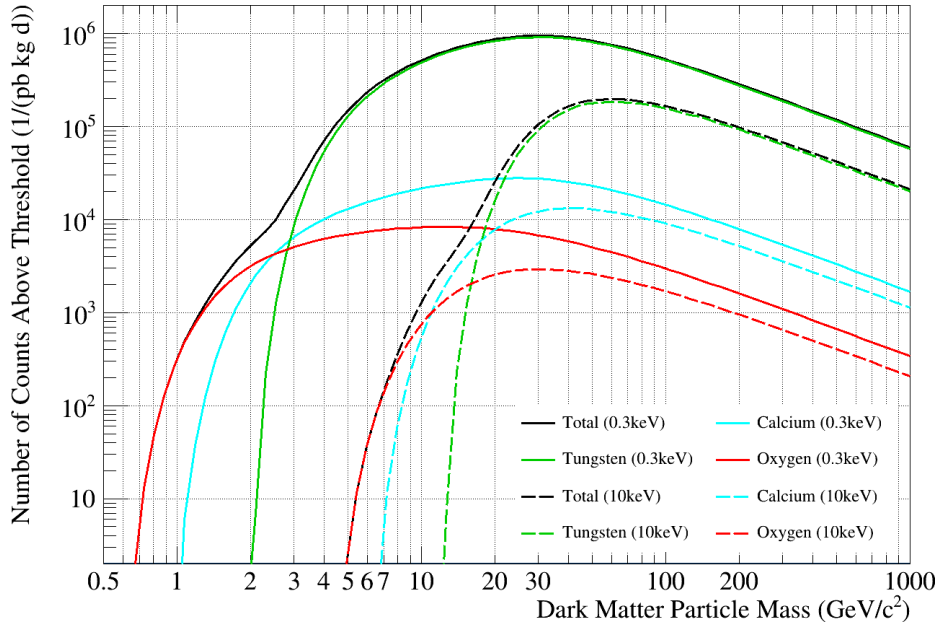
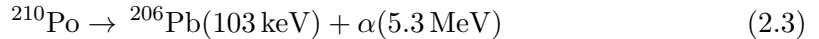


Figure 2.9: Number of counts above threshold for dark matter particle masses of 0.5 to 1000 GeV/c^2 with an energy threshold of 0.3 keV (solid black) and 10 keV (dashed black). The fraction of events for each nucleus is shown in colors. Image taken from [71].

2.3.2 Surface Background Discrimination

A dangerous background for dark matter search are surface contaminations that result in α -decays. The main source for this background is the noble gas radon which is present in ambient air and can be adsorbed on any surface inside the detector housing. The isotope ^{210}Po is a daughter nucleus of ^{222}Rn and decays further via α -emission [72]:



whereby the α -particle and the lead nucleus leave the center of mass in opposite directions.

In general, α -radiation with energies in the MeV-range is no relevant background as such events are far off the region of interest for dark matter search. However if the nucleus decays just below the surface of a surrounding material, the α -particle can loose most of its energy and appear in the α -band at low energies.

The even more dangerous background arises, when the Pb-nucleus hits the crystal. As it is even more heavy than tungsten, its quenching factor is lower than the one of tungsten and, therefore, it appears in a band just below the tungsten band and cannot be separated from tungsten nuclear recoils. The background induced by the lead nucleus is illustrated in figure 2.10. Two cases have to be distinguished, where the ^{210}Po -nucleus decays on (or slightly below) the surface of the crystal or of a surrounding material.

If the decay happens on or slightly below the surface of the crystal, at least the full energy of the ^{206}Pb -nucleus (103 keV) is detected plus a possible contribution from the α -particle (upper part of figure 2.10). In this case the total detected energy is far above

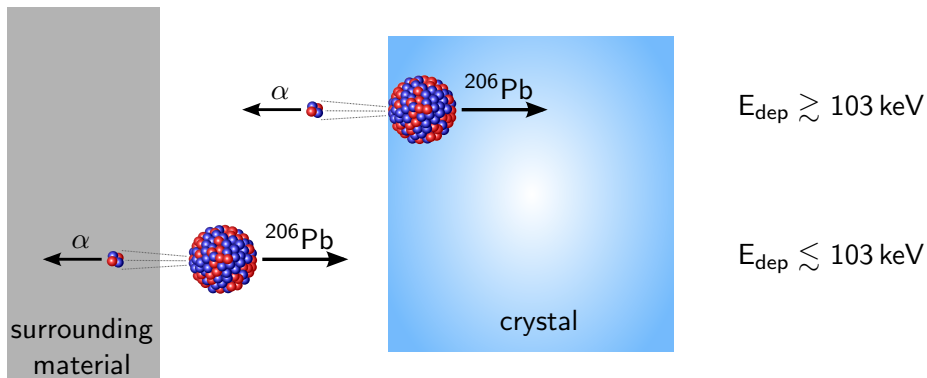


Figure 2.10: Background events due to the decay of ^{210}Po . The isotope can be present on or be implanted in the surface of the crystal (top). When the decay happens on or in the surface of the crystal an energy of $\gtrsim 103 \text{ keV}$ is deposited in the crystal. However, the isotope can also be present on or implanted in a surrounding material (a clamp or the reflective foil). In this case energies of $\lesssim 103 \text{ keV}$ can be deposited in the crystal by the ^{206}Pb -nucleus and can leak into the region of interest.

the energy relevant for dark matter search ($\geq 103 \text{ keV}$).

If a surrounding surface (either the reflective foil or on the clamps) is contaminated with ^{210}Po dangerous background events might appear. When the ^{210}Po -nucleus decays on a surface, the ^{206}Pb -nucleus can hit the crystal, while the α -particle escapes undetected (lower part of figure 2.10). In this case the maximal energy of 103 keV is deposited in the crystal. However, if the ^{210}Po -nucleus is implanted in the surface it can lose energy while escaping. Thereby, energies down to zero can be deposited in the detector. As such recoils produce very little light, they can appear at low light yields and low energies and, therefore, can mimic dark matter recoils.

Such an event can be vetoed if the surrounding material is scintillating and produce additional light when a particle deposits energy in them. Thereby, the event is located at a higher light yield and shifted out of the nuclear-recoil bands in the light yield - energy plane.

For that reason, the polymeric foil surrounding the detectors is not only reflective but also scintillating. Additionally, there are scintillating rings used that guide the foil and reduce the openings in the foil, needed for the bonding wires. However, in the conventional detector module, the metal clamps that are used to hold the detectors in place are not scintillating. There were several attempts to cover the metal clamps with a plastic scintillator but this induced thermal stress relaxation events (i.e. events without a corresponding light signal) [63]. Although these events may have a slightly different pulse shape, they cannot be efficiently discriminated of particle events at low energies.

In CRESST-II phase 1 a ^{210}Po contamination in the clamps was the dominant background source [73]. For phase 2 a new clamp material was fabricated for the conventional modules [63]. Additionally, three new module designs, that feature a fully-scintillating or a fully-active housing, were installed. However, in all conventional modules equipped with the new clamp material events from surface backgrounds with a reduced intensity compared to phase 1 were observed [74]. Instead, the newly developed module designs

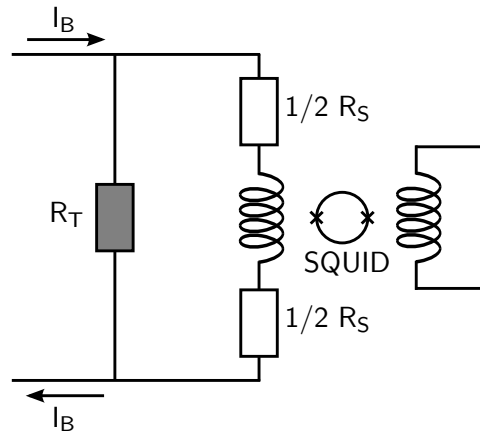


Figure 2.11: Readout circuit used to measure the change of the thermometer resistance R_T . A constant bias current is sent through the two parallel branches - one with the thermometer and the other with the two shunt resistors with a total resistance of R_S each and the input coil of the SQUID. The SQUID outputs a voltage proportional to the current through its input coil.

efficiently veto all surface related background [67] (see section 2.6).

2.4 Data Taking

Up to now it is described that an energy deposition in the target crystal leads to a resistance change in the phonon and light detector. This section describes how the signal is read out and which electronic components are needed for detector operation.

2.4.1 SQUID-based Readout

The readout of the resistance change is done with a SQUID (Superconducting Quantum Interference Device), which is a very sensitive device for measuring small current variations. The detector is connected in the readout scheme shown in figure 2.11 [75]. One branch of the parallel circuit contains the thermometer, while in the other branch the input coil of the SQUID and two identical shunt resistors, with a resistance of R_S in total, are connected. A constant bias current I_B (typically of some μA) is sent through the two branches. Thereby, a change of the thermometer resistance will change the branching of the bias current and thus the current measured by the SQUID. The SQUID outputs a voltage which is proportional to this current with a constant offset. This offset is normally irrelevant and, therefore, is subtracted when a pulse is displayed.

In summary, a temperature pulse is converted in a voltage pulse, which is then recorded and stored on disk.

2.4.2 Detector Operation and Data Acquisition

A simplified diagram of the electronics used to read out the SQUID signals and to operate a single detector is shown in figure 2.12. The bias supply chain is shown in black, the readout chain and the trigger system are shown in blue while the heater chain is drawn in red.

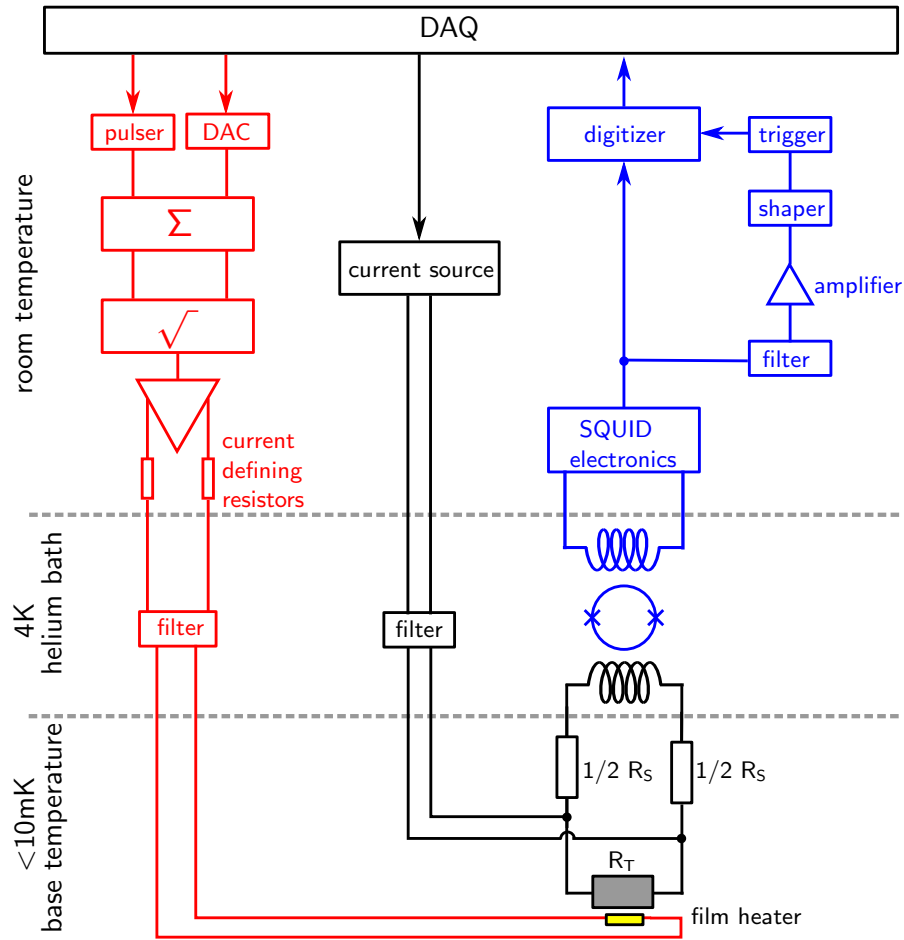


Figure 2.12: Simplified diagram of the electronics used for detector operation and data acquisition. The readout circuit containing the SQUID and the trigger system is shown in blue. The detector bias chain is drawn in black and the heater system for detector stabilization is drawn in red. For details see text.

Bias Supply Chain

The constant bias current for the detector is provided by a floating current source located at room temperature. The bias current is typically of some μA and is optimized for maximum signal during the set up of the detectors.

The detectors are operated at the base temperature of the cryostat ($<10\text{ mK}$) and the SQUIDS are mounted in the liquid helium bath of the cryostat at 4 K. To reduce high frequency noise low pass filters (10 kHz) are installed in the lines connecting the electronics to the detectors.

Signal Readout Chain

The output signal of the SQUID is transferred out of the cryostat into the SQUID electronics. There it is split into two branches with one branch directly being sent to a digitizer unit, which continuously samples the signal with a sampling rate of 25 kHz

(one sample every 40 μs). In the other branch, the signal is amplified and AC-coupled to a trigger unit, which sends a signal to the digitizer when the signal level exceeds an adjustable threshold. When this happens, the digitizer saves a record of 8192 samples which are read out and saved to hard disk. The first quarter of the record happened before the trigger signal and is therefore, called pre-trigger region. It is mainly used to evaluate baseline parameters whereas the other three quarters, called post-trigger region, contain the actual pulse information.

When one detector of a module triggers the digitizer, also its partner channel is read out regardless of a trigger so that each record contains a phonon signal and the corresponding light signal. This ensures that always both pulses of phonon and light detector are stored together and the event-by-event discrimination can be applied.

Heater Chain

During operation each detector is stabilized in its operating point in the superconducting transition, which is typically chosen so that the signal height is maximal. For stabilization a current is sent through the heater structure on each detector. The total heating current consists of two components: Firstly, a quasi-constant heating current is needed to keep the detector in its operating point. This contribution is controlled by a DAC (Digital-to-Analog Converter) which outputs a variable voltage proportional to the desired heating current. Additionally, heater pulses with different amplitudes are injected in regular time intervals. They are generated with a wave form generator and shaped that detector pulses similar to particle pulses result. The sum of the constant current and the heater pulses is sent through an analog square-rooter³ and converted to the heating current by a pair of resistors.

The types of heater currents are control pulses and test pulses, which both have a different purpose.

Control Pulses for Stabilization As particle interactions in the crystal lead to temperature changes of $\mathcal{O}(\mu\text{K})$, the temperature of the thermometer has to be stabilized with at least this precision. Therefore, heater pulses with a large amplitude - so-called control pulses - are sent to the thermometer every six seconds. They heat the thermometer completely out of transition and, therefore, their pulse height is a measure of the distance to the top of the transition. The pulse height is an input for a PI (proportional-integral) control loop which adjusts the heating current to keep the detector at its operating point.

Test Pulses for Energy Calibration One so-called test pulse is sent every five control pulses. Test pulses are smaller heater pulses of several different amplitudes. They allow for a calibration down to threshold energies, where no external γ -source can be used. In addition, they are also used to correct variations of the detector response over time and they allow to directly determine the trigger threshold [67, 74].

³The purpose of the square rooter is to decouple the constant heating current from the heater pulses. As the power dissipated in the detector is proportional to the square of the total heating current, with the square-rooter the energy injected via a heater pulse remains the same independently of the constant heater current.

2.5 Basic Concepts of Data Analysis

In the offline analysis for each record several parameters are evaluated. In the following an overview of the basic concept of the data analysis performed in CRESST-II is given. The aspects important for the measurements done within this work are in particular discussed. More details on the data analysis techniques used in CRESST are given in [71, 76].

2.5.1 Pulse Height Evaluation

The height of a recorded pulse is a measure of the energy deposited during an interaction. Thus, the determination of the pulse height must be accurate. Using simply the maximum of the pulse leads to an overestimation of the pulse height as the maximum would be preferentially found where an upward noise fluctuations occurs.

Another aspect is, that the pulse shape changes for larger pulses, which is related to the shape of the superconducting transition of the TES. In general, close to the operation point the transition is linear, meaning $\Delta R/\Delta T$ is constant in this region and for small pulses the pulse shape stays the same. However, at the top of the transition $\Delta R/\Delta T$ becomes zero (and the transition curve becomes flat). This can be observed in the pulses in the same way, that they become flat on top. With a *template fit* this can be compensated for and the “real” pulse height, which is called amplitude, is determined.

Template Fit

For the template fit method first a *template pulse*, which describes the observed pulse shape, is required. To generate this template pulse, a set of some hundred pulses is averaged. These pulses are typically selected to have almost the same pulse height in the linear regime. Furthermore, strict selection criteria are applied, so that they provide a good description of the pulse shape. Typically, pulses induced by 122 keV γ 's from a ^{57}Co calibration source are used. Due to the averaging the template pulse has a reduced noise contribution. It has to be generated for each pulse type separately (e.g. for particle and heater pulses).

In the template fit, the template pulse is fitted to each pulse separately and three free parameters are adjusted:

- The *baseline offset* describes the absolute level of the baseline. The baseline can be described by a constant or a baseline model (e.g. an exponential that describes pile-up).
- The *pulse amplitude* is determined by scaling the template pulse.
- The *pulse onset* is determined by shifting the template in time.

The result of such a template fit is shown in figure 2.13. The deviation of the recorded pulse from the template is given by the RMS (root-mean-square) value which is minimized during the fit. It is calculated for each pulse and quantifies the quality of the fit.

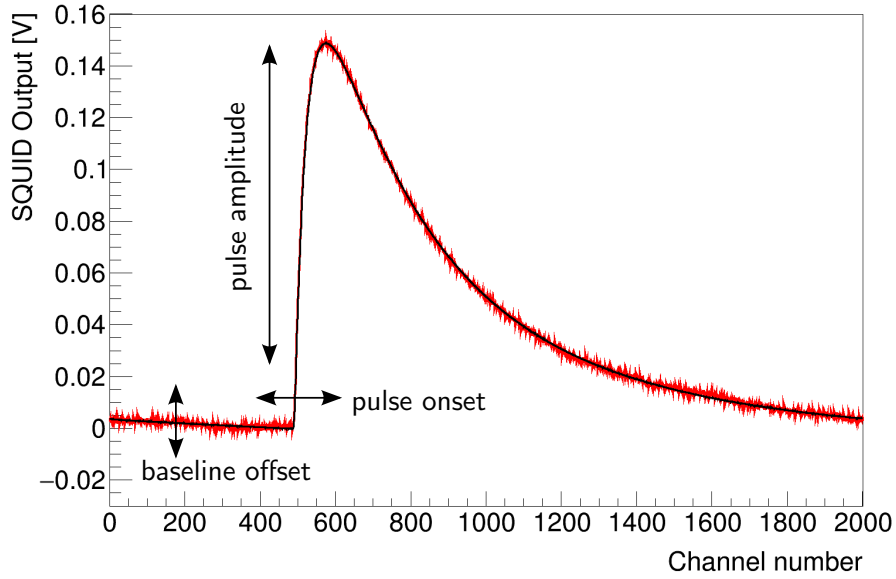


Figure 2.13: Data of a particle pulse (red) shown together with the result from a template fit (black). The three parameters, that can be varied to best match the template to the pulse, are indicated with arrows.

Truncated Fit

The determination of the pulse amplitude only works reliable in the linear regime of the transition. Higher energetic recoils heat the TES in its nonlinear region, which changes the pulse shape. This can be observed in a rise of the RMS of the fit for higher pulses, due to the reduced fit quality for pulses with a different shape (see figure 2.14).

The region where the pulse shape starts to change is usually far above the energies interesting for dark matter search. However, for the characterization of background sources and the performance of the detectors, these pulses are also reconstructed in the analysis.

To increase the fit quality, in the so-called *truncated fit* parts of the pulse, that are in the nonlinear regime of the transition are excluded from the fit. By doing so, only the linear part of the pulse is considered for the fit with the low-energy template and the resulting amplitude is an extrapolation of the low-energetic part of the pulse. The limit above which samples are not considered for the fit anymore is chosen from the RMS distribution (see figure 2.14) and is called *truncation limit*. With this method pulses with energies up to some MeV can be reconstructed reliably [77].

Correlated Fit

In CRESST phonon and light detector pulses are measured simultaneously. As more energy is deposited in the phonon detector, usually phonon pulses have a larger signal-to-noise ratio than light detector pulses. For this reason, for small energies phonon pulses can still be fitted well, whereas light detector pulses are often more difficult to fit. The fact that the pulse onset must be the same for both pulses is exploited in the *correlated fit*, where both pulses are fitted with a common pulse onset.

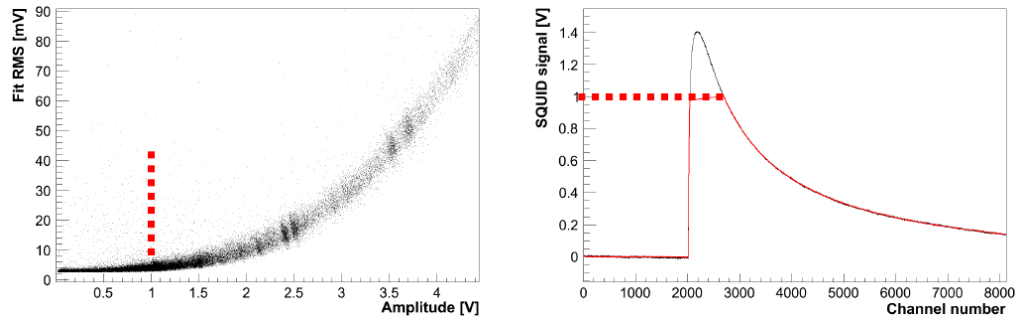


Figure 2.14: Pulses exceeding the linear range of the transition cannot be fitted properly with a low energy template, since the pulse shape changes in the non-linear region. The different pulse shape results in a decrease of the fit quality and is indicated by an increase of the RMS value for these pulses (left). With the truncated fit (right) pulses with a higher energy are reliably reconstructed as only the linear part is used for the fit. The truncation limit is set where the RMS distribution starts to increase (dashed red line, here: 1V pulse height). Image taken from [63].

To do so, the templates for both pulses must be summed from the same set of pulses so that the relative onset time is fixed. In the correlated fit the templates are fitted to the pulses and, thereby, even very small light detector pulses can be fitted correctly due to the known relative timing of both pulses. The best fit is found by minimizing the sum of the RMS values of both signals.

2.5.2 Energy Calibration

For the absolute energy calibration of CRESST-II detectors an external γ -source is used. Usually the 122 keV-line of a ^{57}Co source is used to fix the energy scale⁴. In case of the light detector, the detected scintillation light from the 122 keV γ 's hitting the target crystal, is fixed as 122 keV_{ee}. Thereby the energy scale of the light detector is set with the *electron-equivalent energy*⁵. Due to this definition the light yield is 1 at 122 keV.

With the calibration source the energy scale is fixed only at one point and at the time when the calibration takes place. As already explained, during a measurement test pulses are sent to every detector heater regularly. They are used to calibrate the detector over an energy range from threshold up to MeV energies and to compensate for variations in the detector response over time.

Over the whole measurement period every ~ 30 s one test pulse is injected in the heater. The test pulses can have up to twelve different amplitudes in order to obtain pulses with energies corresponding to energies which are relevant for the measurement. Similar to particle pulses the amplitude of the test pulses is obtained via a correlated

⁴A lower energetic calibration source would be closer to the energies that are aimed to be measured. However, such a source would not be able to penetrate the in total 12 mm thick copper shields around the detectors.

⁵In general it is possible to calibrate the light detector absolutely with a low-energetic γ -source directly hitting the light detector

truncated standard event fit. The test pulses serve two purposes:

- Variations of the detector response in time can be corrected by fitting splines to the measured test pulse amplitude. With this the detector response can be evaluated at any point in time.
- As the energy deposited by a test pulse is proportional to the injected voltage, the test pulse amplitude can be used to linearize the detector response. To obtain a continuous response function (i.e. the relation between the injected test pulse amplitude and the corresponding measured pulse amplitude) over the whole energy range of interest, pulse heights resulting from discrete injected test pulse amplitudes are fitted with a low-order polynomial, which then serves to determine the energy from the pulse height.

From the calibration with the ^{57}Co source a relation between the injected voltage and the energy deposited in the target can be evaluated. Thereby, the detector can be calibrated for the whole measurement period and for all energies.

2.5.3 Cuts

For the analysis of CRESST detectors invalid pulses that are not induced by particle events (such as electronic disturbances) or particle events that are not properly energy reconstructed due to artifacts in the record, are removed from the data set. This is done by several data cuts identifying invalid pulses. In the following only a brief overview of the most important cuts, used for the measurements of this work, is given. A more detailed description of the cuts used in the dark matter analysis of CRESST can be found in [71, 76]. The following cuts are applied on the data set:

Stability Cut Time periods in which the detector was not running stably in its operating point (e.g. due to external disturbances) are rejected by the stability cut. This is done by evaluating the height of the control pulses, which is a measure for the detectors operating point in the transition (see section 2.4). For time periods, where the control pulse height deviates significantly from the set value, all records are completely removed from the data set.

Coincidence Cut Due to the low expected cross-section of dark-matter particles it is nearly impossible that the latter interact twice in the CRESST setup. Thus, all cryogenic events which are coincident in time with either a signal from the muon veto or another detector module are rejected by the coincidence cut.

Data Quality Cuts Several cuts are designed to identify invalid pulses where the energy reconstruction does not work properly. For example records that include SQUID resets or that triggered on noise are removed by these cuts. Also pulses with a different pulse shape (such as events in the TES carrier of a phonon detector) are removed by dedicated cuts. The most important and most generic data quality cut is a cut on the RMS value of the template fit, where pulses with measured shapes that deviate from the expected signal shape, are discarded. This includes strongly distorted pulses, pulses with a strong baseline tilt or pile-up events, i.e. samples where more than one pulse appears in the time window recorded.

After applying all cuts, the collected exposure needs to be calculated and afterwards either a limit on the dark matter particle-nucleon cross-section can be given or, if events in the ROI are observed, a hint for a possible dark matter signal can be calculated. These steps are explained e.g. in [71, 76]. In the following section only the results of the previous CRESST-II dark matter data-taking phases are explained.

2.6 Status and Future Strategy of the CRESST experiment

Results of different direct detection experiments are usually compared in a plot of dark matter particle-nucleon cross-section versus dark matter mass. For the calculation of the expected recoil energy spectrum all experiments assume standard parameters, as explained in section 1.4. The lines in figure 2.15 mark limits, where the parameter space above is excluded by the corresponding experiment, whereas colored regions mark favored regions of a possible hint for dark matter. The latest results of CRESST, which are explained in the following, are included in figure 2.15. Additionally, for comparison the leading limits of other experiments, as discussed in section 1.4, are shown in the same figure.

CRESST-II performed two extended physics runs, which are conventionally referred to as phase 1 and phase 2. In phase 1 a net exposure of 730 kg days was collected between 2009 and 2011 [73]. In this data 67 events were observed in the acceptance region, in which events are accepted as possible dark matter scatters in the analysis. A likelihood fit was performed to determine the parameters of the background model. Additionally, a possible signal contribution was included in the likelihood. Less than half of the observed events could be explained by known backgrounds, including leakage of e^-/γ -events, events from neutrons, from α -particles, and from recoiling ^{206}Pb nuclei. The additional events might be either explained by an unknown background contribution⁶ or by scatterings of WIMPs. It was found that the likelihood function has two maxima, which are denoted as M1 and M2 and are illustrated in figure 2.15 in the parameter space for dark matter particle-nucleon scattering. The two regions mark the 90% confidence region for both maxima⁷.

2.6.1 CRESST-II Phase 2

As the backgrounds and the potential signal were in the same order in CRESST-II phase 1 and the uncertainties in the background models were large, the major goal of CRESST-II phase 2 was to clarify the nature of the signal excess above background.

⁶A possible explanation for the excess events was published in [78]. Simulations showed that the energy spectrum of radon-induced events can have a steep rise at low energies due to sputtering in the surrounding materials, when the surface roughness of these materials is not neglected.

⁷The presence of two maxima can be ascribed to the presence of different nuclei in the target material CaWO_4 . M1 describes a possible WIMP with a mass of $m_\chi = 25.3 \text{ GeV}/c^2$ which is heavy enough to produce detectable recoils of tungsten, whereas the lighter WIMP ($m_\chi = 11.6 \text{ GeV}/c^2$) described by M2 only produces detectable scatters off oxygen and calcium nuclei. Both possibilities lead to a similar spectral distribution in terms of recoil energy and could in principle be discriminated by the light yield distribution of the signal events. However, in this measurement the overlap of the three nuclear recoil bands was too large for this, due to the finite resolution of both, phonon and light detector.

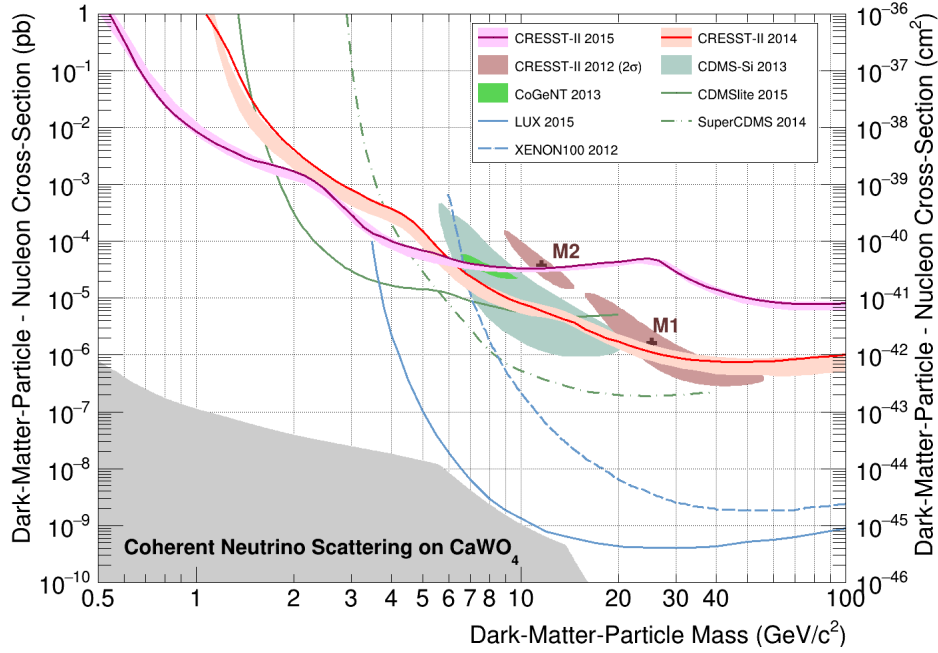


Figure 2.15: Parameter space for elastic spin-independent dark matter nucleon scattering. The favored parameter space reported by CRESST-II phase 1 [73] is shown as brown region. The exclusion limits of CRESST-II phase 2 of the modules TUM40 [67] and Lise [74] are shown in red and magenta, respectively. Additionally the expected sensitivities from a data-driven background model (1σ confidence limit (C.L.), light red and light magenta band) are displayed. For comparison, exclusion limits (90% C.L.) of liquid noble gas experiments are shown in blue [37, 38], and of germanium-based experiments in green [44, 45]. The favored parameter spaces reported by CDMS-Si [43] and CoGeNT [40] are drawn as green shaded regions. Marked in grey is the parameter space where coherent neutrino-nucleus scattering, dominantly from solar neutrinos, will be an irreducible background for a CaWO_4 -based dark matter search experiment [49].

The aim was to reduce neutron, α and in particular ^{206}Pb recoil backgrounds by more than one order of magnitude. CRESST-II phase 2 has been acquiring data from July 2013 until August 2015. A total of 18 detector modules corresponding to an overall total target mass of 5 kg has been installed.

The data show that the neutron background has been efficiently reduced by the installation of an additional 3.5 cm thick PE shield inside the outer vacuum can. The background of degraded α 's, originating from a bulk contamination of the bronze holding clamps, has been completely removed by introducing a newly produced ultra-pure bronze material [63] for the clamps. However, the background from ^{206}Pb nuclear recoil background could not be completely suppressed in the conventional modules despite efforts in improving material selection and radon-prevention methods [74]. In order to reduce the exposure to radon, the assembling and mounting of the detectors was carried out in radon-depleted air supplied by the CUORE experiment [79]. This background could only be suppressed efficiently in three new actively discriminating detector module designs, that were introduced in phase 2.

Actively Discriminating Module Designs

Actively discriminating modules were designed to efficiently reject surface α -events by only having scintillating and/or active surfaces inside the module. Three different designs, with two modules each, were installed in phase 2. Two of these designs feature a fully-scintillating housing of the detector module. Thereby, events induced by α -decays from all inner surfaces are shifted out of the region of interest by producing an additional light signal (see section 2.3). One design still uses non-scintillating clamps, but instead accomplishes to surround the crystal with only active surfaces.

Module with Big Carrier One design has a large TES carrier with the same diameter as the crystal and a thickness of 7 mm. Thereby, the carrier crystal, glued to the main absorber crystal, can be held by three pairs of clamps, which are covered with the scintillating polymer Parylene C. Events in the absorber and the carrier crystal experience a pulse shape difference, which is exploited in a pulse-shape analysis to discriminate possible relaxation events introduced by the parylene [76]. This module is mounted together with a standard light detector. Details about the performance of one of these modules can be found e.g. in [76].

Module with Si Beaker Light Detector Similar to the first design, the second design also uses a large TES carrier glued to the target crystal. Additionally the crystal is held inside a beaker-shaped silicon light detector. Thereby, the crystal is surrounded by the light detector on all sides except the side glued to the carrier crystal. The geometry is designed so that the absorber crystal has no line-of-sight to the bronze clamps holding the carrier or any other surface than the light detector and the carrier. Again events from the non-scintillating clamps hitting the carrier can be discriminated by pulse-shape analysis. Details about the performance of these modules can be found e.g. in [76].

Crystal Held by CaWO₄ Sticks In the third design the target crystal is held by scintillating CaWO₄ sticks which are held in place by clamps mounted outside the detector housing. In this way, no non-scintillating parts are present inside the housing. Additionally, in this design the crystal is a cuboid instead of a cylinder, for enhanced light output [80]. The light is detected with a standard light detector as in the conventional module. A schematic drawing of this design is shown in figure 2.16. A detailed description of this design can be found in [81].

All three designs performed well and effectively vetoed any ²⁰⁶Pb nuclear recoil background. Therefore, a module housing with fully-scintillating or fully-active surfaces is the solution to suppress all surface-related backgrounds completely.

Crystal Quality

Since 2011 crystals have been grown at the crystal growing facility of the Technische Universität München (TUM) [82]. The aim is to improve the background and increase the light output compared to commercially available crystals. In phase 2 in total four TUM-grown crystals have been installed in actively discriminating modules in the CRESST setup. These crystals show a significant improvement in terms of radiopurity

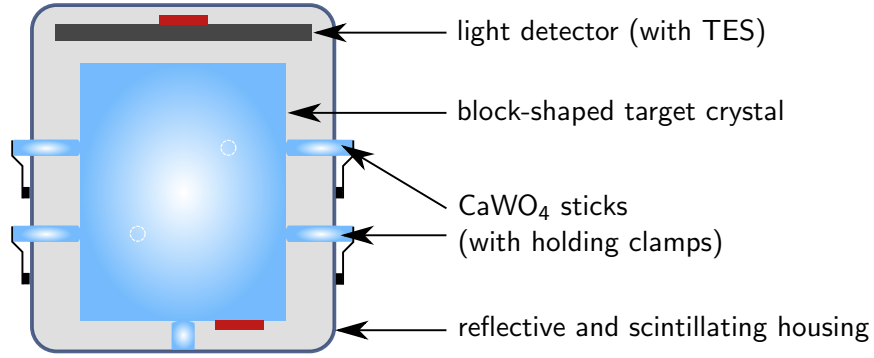


Figure 2.16: Schematic drawing of an actively discriminating module with crystal held with CaWO_4 sticks. The sticks are held with clamps from outside the housing. A standard light detector as used in the conventional modules is mounted above the crystal.

with respect to the commercially available crystals. A lowering of the e^-/γ -background in the ROI by a factor 2 to 10 with respect to commercial crystals (with an average rate of $3.44 / [\text{kg keV day}]$) is accompanied with a significant reduction in the alpha contamination corresponding to a total intrinsic alpha activity of about 3 mBq/kg [77, 83].

Due to the improvement in background in addition to a low threshold of 603 eV the module TUM40 has the best overall performance in phase 2. An analysis of this module, with an exposure of $29.35 \text{ kg live days}$ collected in 2013, was published in 2014 [67]. The superior performance of this module results in a gain in sensitivity for low mass dark matter and an at that time world leading limit on dark matter particles down to $1 \text{ GeV}/c^2$ was set (see figure 2.15).

The limit derived from data was compared with a Monte Carlo simulation, based on a background model assuming the presence of e^-/γ -background only [83], which gives the light-red band (1σ C.L.) in figure 2.15 [67]. Limit and simulation agree throughout the whole mass range indicating that the events in the acceptance region may solely be explained by leakage from the e^-/γ -band.

This result excludes the lower mass maximum (M2) from phase 1, but more statistics is required to improve the limit at higher masses and thereby to clarify the origin of the higher mass maximum (M1).

Low-Threshold Detectors

The importance of a low threshold was demonstrated with the result of the conventional detector module named Lise, which is the module with the lowest energy threshold operated in phase 2 [74]. With a threshold of 307 eV the sensitivity for light dark matter was significantly enhanced. In a data set with an exposure of $52.2 \text{ kg live days}$ dark matter masses down to $0.5 \text{ GeV}/c^2$ are explored (see figure 2.15), which is a novelty in the direct dark matter search field. The improvement compared to the TUM40 result is a consequence of an almost constant background level down to the low threshold. The lower the mass of the dark matter particle, the more relevant these improvements become. In contrast, the reduced sensitivity for higher masses is a result of a worse background level in the crystal and the poor performance of the light detector. With the

result of Lise CRESST demonstrated that detector performance is the key requirement to achieve sensitivity to dark matter particles of $\mathcal{O}(1 \text{ GeV}/c^2)$ and below.

In figure 2.15 it can also be observed that the CRESST exclusion limits rise more moderately towards lower dark matter masses than the limits from other experiments. This distinctive feature is a result of the ability to probe a possible dark matter signal on light nuclei (O and Ca) as well as on heavy W nuclei in addition to measure nuclear recoil energies with little systematic uncertainty down to a low energy threshold.

2.6.2 Future Strategy of CRESST-III

The results of phase 2 demonstrate that CRESST has the unique potential to explore the low-mass regime. As a consequence, the CRESST collaboration decided to optimize the detectors in order to gain even more sensitivity for low dark matter masses in future phases. A strategy that allows to explore the low-mass dark matter region further and to approach the neutrino floor was developed [84]. With the upgrade to CRESST-III, it is planned to explore the low-mass region down to the neutrino scattering limit.

In the first phase of CRESST-III⁸ ten small modules with a reduced threshold will collect data for one year. Depending on the threshold achieved, new parameter space down to a dark matter particle mass of $\sim 0.1 \text{ GeV}/c^2$ might be explored (see chapter 3). CRESST-III phase 1 started to take data in September 2016.

For future phases it is planned to reduce the background significantly, mainly by improving the crystal radiopurity. Additionally, an upgrade of the cryostat is planned in order to be able to measure 100 modules with reduced threshold and background. Further details on the expected time scales and the developments needed for each step can be found in [84].

⁸Within this work the different phases of CRESST are labeled according to [84].

Chapter 3

Sensitivity Projections for CRESST-III

As long as a direct dark matter search experiment does not observe a signal, only an upper limit on the dark matter particle-nucleon cross-section depending on the dark matter particle mass can be derived. Such a limit defines the best sensitivity on dark matter particles in different mass regions of the respective experiment. The statistical methods to derive an upper limit in the parameter space and the parameters determining the sensitivity in different regions of the parameter space have been reviewed e.g. in [85]. In the following only a brief overview is given.

In order to improve the sensitivity of an experiment it is necessary to know its restricting parameters. The sensitivity is mainly determined by three different parameters: The exposure (i.e. the product of detector mass and measurement time), the background observed in this exposure, and the threshold. For exploring different regions of the parameter space, these parameters play a role of different importance.

The sensitivity on the cross-section depends on the dark matter particle mass. It is maximal at the position of the minimum of the derived limit. This position is given by the kinematics of the scattering process, which depend on the target nucleus [85]. At low masses, the sensitivity is mainly limited due to the finite energy threshold of the detector, whereas at large masses the sensitivity is reduced due to a smaller expected event rate. As the local dark matter density is assumed to be a constant, a larger dark matter particle mass results in less particles available for scattering and, thus, a smaller rate.

In the present work the influence of the different parameters on the expected sensitivity of the CRESST experiment is investigated. With the knowledge of the parameters that determine the sensitivity it is possible to optimize the detectors. A similar study using the same methods has been performed in [84], where the expected sensitivity for CRESST-III is determined.

After explaining the method and the necessary assumptions used for the simulation in section 3.1, the different parameters and their impact on the sensitivity are discussed (section 3.2). An estimation of the potential of CRESST-III concludes this chapter in section 3.3.

3.1 Method and Assumptions

For each modification considered in the following, a projection based on the performance of TUM40 (the module with the best overall performance in CRESST-II phase 2 [67]), is simulated. The projections are calculated with a Monte Carlo simulation, with 1000 data sets simulated for each projection. The simulations are based on a background

model assuming the presence of e^-/γ -background only [83] and the distribution in the light yield - energy plane according to an empirical model of the e^-/γ -band¹ (see appendix B). From each data set the corresponding limit is calculated with Yellin's optimum interval method [86, 87]². The areas shown in the following figures correspond to the 1σ confidence level (1σ C.L.), i.e. for each mass the central 68 % of the respective limits lie in the colored area.

The projections are compared with the measured sensitivity of the module TUM40 in CRESST-II phase 2 (red solid line in the following figures) with an exposure of 29.35 kg days and a threshold of 603 eV [67]. The projection for TUM40 obtained in the present work (light red band in the following figures) is slightly different to the one published in [67]. The reason for this difference is, that for the present work the model is based on the complete data set of TUM40, while in [67] a model based only on a subset of the data was used. Due to the enhanced statistics slightly different parameters are found in both models and, thus, also the corresponding projections are slightly different. All projections shown in this chapter are calculated with the model, which is based on the full data set.

The simulations are based on the performance of TUM40 as measured in CRESST-II phase 2³. This includes especially the background and the non-proportionality of the light yield of the crystal⁴. In future phases most of the crystals used are planned to be grown at Technische Universität München (TUM). In particular the background and the non-proportionality parameters of TUM-grown crystals are expected to be similar [76, 77].

The low-energy e^-/γ -background observed in TUM40 was investigated in [83]. A background model was developed that describes the observed spectrum (see figure 3.1). An average of 3.51 ± 0.09 e^-/γ -events per kg keV day in the range of 1 – 40 keV is observed. In the simulations done within the present work the spectrum is extrapolated with a constant value down to the assumed energy threshold for energies lower than the threshold of TUM40. The non-proportionality of the crystal is parametrized within the fit of the e^-/γ -band model by the parameters L_2 and L_3 ¹.

During the analysis several cuts reduce the signal survival probability especially at low energies. In the module TUM40 the signal survival probability at low energies (see black solid line in figure 3.2) is mainly reduced due to a pulse-shape cut removing pulses which are taking place in the carrier [67]. For the simulations assuming an energy threshold lower than the one measured with TUM40 in [67], assumptions for the low energy range have to be made, as the signal survival probability directly influences the limit. Future detectors are planned to be operated without a carrier and, thus, a signal survival probability constant until energies close to threshold is expected. For simulations assuming a threshold lower than 603 eV, the signal survival probability is

¹The parameters used in the simulation done within the present work to describe the e^-/γ -band of TUM40 are the following: $L_0 = 0.978$, $L_1 = 0 \text{ keV}^{-1}$, $L_2 = 0.343$, $L_3 = 8.888 \text{ keV}$, $S_0 = 0.0667 \text{ keV}_{ee}^2$, $S_1 = 0.561 \text{ keV}_{ee}$, $S_2 = 0$. The parametrization of the recoil bands is explained in appendix B.

²The simulations as well as the calculations were done with a software provided by [88].

³Analyzed data provided by [88].

⁴At small energies, the e^-/γ -band usually decreases to lower light yields. This so-called non-proportionality effect is detector dependent and is observed in most inorganic scintillators at low energies [89, 90]. In the case of TUM40 strongly pronounced compared to commercial crystals[76].

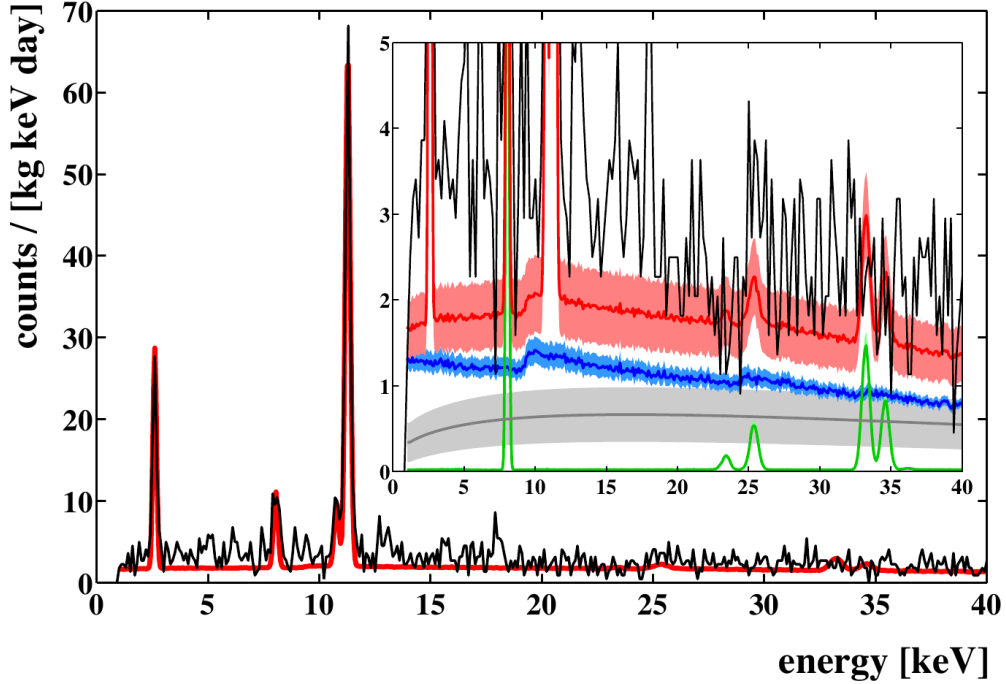


Figure 3.1: Histogram of the events in the region of interest recorded with TUM40 in CRESST-II phase 2 (black line). The red line indicates the sum of all background sources identified in [83] with the dominant peaks from cosmogenic activation (2.6 keV, 10.7 keV, and 11.3 keV) and the Cu X-ray line (8.0 keV). The insert shows the decomposition of the background based on Monte Carlo simulation developed in [83]. The contributions of external γ -radiation (green), external betas (grey), and intrinsic e^-/γ -radiation from natural decay chains (blue) are shown. The sum of these components (plus γ -peaks) is shown in red. The individual 1σ error bands are depicted in the corresponding color. An average of 3.51 ± 0.09 e^-/γ -events per kg keV day in the range of 1 – 40 keV is observed. The identified backgrounds explain $\sim 70\%$ of the observed events. Image taken from [83].

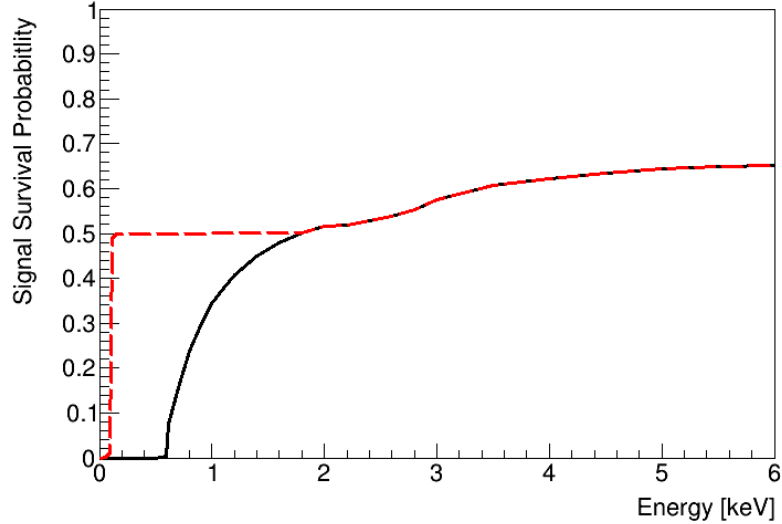


Figure 3.2: The signal survival probability of TUM40 after application of all selection criteria for a threshold of 603 eV from [88] is depicted as black solid line. The red-dashed line describes the signal survival probability assumed for the simulations of a threshold of 100 eV. For lower thresholds the cut off is shifted to the respective threshold.

extrapolated at a value of 50 % and cut off at the respective threshold. The assumed signal survival probability for a threshold of 100 eV is shown as red-dashed line in figure 3.2.

In the following figures the projections for the discussed improvements are compared to the projection for the performance of TUM40, which is depicted as light red band. Although, the model depends on assumptions the simulations give an indication which modifications influence the sensitivity most in the different regions of the parameter space. In conclusion, the effects on the sensitivity should be considered rather qualitatively than quantitatively.

3.2 Impact of Relevant Parameters

In the following the impact of the relevant parameters on the sensitivity of a direct dark matter experiment is investigated. In order to disentangle the influence of exposure, background, as well as threshold, these modifications are studied separately.

3.2.1 Exposure

As long as no background is observed, the sensitivity of a direct dark matter experiment scales with the exposure, i.e. the product of detector mass and measurement time. The exposure can be increased either with longer measurements or with an increased target mass. As it is not feasible to increase the measurement time arbitrarily, the exposure usually is increased with an enlarged detector mass. One possibility to do this is to increase the mass of each single detector, which is difficult to achieve without reducing the detector performance. Otherwise, the detector mass can be increased by operating

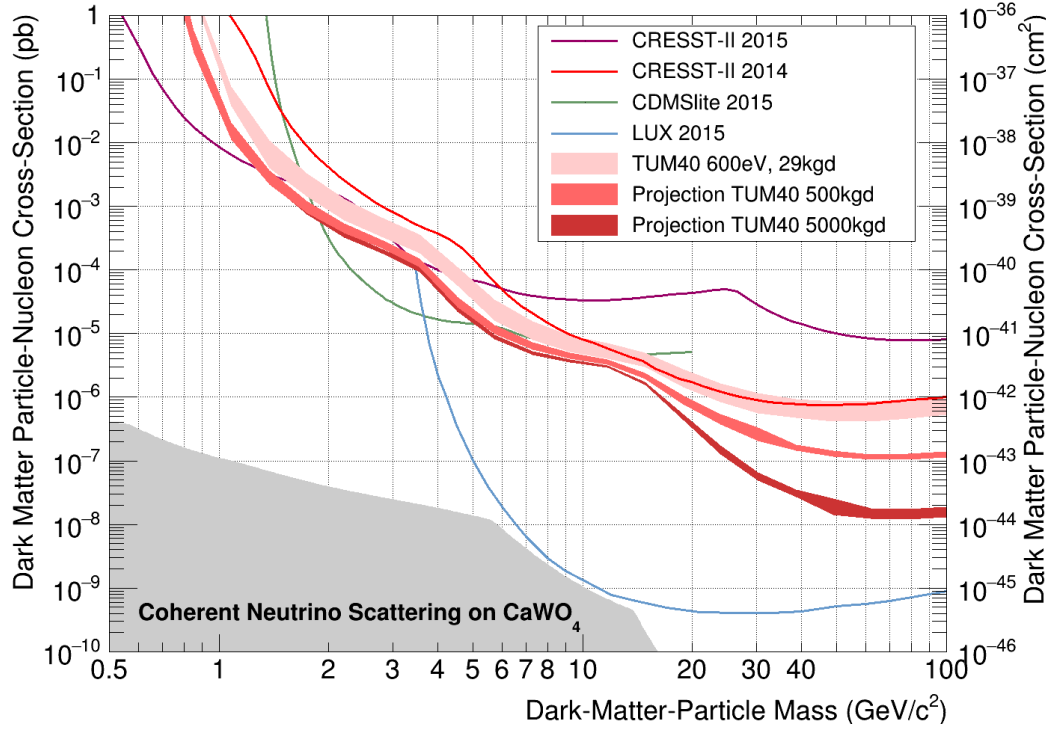


Figure 3.3: The expected sensitivities (1σ C.L.) for an exposure of 500 kg days (medium red) and 5 tonne days (dark red) with a TUM40 like module shown in the parameter space for elastic spin-independent dark matter nucleon scattering. A larger exposure results in an increased sensitivity in the high mass region while at low masses the exposure is not an important parameter for the sensitivity. For comparison the currently leading limits of different experiments (solid lines) and the neutrino floor for CaWO_4 (gray-shaded area) are shown [37, 45, 49, 67, 74].

a large number of detectors, which in the case of the CRESST experiment implies a large number of readout channels for which an upgrade of the setup would be necessary.

In figure 3.3 the sensitivity expected for an exposure of 500 kg days with the performance of the module TUM40 (medium red) demonstrates that increased statistics improve the limit for masses above $\sim 15 \text{ GeV}/c^2$ compared to the projection with an exposure of 29 kg days (light red). At a mass of $100 \text{ GeV}/c^2$ the limit can be increased by a factor of ~ 10 , while for masses $\lesssim 13 \text{ GeV}/c^2$ the improvement is less than $\sim 20\%$. A projection for an exposure of 5 tonne days (dark red) illustrates that in the high mass region the sensitivity directly scales with exposure, as this projection with a ten times higher exposure improves the limit by a factor of ten at a mass of $100 \text{ GeV}/c^2$. However, for masses $\lesssim 13 \text{ GeV}/c^2$ there is hardly any improvement in the sensitivity compared to the sensitivity expected with an exposure of 500 kg days.

In conclusion, in the high mass region the sensitivity directly scales with exposure while at low masses exposure is not an important parameter.

3.2.2 Background

Another parameter that limits the sensitivity is the observed background. As explained before (see section 2.6), the limits derived from data of TUM40 and Lise both agree with the presence of e^-/γ -background only, throughout the whole mass range. This indicates that the events in the acceptance region are probably produced by this background only. Therefore, reducing the background means reducing the leakage of the e^-/γ -band, which can be achieved by *reducing the content of the band* or/and *reducing the overlap of the bands*.

- A reduction of the e^-/γ -band content can be achieved by *increasing the radiopurity of the crystals* (selection and/or cleaning of the raw materials, multiple growing of the crystals [77, 83]) or by *reducing the background from the surrounding of the detectors* (e.g. selection and improved cleaning of materials, active veto).
- The overlap of the bands can be reduced by a *reduction of the width of the bands*, which is equivalent to an *enhancement of the light detector resolution* (e.g. increase of the amount of the detected light or an increase of the sensitivity of the light detector) or a *reduction of the non-proportionality of the light yield*.

As the e^-/γ -background is dominated by the intrinsic contamination of the crystals [83], a reduction of the overall background can be achieved with an improvement of the crystal radiopurity. An investigation of the crystal growth process and a development of a cleaning procedure of the raw materials is currently in progress [91]. Within the next years a reduction of the internal impurities of the crystals by a factor of 100 is in reach [84].

The expected sensitivities for a reduction of the total background by a factor of 10 (light magenta) and 100 (dark magenta) are shown in figure 3.4. As can be seen, a reduction of the background improves the sensitivity over the whole mass range. For an improvement of the background by a factor of 10 a gain of sensitivity by a factor of 2–3 is expected for masses of 2–100 GeV/c^2 . In the mass range where the improvement is more pronounced (10–20 GeV/c^2) the current sensitivity is more limited by backgrounds than in regions where a smaller improvement is expected. Only for masses below $\sim 2 \text{ GeV}/c^2$ the gain in sensitivity is only $\sim 10\%$. However, a further improvement of the background by a factor of 10, i.e. a factor of 100 in total, only results in a slight gain of the expected sensitivity. The maximum gain in sensitivity is ~ 2 for a mass of $\sim 13 \text{ GeV}/c^2$, while at masses $\lesssim 4 \text{ GeV}/c^2$ and $\gtrsim 40 \text{ GeV}/c^2$ an improvement of $\lesssim 20\%$ is expected. This is due to the fact that the expected amount of background events in the assumed exposure is close to zero.

In conclusion, for the given exposure of 29 kg days a reduction of the background by a factor of 10 improves the sensitivity for almost the complete mass range shown here, while a further reduction has only little effect. However, a background reduction pays out more when the exposure is increased significantly.

3.2.3 Threshold

The performance of the phonon detector is defined by its signal-to-noise ratio. A larger signal-to-noise ratio improves the energy resolution and accordingly reduces the energy

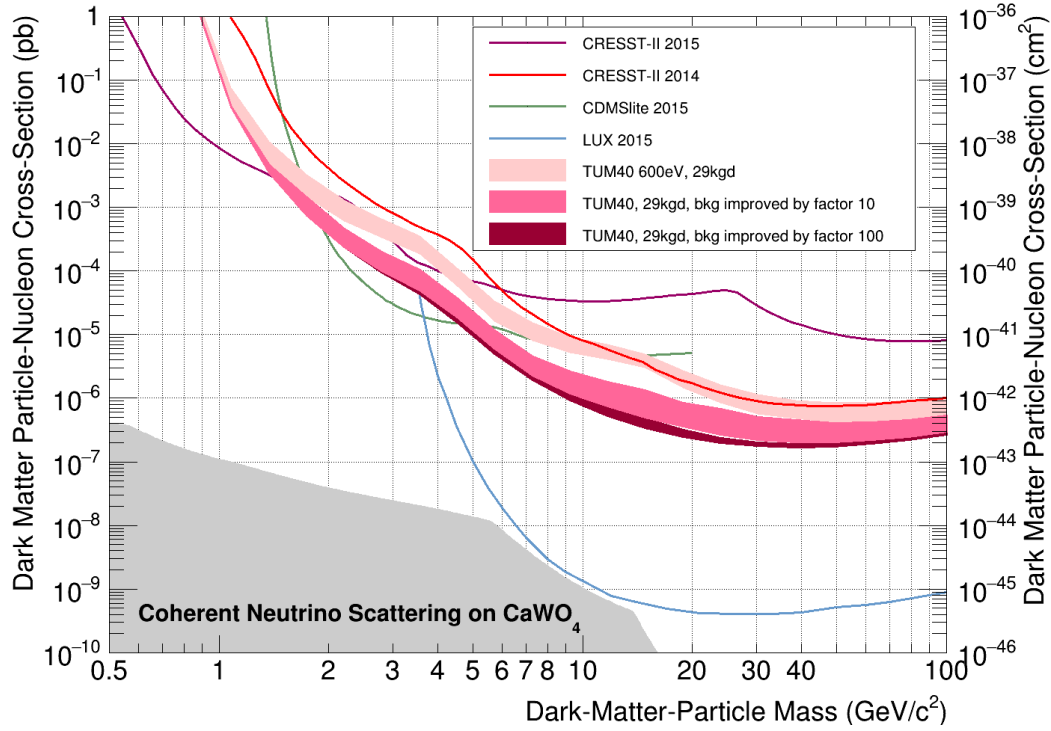


Figure 3.4: The expected sensitivities (1σ C.L.) for a module with a background reduced by a factor of 10 (light magenta) and 100 (dark magenta) compared to TUM40 shown in the parameter space for elastic spin-independent dark matter nucleon scattering. All projections are simulated for an exposure of 29 kg days in order to compare them to the projection for TUM40. Compared to the current sensitivity obtained with the given background a slight improvement of the sensitivity over the whole mass range is expected. However, improving the background by a factor of 100 only results in a marginal sensitivity increase due to the low number of expected background events in the exposure of 29 kg days. For comparison the currently leading limits of different experiments (solid lines) and the neutrino floor for CaWO_4 (gray-shaded area) are shown [37, 45, 49, 67, 74].

threshold. The lowest energy threshold achieved with CRESST detectors in phase 2 was 307 eV [74]. A further reduction can be achieved by either increasing the signal or by reducing the noise of the detector. While the noise is dominated by the parameters of the TES and the SQUID (see section 4.3) and is difficult to reduce, an increase of the signal can be achieved by reducing the size of the target crystal or a further optimization of the TES.

From the detector physics (see chapter 4) it is expected that a reduction of the crystal volume by a factor of 10 combined with an optimization of the detector layout translates in a reduction of threshold from the 603 eV reached in TUM40 [67] to at least 100 eV (see section 5.1). First measurements indicate that with the optimized detector module even lower thresholds down to ~ 20 eV can be reached (see section 7.2.2).

Figure 3.5 illustrates the sensitivities that can be reached with a threshold of 20 eV (light yellow), 50 eV (medium yellow), and 100 eV (dark yellow) with all parameters concerning the light detector performance and backgrounds as observed in the TUM40 module. It can be seen that for masses below $\sim 3 \text{ GeV}/c^2$ the sensitivity increases with a lower threshold, whereas in the high-mass region almost no difference is visible. With thresholds of 100 eV and 20 eV the parameter space down to masses of $\sim 0.25 \text{ GeV}/c^2$ and $\sim 0.13 \text{ GeV}/c^2$ can be explored, respectively. For a dark matter particle mass of $1 \text{ GeV}/c^2$ a threshold of 100 eV enhances the sensitivity by three orders of magnitude and for a threshold of 20 eV the sensitivity is improved by more than four orders of magnitude.

In conclusion, a reduction of threshold enhances the sensitivity in the low mass region drastically and allows to explore lower dark matter particle masses. For the high-mass region this parameter is not decisive.

3.3 Future Potential of CRESST-III

The projections shown in this chapter demonstrate that for the sensitivity in the low-mass region of the parameter space a reduction of the energy threshold is the crucial modification, while a reduction of background and an increase of exposure help to improve the limit further in the high-mass region. In order to explore new parameter space, the future strategy of CRESST-III is to operate detector modules with a threshold reduced to at least 100 eV in phase 1 [84]. Within the present work the new detector module for phase 1 with a reduced threshold is developed in order to gain sensitivity for low-mass dark matter particles.

In addition to the reduction of the threshold of the phonon detector smaller crystals are expected to be beneficial for the light detector performance. Due to the size reduction of the crystal more light is expected to escape the crystal which may result in an increase of the detected light by a factor of 3 [84]. Moreover, also the size of the light detector can be adjusted to the crystal geometry, which corresponds to a reduction of the volume by a factor of 3. The latter is conservatively expected to translate in a reduction of light detector noise by a factor of 2 [84].

Ten of such small modules are operated in CRESST-III phase 1 which started to take data in September 2016. It is expected, that within one year an exposure of 50 kg days can be collected. The sensitivity expected for this exposure obtained with small

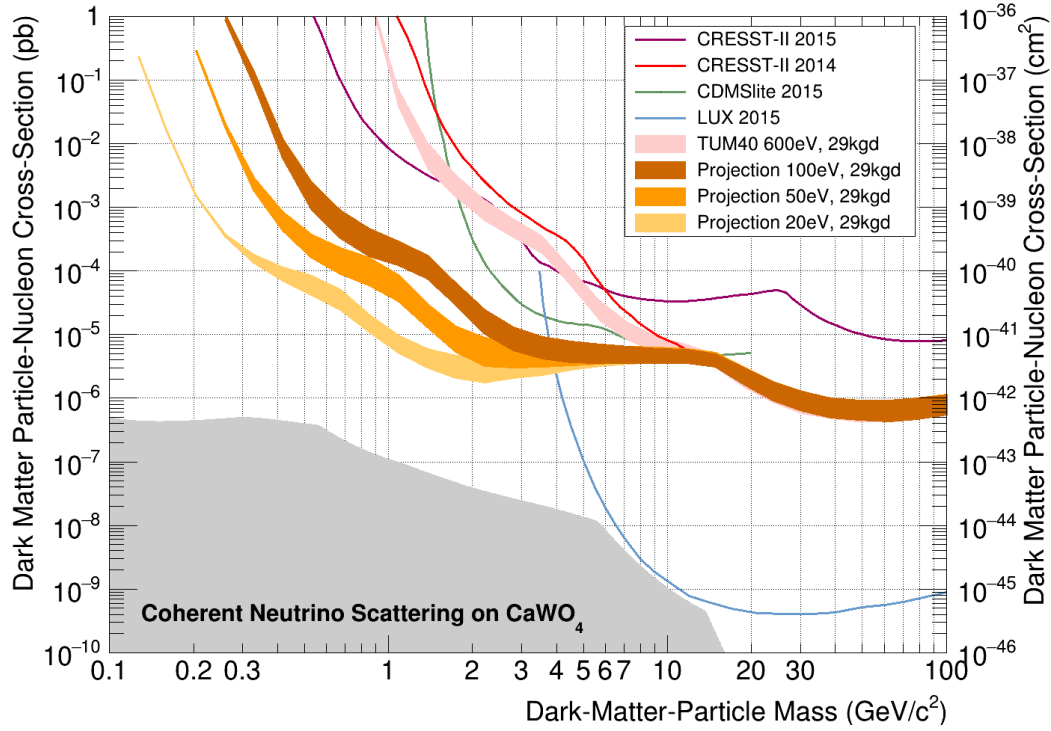


Figure 3.5: The expected sensitivities (1σ C.L.) for a module with a reduced threshold of 100 eV (dark yellow), 50 eV (medium yellow), and 20 eV (light yellow) shown in the parameter space for elastic spin-independent dark matter nucleon scattering. All other parameters (concerning e.g. light detector performance and background) are equal to the ones of TUM40. All projections are simulated for an exposure of 29 kg days in order to compare them to the projection for TUM40. A lower energy threshold results in the low dark matter mass region in an improved sensitivity while at high dark matter masses no sensitivity enhancement is expected. For comparison the currently leading limits of different experiments (solid lines) and the neutrino floor for CaWO_4 (gray-shaded area) are shown [37, 45, 49, 67, 74]. Note that the scale of the x-axis is different (extended down to dark matter particle masses of 0.1 GeV/c² compared to 0.5 GeV/c² before) compared to the plots shown previously.

modules is depicted in figure 3.6 for a threshold of 100 eV (dark orange) and a threshold of 20 eV (light orange). The measurements with a prototype module, discussed in chapter 7, indicate that a threshold of 20 eV is possible to achieve with the optimized detector module developed in the present work. Due to the reduced threshold new parameter space in the low-mass region can be explored. The improvement of the expected sensitivity in the low mass region is mainly caused by the decreased threshold, since the sensitivities are similar to the expected sensitivity shown in figure 3.5 where only the threshold is reduced. As expected, both projections only differ in the low-mass region, where the threshold dominates the sensitivity. The additional improvements of the light detector performance and the increased exposure enhance the sensitivity mainly in the mass region of $\gtrsim 5 \text{ GeV}/c^2$. With a small module having a threshold of 20 eV masses down to $\sim 0.13 \text{ GeV}/c^2$ might be explored with CRESST-III phase 1. For a dark matter particle mass of $1 \text{ GeV}/c^2$ the sensitivity is increased by more than four orders of magnitude.

For a further gain in sensitivity in CRESST-III phase 2 it is necessary to reduce the background. As already mentioned, it is planned to decrease the internal background of the crystals by a factor of 100 [84]. Additionally, the number of readout channels is planned to be increased, so that in total 100 of the small modules can be operated. In this case it is foreseen to collect an exposure of 1000 kg days within two years of measurement time [84]. The expected sensitivity for this phase is illustrated in figure 3.6 as the two lowest projections for a threshold of 100 eV (red) and 20 eV (light red). Compared to the sensitivity expected for CRESST-III phase 1 the sensitivity can be increased in the whole mass region by at least one order of magnitude due to the increase of exposure and the reduction of background. Compared to the current sensitivity CRESST-III phase 2 is expected to improve by six orders of magnitude for a dark matter particle mass of $1 \text{ GeV}/c^2$. The expected sensitivities shown here are in good agreement to former projections [84].

To summarize, depending on the threshold of the small modules, CRESST-III will be able to explore the parameter space of dark matter down to masses of $\sim 0.1 \text{ GeV}/c^2$. Furthermore, with these detector modules and a large enough exposure the detection of coherent neutrino nucleus scattering might be in reach. In the remaining part of the present work the module foreseen for CRESST-III is discussed in detail.

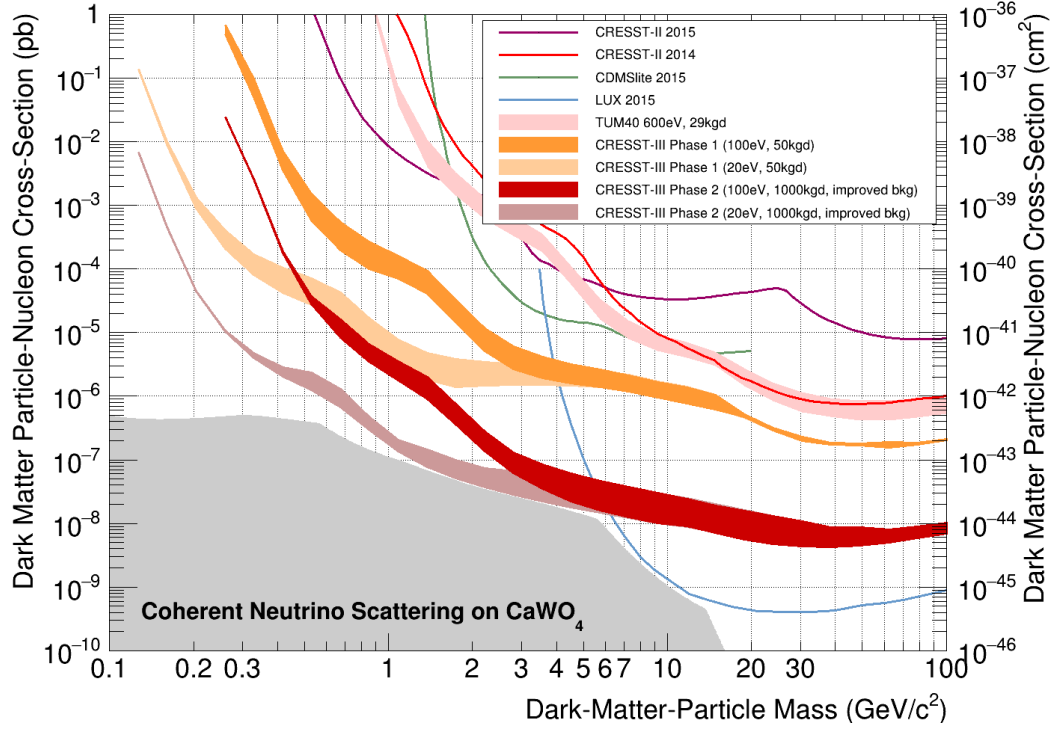


Figure 3.6: The expected sensitivities (1σ C.L.) for CRESST-III phase 1 (orange) and phase 2 (red) shown in the parameter space for elastic spin-independent dark matter nucleon scattering. CRESST-III will operate small detector modules with a reduced threshold of at least 100 eV (dark colors) or even down to 20 eV (light colors). In the first phase an exposure of 50 kg days is aimed to be collected within one year. In this phase new parameter space in the low mass region can be explored, while the sensitivity for higher masses is only slightly increased. In the second phase the aim is to reduce the e^-/γ -background by a factor of 100 and, additionally, to increase the number of operated detector modules to 100 in order to achieve an exposure of 1000 kg days within two years. These improvements are expected to result in an increase of the sensitivity in the whole mass range. For comparison the currently leading limits of different experiments (solid lines) and the neutrino floor for CaWO_4 (gray-shaded area) are shown [37, 45, 49, 67, 74].

Chapter 4

Detector Model

In order to be able to optimize the detector performance a detailed understanding of the detector physics is required. The process that leads from an energy deposition to a thermal signal in the thermometer can be described within a thermal detector model, which is summarized in the present chapter. In order to model the detector behavior, the geometry of the detectors and especially that of the thermometers needs to be known (see section 4.1). The thermal model that describes the processes after an energy deposition which finally leads to the formation of the measurable signal is discussed in section 4.2. The detector is also affected by various noise sources (see section 4.3). The noise contribution measured in the different setups is investigated in section 4.4. For the determination of the detector performance the decisive parameter is the signal-to-noise ratio. Therefore, in section 4.5 it is discussed how signal and noise determine the sensitivity of a detector.

4.1 Components of the Detector Module

As mentioned in the previous chapter, a CRESST detector consists of a dielectric absorber (CaWO_4 , sapphire or silicon) and a superconducting thin tungsten film. The latter is evaporated on the absorber and serves as a sensitive thermometer. An energy deposition in the absorber material is transformed into phonons which then can be transferred into the thermometer.

As the goal of the present work is to optimize the performance of the detectors, they are described in detail in the following.

4.1.1 Phonon Detector

In CRESST-II the absorber of the phonon detector typically is a scintillating CaWO_4 single crystal. As explained before there exist different detector module designs (see section 2.6). In the conventional module the crystal is of cylindrical shape with a diameter and a height of ~ 40 mm which corresponds to a mass of ~ 300 g.

Two of the alternative detector designs mounted in CRESST-II phase 2 feature smaller crystals, in order to obtain the same outer dimensions of the module as the standard conventional design, which allows a proper mounting in the fixed geometry of the carousel. The cylindrical crystals of the modules with a silicon beaker as light detector have a mass of ~ 195 g. For the module with the crystal held by CaWO_4 sticks a cuboidal crystal has been used, as this shape is expected to have a higher light output [69, 80]. In order to fit into a standard module housing those crystals have to

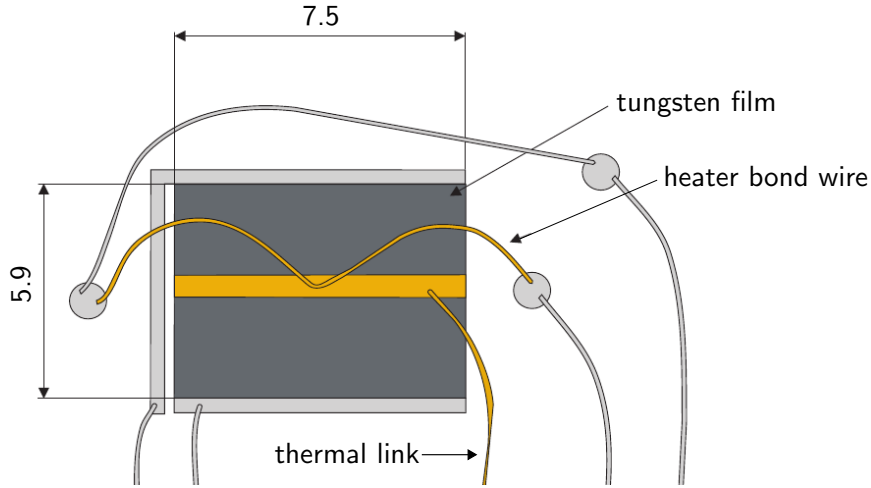


Figure 4.1: Structure of the phonon detector TES used in CRESST-II phase 2. The tungsten film (dark gray) has a size of $7.5 \times 5.9 \text{ mm}^2$. The aluminum film (light gray) is used to contact the thermometer with bond wires. The bias supply wires provide a constant current for the thermometer. The thermal link is realized by a gold bond wire and couples the thermometer to the heat bath. The heater is used to stabilize the thermometer in its transition and to send heater pulses. All measures are given in millimeters. Image taken from [92].

be slightly smaller with a size of $40 \times 32 \times 32 \text{ mm}^3$ corresponding to a mass of 249 g [81].

During the evaporation of the tungsten film for the thermometer, which happens at a temperature of $\sim 450 \text{ }^\circ\text{C}$ and a low pressure of 10^{-8} mbar , the oxygen content of the crystal is reduced which results in a reduction of its scintillation efficiency [59]. Therefore, most of the detectors are produced as composite detectors, where the thermometer is produced on a small carrier substrate (with a size of $20 \times 10 \times 1 \text{ mm}^3$) which is then glued with a thin layer of epoxy resin to the big absorber crystal [57].

While the absorber crystals of the different module designs are slightly different, all phonon detector TES operated in CRESST-II phase 2 have the same size and design depicted in figure 4.1. The tungsten film (dark gray), which is evaporated either directly on the crystal or on a small carrier substrate, has a size of $5.9 \times 7.5 \text{ mm}^2$ and a thickness of 200 nm. On each of the two long sides an aluminum stripe (light gray), which is used to connect the thermometer via bond wires, is placed. The thermal coupling to the heat bath is realized with a gold bond wire of $25 \text{ }\mu\text{m}$ diameter, connected to the gold stripe (yellow) in the middle of the thermometer. The heater is realized by a gold bond wire, which is attached to the gold stripe in the middle of the thermometer. With a heater current controlled by a PID controller, the thermometer is kept in a certain point in its transition (see section 2.4).

4.1.2 Light Detector

In the majority of all modules operated in CRESST-II phase 2, the light absorber consists of an SOS (silicon-on-sapphire) wafer, which is a sapphire disk of 40 mm diameter

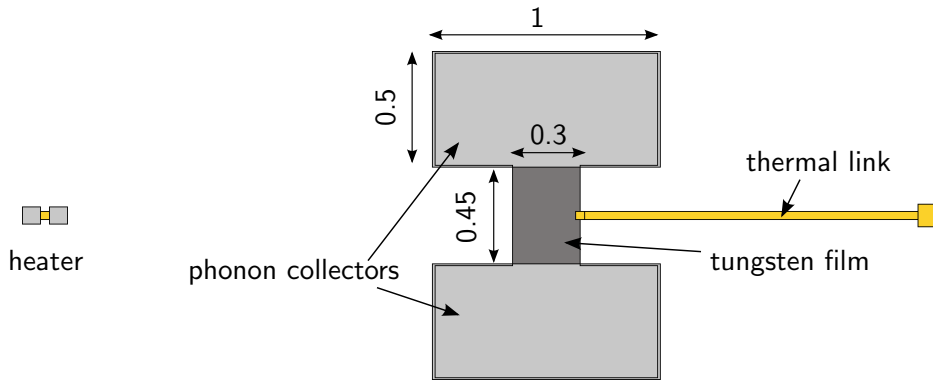


Figure 4.2: Structure of the light detector TES as used in CRESST-II phase 2. The tungsten film (dark gray) has a size of $0.45 \times 0.3 \text{ mm}^2$. It features phonon collectors made of an aluminum film (light gray), which are also the contact pads for the bias supply wires. The thermal link consists of a thin gold film (yellow) and couples the thermometer weakly to the heat bath. The heater (left) is electrically separated from the thermometer film. It consists of a thin gold film with two aluminum contact pads. All measures are given in millimeters.

and of 0.46 mm thickness with a $1 \mu\text{m}$ epitaxially grown silicon layer on one side¹.

The TES of the light detector covers a smaller area than the phonon detector TES. In figure 4.2 the typical structure of the light detector TES is depicted. The actual thermometer film has a size of $0.45 \times 0.3 \text{ mm}^2$ (dark gray). To increase the amount of phonons absorbed by the thermometer it uses phonon collectors made of an aluminum film (light gray, see section 4.2.7). The thermal coupling is provided by a thin gold film (yellow) and couples the TES thermally to the heat bath of the cryostat. The heater is electrically and physically separated and consists of a small gold film with two aluminum bond pads. An electrically separated heater is advantageous as it reduces the observed noise [66]. Although, this heater is not electrically connected to the tungsten film, it works similar to the phonon detector heater, i.e. it allows to inject non-thermal phonons into the heater [66].

4.2 Thermal Model of the Detector

As described in section 2.2, CRESST detectors are cryogenic calorimeters, that measure the energy deposited in a dielectric absorber by detecting its temperature rise with a sensitive thermometer. The phonons can be transferred into the thermometer, whose temperature is measured via its resistance change. By a weak thermal coupling to a heat bath the temperature of the thermometer relaxes back to equilibrium. In order to model the formation of the measured temperature pulses, a detailed description of a theoretical model for the signal evolution in a low temperature calorimeter used in CRESST has been developed in [93].

The current section reviews of the parameters and processes after an energy deposition in the absorber. In this thermal model the absorber and the thermometer are both

¹One alternative module design uses a silicon beaker as light absorber. This type of light detector also uses a different design for the TES, which however, is not discussed here.

	CaWO ₄	Al ₂ O ₃	Si
Θ_D [K]	228	1041	648
$\nu_D = k_B \Theta_D / h$ [THz]	4.8	21.7	13.5

Table 4.1: Debye temperatures Θ_D and Debye frequencies ν_D for materials used as absorber in CRESST [93, 94].

characterized by their individual temperatures T and heat capacities C . The different systems are thermally coupled to each other by the thermal couplings G , which define the phonon transport through the components.

4.2.1 Heat Capacities

The heat capacity is a fundamental property of a material, as it determines the temperature rise that can be achieved by an energy deposition. The relation of an amount of heat energy Q transferred to an object and the resulting temperature change ΔT is described by the heat capacity C :

$$C = \frac{Q}{\Delta T}. \quad (4.1)$$

The heat capacity results from the different possible excited states of a thermodynamic system in a certain temperature range.

Non-Metals

The heat capacity of *crystalline dielectric materials* is dominated by the lattice specific heat. For temperatures much smaller than the Debye temperature Θ_D the specific heat c_{ph} can be described by the Debye model [56]:

$$c_{ph}(T) = \frac{12}{5} \pi^4 n_a k_B \left(\frac{T}{\Theta_D} \right)^3 =: A T^3 \quad (4.2)$$

where n_a is the number of lattice atoms per mole, k_B the Boltzman constant and A a material constant. The Debye temperatures for the absorber materials used in CRESST are listed in table 4.1. In semiconductors the conducting electrons are frozen out at low temperatures and, thus, this relation is also valid. Dielectrics and semiconductors are a suitable absorber material for cryogenic calorimeters as due to the T^3 dependence, the phonon heat capacity is very small at low temperatures.

Metals

In *metals* not only the phonon system but also the electron system can be thermally excited and, therefore, contributes to the heat capacity. For temperatures much smaller than the Fermi temperature T_F , the specific heat of the electron system c_e is given by [56]

$$c_e(T) = \frac{\pi^2}{2} n_e k_B \frac{T}{T_F} =: \gamma T \quad (4.3)$$

		Tungsten	Gold	Aluminum
T_C	[mK]	15	-	1180
T_F	[K]	27000	63900	134900
Θ_D	[K]	383	165	428
γ	[mJ · mol ⁻¹ · K ⁻²]	1.008	0.729	1.35

Table 4.2: Transition temperatures T_C , Fermi temperatures T_F , Debye temperatures Θ_D , and Sommerfeld constants γ for metals utilized CRESST thermometers [95, 96].

with the number of conducting electrons per mol n_e and the Sommerfeld parameter γ which is a material constant. Thus, the total specific heat of a metal is:

$$c = c_{ph} + c_e = AT^3 + \gamma T. \quad (4.4)$$

At temperatures below 1 K the phonon heat capacity is negligible and the electronic heat capacity dominates due to its linear dependence on the temperature. The relevant material parameters for the metals used in the CRESST thermometers are given in table 4.2.

Superconducting Metals

In a *superconducting metal* the heat capacity changes at its critical temperature T_C , where the former goes into its superconducting state. In the absence of a magnetic field the transition is a second-order phase transition and results in a jump of the heat capacity. Simple superconductors, such as aluminum and tungsten, follow the BCS theory of superconduction, which predicts the jump to be [97]

$$\Delta c = 1.43 \gamma T_C \quad (4.5)$$

with the electronic specific heat in the normal conducting state γT_C . At temperatures below T_C the heat capacity of a superconductor decreases exponentially with temperature, falling off much more rapidly than the electronic heat capacity c_e . Below $T_C/2$ the heat capacity of the superconducting metal becomes negligible compared to the remaining phonon contribution.

In practice a finite width of the transition is observed (see figure 2.3), which is caused by small position dependencies of the transition temperature due to inhomogenities in the thermometer film [98]. These inhomogenities can lead to a resistance measurement of zero, while parts of the thermometer are still normal conducting. For this reason there is no linear relation of the heat capacity of the thermometer film and its resistance within the superconducting transition.

4.2.2 Non-thermal and Thermal Phonons

An energy deposition in the absorber creates high-frequency (O(THz)) *non-thermal phonons*, with energies of a few meV. They are called non-thermal as the thermal energies at temperatures of the detector operation (~ 10 mK) are much smaller ($E =$

$k_B T \approx 1 \mu\text{eV}$). The initial phonon spectrum depends on the type of interaction. If the deposited energy is transferred to an electron, this electron loses the energy in the absorber via emission of optical phonons, which finally decay into acoustical phonons of about half the Debye frequency (see table 4.1) on a time scale of 100 ps. This leads to an almost monoenergetic frequency distribution for electron recoils. In the case of a nuclear interaction, energy is deposited via the local deformation of the crystal lattice and non-thermal acoustic phonons in a broad frequency range are excited.

In both cases, these phonon populations are not stable and decay to a thermal distribution with a decay rate, which strongly depends on the phonon frequency ν [93]:

$$\Gamma_{decay} \propto \nu^5. \quad (4.6)$$

Due to this strong frequency dependence of the decay rate, the phonon population decays very fast to a distribution with a mean frequency of a few GHz [93]. After this very rapid initial decay differences in the frequency distribution caused by different interaction types are washed out. The following decay has a much smaller rate of change and the mean phonon frequency stays nearly constant on the time scale of the response time of the thermometer.

During this time the non-thermal phonons spread ballistically over the whole volume of the absorber. They are distributed homogeneously in the absorber $\sim 20 \mu\text{s}$ after the interaction².

The temperature of the electron system in the thermometer defines the resistance of the thermometer and, thereby, the signal height. There exist two possibilities for the energy transfer into the thermometer:

- The non-thermal phonons can be absorbed directly in the thermometer film. Non-thermal phonons, that are transmitted into the thermometer film, transfer their energy directly to a free electron of the metal film and thereby heat the electron system.
- Part of the non-thermal phonons thermalizes in the crystal which happens mainly due to inelastic surface reflections. The resulting *thermal phonons* increase the temperature of the absorber. The thermalized phonons define the absorber temperature and can be transmitted into the phonon system of the metal film, which is weakly coupled to its electron system.

For the measured signal it is of importance which amount of energy is transported into the thermometer. These processes depend on the thermal couplings, which are discussed in the following.

4.2.3 Thermal Couplings

An energy deposition in the absorber is followed by relaxation processes which result in different temperatures of the sub-systems of the calorimeter. These temperature differences lead to a heat flow between the sub-systems until equilibrium is reached once again. For an understanding of the signal it is necessary to understand the thermal couplings between the different sub-systems of the calorimeter.

²A time of order L/v (with the largest crystal dimension L and the sound velocity v) is required to establish a uniform distribution of phonons in the absorber.

Phonon Transmission

As explained before, phonons are distributed over the whole absorber crystal shortly after an interaction. When hitting the absorber-thermometer interface, phonons can be either transmitted into the thermometer or reflected back into the absorber. The transmission probability of acoustic phonons across the absorber-thermometer interface can be calculated within the theory of anisotropic elastic continua.

In [93] a calculation of the energy flux per unit area and unit time across the boundary from material 1 to material 2 $\dot{Q}_{1 \rightarrow 2}$ was performed by summing over all modes and wave vectors of incident phonons. This energy flux is given by:

$$\dot{Q}_{1 \rightarrow 2} = \left\langle \frac{E}{V} \right\rangle \frac{1}{2} \langle v_{\perp} \alpha \rangle \quad (4.7)$$

where $\langle E/V \rangle$ is the average energy density of the phonons in the absorber, v_{\perp} is the phonon group velocity perpendicular to the interface, and α is the transmission probability. Hence, $\langle v_{\perp} \alpha \rangle$ describes the transmission of the incident phonons over the interface averaged over modes and angles of incidence. As non-thermal and thermal phonons feature the same angular distribution of wave vectors, the transmission through an ideal boundary does not depend on the frequency. Therefore, this equation can be used to describe the energy transmission of both by inserting the appropriate energy density $\langle E/V \rangle$.

Kapitza Conductance

With the energy density $\langle E/V \rangle$ of the thermal phonons, the heat boundary conductance G_K of thermal phonons, called *Kapitza conductance*, can be derived using equation 4.7 [93]:

$$G_K = \frac{1}{\Delta T} \left(\dot{Q}_{1 \rightarrow 2}(T + \Delta T) - \dot{Q}_{2 \rightarrow 1}(T) \right) = \frac{C}{2V} \langle v_{\perp} \alpha \rangle, \quad (4.8)$$

where C/V is the heat capacity per unit volume of material 1. In the case of phonon transmission from absorber to thermometer, the heat capacity of the dielectric absorber has a cubic temperature dependence (see equation 4.2). Hence, the Kapitza coupling for the absorber-thermometer interface exhibits the same dependence:

$$G_K \propto T^3. \quad (4.9)$$

The transmission coefficients for the materials relevant for the CRESST detectors calculated by numerical methods [93] are listed in table 4.3. Anisotropic conditions are assumed and the tungsten films are considered as polycrystalline metals with randomly oriented single crystals.

Electron-Phonon Coupling

During detector operation the thermometer film is stabilized in the superconducting transition, where only few electrons are bound in Cooper pairs. For this reason, phonons basically interact with the remaining free electrons. While the phonon transmission into the metal film does not depend on the frequency, the absorption of phonons in

Transmission from \rightarrow to	G_K/T^3 [kW · K ⁻⁴ · m ⁻²]	$\langle v_{\perp\alpha} \rangle$ [m/s]	$\bar{\eta}$
Si \rightarrow W	0.440	1485.4	0.246
Al ₂ O ₃ \rightarrow W	0.430	2547.5	0.290
CaWO ₄ \rightarrow W	1.784	647.9	0.142
Al ₂ O ₃ \rightarrow Si	0.495	2933	
Si \rightarrow Al ₂ O ₃	0.495	1668.7	

Table 4.3: Kapitza conductance G_K per T^3 , the transmission of the incident phonons over the interface averaged over modes and angles of incidence $\langle v_{\perp\alpha} \rangle$, and effective absorption $\bar{\eta}$ listed for different absorber-thermometer interfaces of CRESST detectors. Parameters are calculated for the transmission of phonons across the (001) plane of silicon, the (1 $\bar{1}$ 02) plane of sapphire, and the (001) plane of CaWO₄. Tungsten is considered to be polycrystalline with the crystals randomly oriented [93]. Values taken from [92].

the film does. Therefore, the electron-phonon coupling G_{ep} in the thermometer has to be considered separately for the thermal and the non-thermal phonons. This coupling depends on the mean free path of the phonons l_p , which can be described by the product $l_p = q \cdot l_e$. Thereby q is the phonon wave vector and l_e is the mean free path of the electrons. The latter is dominated by scattering on crystal defects and impurities and, therefore, is independent of the temperature. Thus, the temperature dependence of the mean free path of phonons l_p is only given by the phonon wave vector q .

Thermal Phonons For thermal phonons at low temperatures, where $q \cdot l_e \ll 1$ applies, it can be shown that the temperature of the electron-phonon coupling G_{ep} can be expressed as³ [99, 100] :

$$G_{ep} \propto T^5. \quad (4.10)$$

This strong temperature dependence leads to a thermal decoupling of the electron system in the thermometer from the phonon system in the thermometer and, thus, the absorber. Therefore, the thermal signal is strongly suppressed. As the mean free path length of the thermal phonons is much larger than the thermometer thickness, for the absorption of the thermal phonons the thermometer volume and not the thickness is relevant.

Non-thermal Phonons For non-thermal phonons $q \cdot l_e \gg 1$ applies and the mean free path of longitudinal and transverse phonons is given in the Pippard model [101]. Longitudinal phonons interact strongly with the electrons and are efficiently absorbed in the tungsten films (thickness of 200 nm), whereas transverse phonons do hardly interact. Assuming, for non-thermal phonons, that longitudinal phonons are completely absorbed and transverse phonons do not interact, the *average absorption probability* $\bar{\eta}$ can be calculated [93]. Values for $\bar{\eta}$ for the materials used in the CRESST detectors are listed in table 4.3.

³This relation is weakened at higher temperatures and, furthermore, by the metal film being in the superconducting transition. However, at the operating temperature of CRESST (~ 15 mK) the relation in equation 4.10 is usually assumed [93].

Due to the strong interaction among electrons the phonon energy is quickly thermalized and distributed in the electron system of the thermometer, whereby the temperature of the electron system is increased.

The before-mentioned decoupling of electrons and thermal phonons ($G_{ep} \propto T^5$) can lead to a significant overheating of the electron system in the thermometer with respect to the absorber. Therefore, the detector sensitivity is determined by the heat capacity of the thermometer film and not by the heat capacity of the absorber. The absorber influences the detector sensitivity rather by its phonon transport properties.

Thermal Coupling to the Heat Bath

The thermal coupling of the thermometer to the heat bath G_{eb} is realized via a structure of a normal conducting metal, which is either a gold bond wire or a structure of a thin gold film on the substrate. It is dominated by an electron-electron coupling. The coupling strength defines the thermal relaxation time of the thermometer $\tau = C_e/G_{eb}$, where C_e is the heat capacity of the electron system of the thermometer. The heat conductance G_{eb} of the structure follows the Wiedemann-Franz law [56]:

$$G_{eb} = \frac{LT}{R}, \quad (4.11)$$

with the residual resistance R of the gold structure at temperatures T and the Lorenz number $L = 2.45 \cdot 10^{-8} \text{ W } \Omega \text{ K}^{-2}$ [56]. This coupling can be varied over a wide range by adopting the resistance of the gold structure via its geometry.

The absorber is thermally coupled to the heat bath via the coupling G_{ab} , which has two components. On the one hand, there is a thermal coupling due to the mechanical mounting structures, i.e. the clamps holding the crystal. On the other hand, phonons can be transmitted directly to the gold structures and escape into the heat bath. The coupling between absorber and heat bath is expected to have a temperature dependence of $G_{ab} \sim T^3$ [93].

4.2.4 Model Assumptions

With the processes described up to now, a model for the signal formation in cryogenic calorimeters has been developed and is described in detail in [93]. In this model the detector is considered to consist of three different subsystems: The phonon system of the absorber, and the phonon as well as the electron system of the thermometer. All systems are thermally coupled to each other and the heat bath and are characterized by their respective temperature and heat capacity. All components of the thermal model are schematically shown in figure 4.3.

The absorber is characterized by its temperature T_a and its phonon heat capacity C_a . The phonon system of the thermometer with its phonon heat capacity C_p and its temperature T_p is coupled to the absorber by the Kapitza coupling G_K . The coupling between the phonon system and the electron system of the thermometer, with its electron heat capacity C_e and its temperature T_e , is the electron-phonon coupling G_{ep} .

Based on the fact that the phonon heat capacity of the thermometer C_p is negligibly small compared to the electron heat capacity of the thermometer C_e as well as the

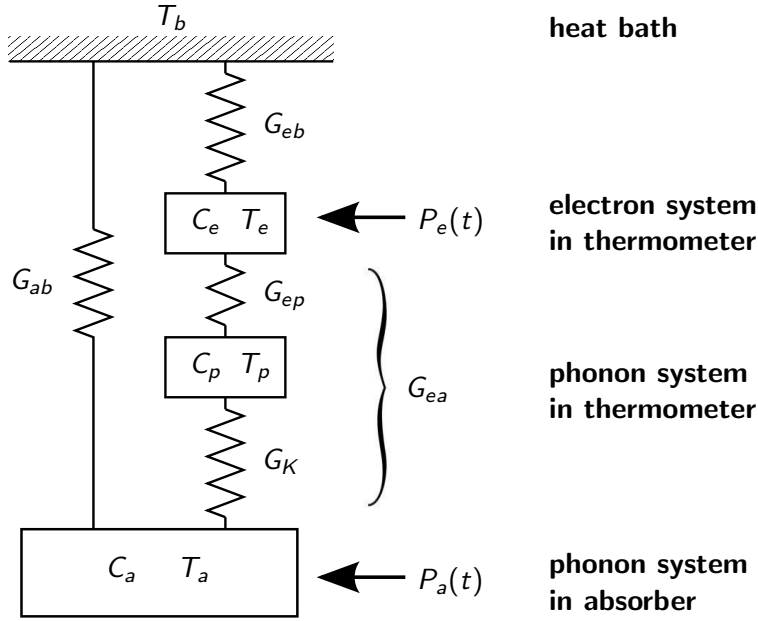


Figure 4.3: Scheme of the thermal model of the cryogenic calorimeter [93]. The absorber is characterized by its temperature T_a and its phonon heat capacity C_a . The electron system and the phonon system of the thermometer can have different temperatures T_e and T_p , respectively. C_e and C_p are the corresponding heat capacities. The phonon system of the absorber is coupled to the phonon system of the thermometer by the Kapitza coupling G_K and the phonon and electron system of the thermometer are coupled by the electron-phonon coupling G_{ep} . These two couplings are replaced with an effective coupling G_{ea} in the model. Both, the absorber and the electron system of the thermometer, are coupled to the heat bath of temperature T_b with the couplings G_{ab} and G_{eb} , respectively. The power inputs are displayed by arrows: Thermal phonons transmit power in the absorber $P_a(t)$ and non-thermal phonons transmit power directly into the electron system of the thermometer $P_e(t)$.

absorber heat capacity C_A , the model can be simplified by defining an effective coupling G_{ea} between the phonon system of the absorber and the electron system of the thermometer:

$$\frac{1}{G_{ea}} = \frac{1}{G_K} + \frac{1}{G_{ep}}. \quad (4.12)$$

The main assumption of the thermal model of [93] is the existence of only two states of phonons - namely the non-thermal phonons and the thermal phonons - instead of a continuous frequency distribution. This assumption is well motivated as mainly phonons of these two states transfer energy in the the electron system of the thermometer. Due to the before-mentioned strong coupling of electrons in the thermometer film and non-thermal phonons, the latter transfer energy efficiently into the electron system of the thermometer. The electrons experience a time-dependent power input $P_e(t)$, which is the origin of the fast signal component. Additionally, the thermal phonons also transfer energy into the thermometer. They heat the phonon system of the absorber which is modeled by the power input $P_a(t)$ into the absorber and, thereby, are the origin of the slow component of the signal. The power inputs are drawn as arrows in figure 4.3.

4.2.5 Signal Formation

The measured signal describes the change of temperature of the thermometer over time. The model describes the time-dependent energy input into the thermometer and the absorber, the following thermal adjustments of the systems via the thermalized phonons, and the relaxation of the detector system back to the initial conditions.

The energy ΔE deposited in the absorber in an interaction, creates non-thermal phonons. These can be absorbed by the thermometer electrons, can decay in the absorber, or escape through the holding clamps. The fraction of non-thermal phonons, which is absorbed by the thermometer is denoted by ε .

The time-dependent power inputs of non-thermal phonons in the thermometer $P_e(t)$ and of thermal phonons in the absorber $P_a(t)$ can be modeled by the following equations:

$$P_e(t) = P_0 e^{-t/\tau_n}, \quad P_a(t) = \frac{1-\varepsilon}{\varepsilon} P_0 e^{-t/\tau_n} \quad (4.13)$$

with the initial power input into the thermometer

$$P_0 = \varepsilon \Delta E / \tau_n \quad (4.14)$$

and the life time of the non-thermal phonons τ_n . The thermalization of non-thermal phonons in the thermometer competes with the thermalization in the absorber. Therefore, τ_n depends on the degradation time τ_{film} caused by absorptions in the thermometer and the degradation time $\tau_{crystal}$ caused by the thermalization in the absorber:

$$\frac{1}{\tau_n} = \frac{1}{\tau_{film}} + \frac{1}{\tau_{crystal}}. \quad (4.15)$$

The time constant $\tau_{crystal}$ is a property of the crystal and in particular of the crystal surface. It scales with the mean scattering length of phonons in the crystal \widehat{l}_{sc} , which scales with the ratio between the volume V_a and the surface area of the absorber A_a [102]:

$$\tau_{crystal} \propto \widehat{l}_{sc} \propto \frac{V_a}{A_a}. \quad (4.16)$$

The proportionality factor, which is investigated in [102], depends on the geometry and the surface of the crystal.

The time constant for the thermalization in the film is given by:

$$\tau_{film} = \frac{\tau_0}{\bar{\eta}}, \quad \tau_0 = \frac{2V_a}{A_t \langle v_{\perp} \alpha \rangle} \quad (4.17)$$

where $\bar{\eta}$ is the effective absorption probability of non-thermal phonons transmitted into the thermometer (see table 4.3), τ_0 is the ideal thermalization time for complete thermalization in the thermometer ($\varepsilon = 1$) and complete absorption of non-thermal phonons transmitted into the film ($\bar{\eta} = 1$), A_t is the area of the absorber-thermometer interface, and $\langle v_{\perp} \alpha \rangle$ describes the transmission of the incident phonons over the interface averaged over modes and wave vectors (see table 4.3).

These two time constants also determine the fraction of non-thermal phonons absorbed in the thermometer ε :

$$\varepsilon = \frac{\tau_{crystal}}{\tau_{crystal} + \tau_{film}}. \quad (4.18)$$

After an energy deposition the time dependent temperatures of the electrons in the thermometer $T_e(t)$ and the phonons in the absorber $T_a(t)$ are changed due to the power inputs $P_e(t)$ and $P_a(t)$, respectively. The different thermal couplings adjust the temperatures afterwards.

The two time dependent temperatures $T_e(t)$ and $T_a(t)$ can be described by two coupled differential equations:

$$C_e \frac{dT_e}{dt} + (T_e - T_a)G_{ea} + (T_e - T_b)G_{eb} = P_e(t) \quad (4.19)$$

$$C_a \frac{dT_a}{dt} + (T_a - T_e)G_{ea} + (T_a - T_b)G_{ab} = P_a(t) \quad (4.20)$$

where T_b is the constant temperature of the heat bath. The measured thermometer signal is defined as:

$$\Delta T_e(t) = T_e(t) - T_b. \quad (4.21)$$

With the initial conditions $T_a(t=0) = T_e(t=0) = T_b$, the equations have the following solution [93] for the thermometer signal $\Delta T_e(t)$:

$$\Delta T_e(t) = \Theta(t) \left[S_n(e^{-t/\tau_n} - e^{-t/\tau_{in}}) + S_t(e^{-t/\tau_t} - e^{-t/\tau_n}) \right] \quad (4.22)$$

where the step function $\Theta(t)$ takes into account the assumption of an instantaneously established homogeneous distribution of non-thermal phonons in the absorber after the energy deposition. The solution consists of two components: a non-thermal component, that originates from the direct absorption of non-thermal phonons in the thermometer film with the signal amplitude S_n given by:

$$S_n = \frac{P_0}{\varepsilon} \cdot \frac{\frac{1}{\tau_{in}} - \frac{G_{ab}}{C_a}}{\left(\frac{1}{\tau_t} - \frac{1}{\tau_{in}}\right) \left(\frac{1}{\tau_{in}} - \frac{1}{\tau_n}\right)} \left(\frac{\frac{1}{\tau_t} - \frac{G_{ab}}{C_a}}{G_{eb} - \frac{C_e}{C_a}G_{ab}} - \frac{\varepsilon}{C_e} \right) \quad (4.23)$$

and thermal component, caused by the temperature rise of the absorber, as measured by the thermometer with signal amplitude S_t given by:

$$S_t = \frac{P_0}{\varepsilon} \cdot \frac{\frac{1}{\tau_t} - \frac{G_{ab}}{C_a}}{\left(\frac{1}{\tau_t} - \frac{1}{\tau_{in}}\right) \left(\frac{1}{\tau_t} - \frac{1}{\tau_n}\right)} \left(\frac{\frac{1}{\tau_{in}} - \frac{G_{ab}}{C_a}}{G_{eb} - \frac{C_e}{C_a}G_{ab}} - \frac{\varepsilon}{C_e} \right). \quad (4.24)$$

There are three time constants involved in equation 4.22:

- τ_n : the life time of the non-thermal phonons, that describes the thermalization in the thermometer (see equation 4.15),
- τ_{in} : the intrinsic thermal relaxation time of the thermometer,
- τ_t : the thermal relaxation time of the absorber.

The last two can be expressed as:

$$\tau_{in} = \frac{2}{a + \sqrt{a^2 - 4b}}, \quad \tau_t = \frac{2}{a - \sqrt{a^2 - 4b}} \quad (4.25)$$

where a and b are defined as:

$$a = \frac{G_{ea} + G_{eb}}{C_e} + \frac{G_{ea} + G_{ab}}{C_a}, \quad b = \frac{G_{ea}G_{eb} + G_{ea}G_{ab} + G_{eb}G_{ab}}{C_e C_a}. \quad (4.26)$$

For CRESST detectors the heat capacity of the thermometer is much smaller than the heat capacity of the absorber ($C_e \ll C_a$). Additionally, at the low operating temperature of the detectors (~ 15 mK) the thermal coupling between phonons and electrons in the thermometer is strongly suppressed ($G_{ea} \rightarrow 0$). Therefore, equation 4.25 can be simplified as [93]:

$$\tau_{in} \approx \frac{C_e}{G_{eb}}, \quad \tau_t \approx \frac{C_a}{G_{ab}} \quad (4.27)$$

Hence, the time constant of the thermometer τ_{in} can be controlled by the thermal conductance of the thermometer to the heat bath G_{eb} , which is defined by the gold structure that thermally couples the thermometer to the heat bath. The time constant of the absorber τ_t is defined by the thermal coupling between absorber and heat bath G_{ab} .

The suppression of the thermal coupling between the absorber and the thermometer also strongly suppresses the thermal component of the pulse S_t . With the assumptions of $C_e \ll C_a$ and $G_{ea} \rightarrow 0$, the amplitude of the non-thermal component (equation 4.23) can be simplified as:

$$S_n \approx \frac{P_0}{G_{eb} \left(1 - \frac{\tau_{in}}{\tau_n}\right) \left(1 - \frac{\tau_{in}}{\tau_t}\right)} = - \frac{\varepsilon \Delta E}{C_e \left(1 - \frac{\tau_n}{\tau_{in}}\right) \left(1 - \frac{\tau_{in}}{\tau_t}\right)} \quad (4.28)$$

Depending on the ratio of τ_{in} to τ_n the thermometer can be operated in two different modes, the calorimetric or the bolometric mode. These modes are explained in the following.

Calorimetric Mode

In a thermometer where $\tau_n \ll \tau_{in}$, the phonons flow faster in the thermometer than out of it. The thermal relaxation time τ_{in} is long enough for the thermometer to integrate over the power input from the non-thermal phonon population $P_e(t)$, which has the life time τ_n . This operating mode is referred to as *calorimetric mode*. The amplitude of the non-thermal component depends on the total energy deposited in the absorber:

$$S_n \approx - \frac{\varepsilon \Delta E}{C_e}. \quad (4.29)$$

In this mode S_n is negative and, hence, the life time of the non-thermal phonons τ_n defines the rise time of both signal component, while the thermal relaxation time of the thermometer τ_{in} defines the decay time of the non-thermal signal component and the relaxation time of the absorber τ_t determines the decay time of the thermal component (see equation 4.22).

The light detector thermometers, used in the CRESST experiment, are optimized to work in the calorimetric mode. Their coupling to the heat bath is adjusted for the

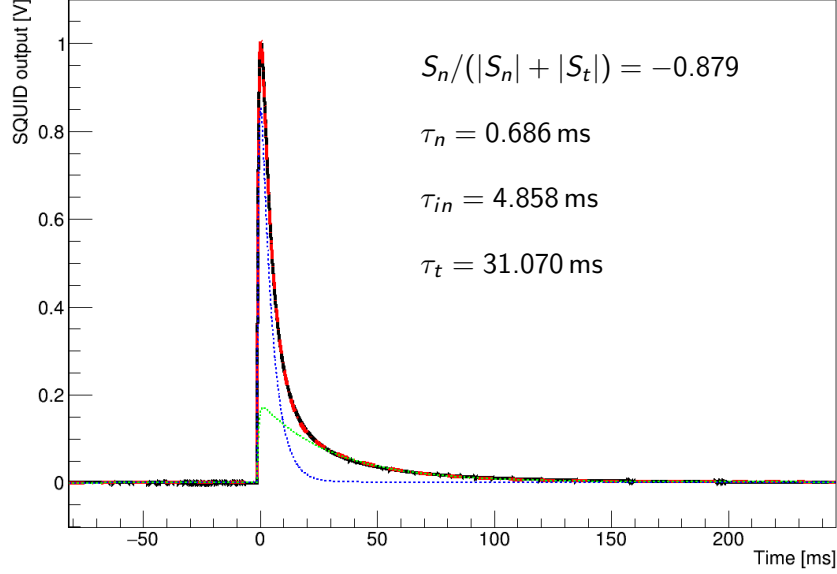


Figure 4.4: Normalized template pulse of a light detector measured in CRESST-II phase 2 which is operated in the calorimetric mode. The pulse model of equation 4.22 (red-dashed line) is fitted to the template (black). The non-thermal component is drawn as blue-dotted line, while the thermal component is drawn as green-dotted line. The given values for the time constants and the relation of the amplitudes result from the fit.

detection of the slow scintillation signal with a long decay time of CaWO_4 ($\tau_s \approx 400 \mu\text{s}$ at mK temperatures [103]).

A typical template pulse of a thermometer operated in the calorimetric mode (black) with the pulse model fitted to it (red dashed) is shown in figure 4.4. The given values result from the fit. The non-thermal component (blue dotted) accounts for 87.9% of the pulse, whereas the thermal component (green dotted) makes up only 12.1% of the total amplitude. As desired for a thermometer in the calorimetric mode, the life-time of non-thermal phonons τ_n , which is the rise time of both components, is much shorter than the other two decay times τ_{in} and τ_t . Typical values of the time constants in a calorimetric detector are $\tau_n \approx 0.5 \text{ ms}$, $\tau_{in} \approx 5 \text{ ms}$, $\tau_t \approx 30 \text{ ms}$.

Bolometric Mode

In a thermometer for which $\tau_{in} \ll \tau_n$ the phonons flow out of the thermometer faster than into it. Therefore, it is measuring the flux of the non-thermal phonons in the thermometer and, thus, is operating in the *bolometric mode*. The amplitude of the non-thermal component is proportional to the initial power input in the thermometer

$$S_n \approx \frac{P_0}{G_{eb}}. \quad (4.30)$$

Due to the proportionality of P_0 to the deposited energy ΔE , the amplitude S_n is an estimate of the deposited energy in the detectors and is can also be described as:

$$S_n \approx \frac{\varepsilon \Delta E}{\tau_n G_{eb}} \quad (4.31)$$

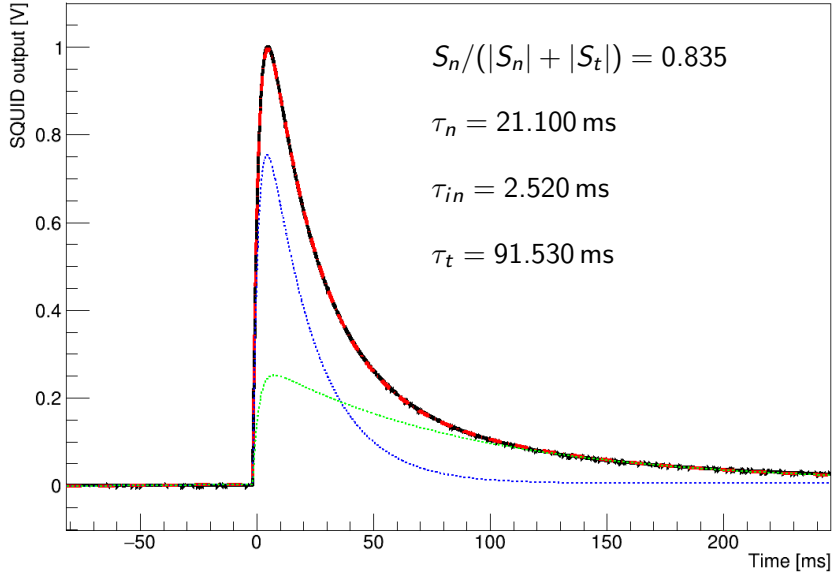


Figure 4.5: Normalized template pulse of a phonon detector measured in CRESST-II phase 2 which is operated in the bolometric mode. The pulse model of equation 4.22 (red-dashed line) is fitted to the pulse (black). The non-thermal component is drawn as blue-dotted line, while the thermal component is drawn as green-dotted line. The given values for the time constants and the relation of the amplitudes result from the fit.

With a positive S_n , the rise time of the non-thermal signal component is defined by the relaxation time of the thermometer τ_{in} and its decay time by the life time of the non-thermal phonons τ_n (see equation 4.22). As in the calorimetric mode the thermal component rises with the time constant τ_n and decays with the relaxation time τ_t .

The phonon detector thermometers, that were used in CRESST-II, were operated in the bolometric mode due to the long time needed for the thermalization of the non-thermal phonons.

A typical pulse of a detector operated in the bolometric mode (black) with the pulse model fitted to it (red dashed) is shown in figure 4.5. Also in this thermometer the non-thermal component (blue dotted) accounts for the larger part (83.5%) of the pulse compared to the thermal component (green dotted). Clearly visible are the different rise times of the two components. In this absorber the life time of non-thermal phonons τ_n is much longer than the relaxation time of the thermometer τ_{in} . Also compared to the light detector the life time of non-thermal phonons τ_n is much longer in the large absorber crystal of the phonon detector. Typical values of the time constants in a bolometric detector are $\tau_n \approx 20$ ms, $\tau_{in} \approx 3$ ms, $\tau_t \approx 90$ ms.

4.2.6 Electrothermal Feedback

During operation a constant bias current is sent through the thermometer. When a power input occurs in the thermometer its temperature and accordingly its resistance increases. Due to the readout scheme (see figure 2.11), this causes a reduction of the bias current through the branch of the thermometer and, thus, also a reduction of the heating of the thermometer due to the bias current. This effect causes the thermometer

to faster relax back into equilibrium and is called electrothermal feedback. It can be modeled as an additional thermal coupling to the heat bath and is defined as [92]:

$$G_{ETF} = I_B^2 R_S^2 m \frac{R_T - R_S}{(R_T + R_S)^3}, \quad (4.32)$$

where I_B is the total bias current, R_S is the shunt resistance, and m is the slope of the transition. The coupling G_{ETF} is fictitious and acts as a thermal conductance parallel to G_{eb} . In general, it can be positive or negative, depending on the difference $R_T - R_S$. A negative electrothermal feedback increases the coupling to the heat bath, while a positive electrothermal feedback reduces the coupling. This causes the intrinsic thermal relaxation time of a pulse to be changed from the physical time constant τ_{in} to an effective time constant τ_{eff} [92]:

$$\tau_{eff} = \frac{\tau_{in}}{1 + \frac{G_{ETF}}{G_{eb}}}. \quad (4.33)$$

CRESST detectors are operated with a weak negative electrothermal feedback⁴ ($R_T \gtrsim R_S$). Especially for CRESST phonon detectors the additional coupling G_{ETF} is small compared to the coupling G_{eb} ($G_{ETF} \ll G_{eb}$).

4.2.7 Phonon Collectors

CRESST detectors are optimized to measure non-thermal phonons. So-called phonon collectors can enlarge the fraction of non-thermal phonons that is absorbed in the thermometer without increasing the heat capacity of the thermometer. Thus, an enlargement of the signal in the calorimetric detector is expected⁵.

Phonon collectors consist of thin superconducting films well below their transition temperature and partly overlap the thermometer film. As mentioned in section 4.2.1, in a superconductor well below its transition temperature, nearly all electrons are combined to Cooper-pairs and do not contribute to its heat capacity. Therefore, the heat capacity of the phonon collectors is determined only by the phonon system, which can be neglected compared to the heat capacities of the other components of the detector.

Phonon collectors can increase the energy transfer into the thermometer by an additional energy transport from the absorber through the phonon collectors into the thermometer. A non-thermal phonon can be absorbed in the phonon collectors and, if its energy is greater than twice the band gap, it breaks up Cooper pairs, which then form quasi particles. The quasi particles diffuse like a gas through the collector and emit phonons which break further Cooper pairs. Part of the energy transmitted by non-thermal phonons is re-emitted into the absorber. However, roughly 50% of the energy remains in excited quasi particles [105].

The quasi particles can recombine or diffuse slowly into the thermometer film. Via this diffusion the quasi particles transport additional energy into the thermometer and

⁴Transition edge sensors can be operated in a strong negative electrothermal feedback mode. This results in a pulse shortening that allows to increase the count rate [104].

⁵The signal of a bolometric detector does not depend on its heat capacity and, thus, phonon collectors can not increase its signal height. For this reason phonon collectors are only utilized in calorimetric detectors.

thereby they can increase the sensitivity of the thermometer. When reaching the tungsten film, where the band gap vanishes, the quasi particles relax and release their energy to the electron system of the thermometer rising its temperature. As the recombination of Cooper pairs in the phonon collectors can cause signal losses, the transport of the quasi particles to the tungsten film determines the increase of signal height.

The mean free path of quasi-particles is determined by the elastic scattering on impurities and lattice defects. A high quality of the superconducting film is important to maximize the diffusion length.

In the calorimetric CRESST light detectors, phonon collectors are realized by large Al/W bilayers placed on two sides of the thermometer (see figure 4.2). Due the ratio of the thickness of aluminum ($d_{Al} = 1 \mu\text{m}$) and tungsten ($d_W = 0.2 \mu\text{m}$), the bilayer has a transition temperature close to the one of aluminum ($T_C = 1.1 \text{ K}$) and its heat capacity is negligible.

Quasi particle diffusion in CRESST detectors has been studied in detail in [106, 107], where a diffusion length of $\mathcal{O}(1 \text{ mm})$ has been observed. The diffusion length of quasi particles defines the maximum size of the phonon collectors. Further measurements, where the area and the thickness of the phonon collectors were increased, showed that signal can be gained with an increase of size compared to the standard geometry of the light detector thermometers used in CRESST-II Phase 2 [107].

4.3 Noise

The performance of a cryogenic detector is limited by the influence of various noise sources. In order to understand the performance of a detector and to optimize its design, it is important to identify the dominating noise contributions. In [92] a theoretical model describing the noise observed in CRESST detectors was developed⁶. Within the present section this model is reviewed.

4.3.1 Noise Sources

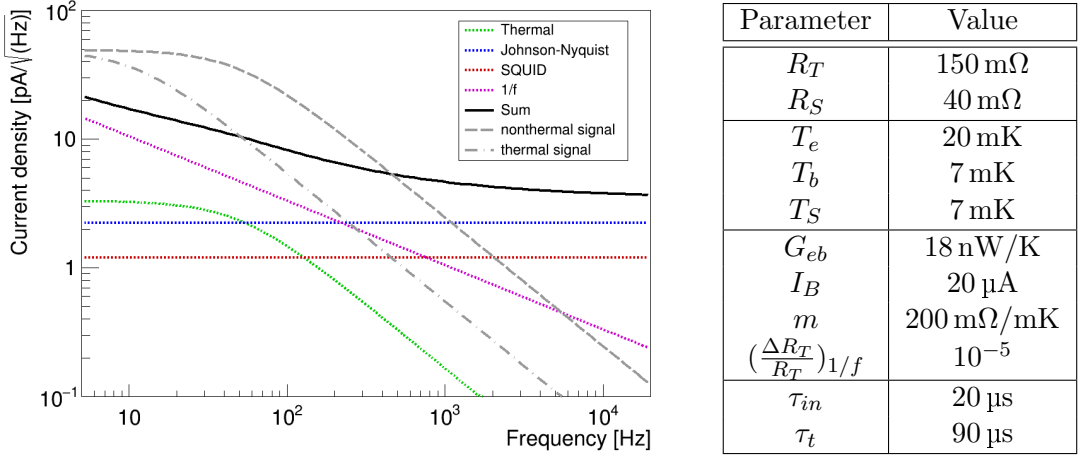
The noise in a calorimeter is produced by several uncorrelated noise sources [108]. Thus, the total output noise is the quadratic sum of all the sources. As the present work concentrates on the performance of phonon detectors, the effects due to electrothermal feedback are neglected here (see section 4.2.6).

To estimate the effect of the various noise sources, the signal is briefly discussed in the frequency domain. For a given power input P_e the thermometer behaves as a low pass system with one pole⁷ in the frequency response corresponding to τ_{in} [92]. The spectral response of the thermometer to an arbitrary power input is described by the responsivity of the thermometer $S(\omega)$:

$$S(\omega) = \frac{d\Delta I_s}{dP_e}, \quad (4.34)$$

⁶The theory of noise for a general model of bolometers and microcalorimeters is given in [108, 109].

⁷The power input P_e is assumed to occur instantaneous. As the finite time of the power input is short compared to the rise time of the thermometer it is not necessary to consider it here.



(a) Expected noise spectrum for a typical CRESST phonon detector

(b) Typical values for a CRESST phonon detector

Figure 4.6: Expected noise spectra for a typical CRESST detector (a). The sum of the noise spectrum (black) is made up of thermal noise (green), Johnson-Nyquist noise of the thermometer and the shunt resistance (blue), Johnson-Nyquist noise of the SQUID (red), and $1/f$ noise (magenta). The spectra were calculated for a typical CRESST phonon detector. The values used are given in the table (b). For comparison the contribution of the signal in the frequency spectrum is illustrated in gray for the non-thermal (dashed) and the thermal (dash dotted) signal. See text for details.

where ΔI_s is the current signal measured for a given power input P_e into the thermometer. The responsivity for the non-thermal signal of a CRESST thermometer is given by [92]:

$$S(\omega) = \frac{1}{1 + i\omega\tau_{in}} \frac{1}{G_{eb}} \frac{I_B R_S}{(R_T + R_S)^2} m, \quad (4.35)$$

with the variables defined as before. The thermal signal appears with a pole corresponding to the thermal decay time τ_t .

In figure 4.6a the frequency spectra of the non-thermal (gray dashed) as well as of the thermal signal (gray dash dotted) for a typical CRESST detector are illustrated. Additionally, the noise spectrum expected for a typical CRESST-II phonon detector with the values given in 4.6b is depicted (black). The contributions of the different noise sources are discussed in the following.

Thermal Noise

Thermal noise, also called phonon noise, occurs due to random energy fluctuations between the thermometer and its connected systems - in particular the link to the heat bath. This random energy flow in the link occurs permanently leading to a fluctuation of the energy content and, thereby, the temperature of the thermometer.

In thermal equilibrium, with the temperature of the detector being equal to the temperature of the heat bath ($T_e = T_b$), the power spectrum of the thermal noise is

white with a power flow of [108]

$$P_{th,eq} = \sqrt{4k_B T_e^2 G_{eb}}. \quad (4.36)$$

However, CRESST detectors are stabilized at a temperature higher than the heat bath. In this case the noise amplitude depends on the thermal link properties and the power flow in the thermometer has the spectral density⁸ [92, 108]

$$P_{th} = \left(4k_b T_e^2 G_{eb} \cdot \frac{2}{5} \frac{1 - \left(\frac{T_b}{T_e}\right)^5}{1 - \left(\frac{T_b}{T_e}\right)^2} \right)^{1/2} \quad (T_e > T_b). \quad (4.37)$$

Analog to the signal this noise is introduced in the thermometer and, thus, the resulting output current noise is determined by the responsivity of the thermometer $S(\omega)$ [92]. Hence, the spectrum of the thermal noise has the same shape as the spectrum of valid pulses (see figure 4.6).

The resulting output current noise due to the power input of thermal noise P_{th} is [92]

$$\sqrt{\langle |I_{th}(\omega)|^2 \rangle} = \sqrt{\langle |S(\omega)P_{th}(\omega)|^2 \rangle} = \sqrt{\frac{1}{1 + \omega^2 \tau_{in}^2} \frac{1}{G_{eb}} \frac{I_B R_S}{(R_T + R_S)^2} m P_{th}}. \quad (4.38)$$

In [92] for light detectors the contribution of thermal noise was determined to be comparable to other noise sources at low frequencies of up to $\mathcal{O}(10 \text{ Hz})$. Most of the parameters defining the thermal noise are similar for phonon and light detectors. Only two parameters differ strongly:

- The thermal coupling between the thermometer and the heat bath G_{eb} is much stronger for phonon detectors. For light detectors the value for G_{eb} at a temperature of 10 mK was determined to be $G_{eb} \approx 10 \text{ pW/K}$ [66]. For phonon detectors which are coupled with a gold bond wire, the value was determined to be $G_{eb} \approx 9000 \text{ pW/K}$ for a temperature of 10 mK [93].
- Also the bias current I_B is typically larger for phonon detectors compared to light detectors. In CRESST-II phase 2 phonon detectors were typically operated with a bias current of 10–25 μA , while light detectors could only be operated with a bias current of 0.5–3 μA .

These two parameters are related as the maximal usable bias current is limited by its power input in the thermometer. With a larger thermal coupling to the heat bath G_{eb} the thermometer can tolerate a larger bias current. In [110] it was shown that these parameters are expected to scale as $I_B \propto \sqrt{G_{eb}}$. The typical values of the two parameters stated above are consistent with this expectation.

For this reason, the contribution of the thermal noise is expected to be on a similar level for phonon and light detectors.

⁸A diffusive thermal conductivity of the heat link is assumed. This is a valid assumption for CRESST detectors as the mean free path of free electrons in the gold film and wire is small compared to the dimensions of the link.

Johnson-Nyquist Noise of the Thermometer and Shunt

Due to their thermal agitation electrons move randomly in a resistor. These fluctuations appear as white Johnson-Nyquist noise, independent of the applied bias current. In the readout circuit of CRESST detectors (see figure 2.11) both, the thermometer and the shunt resistance, contribute to this noise. In [92] this noise contribution was modeled as an additional current source where the resulting output current is described as:

$$\sqrt{\langle |I_J|^2 \rangle} = \sqrt{\frac{4k_B(T_e R_T + T_S R_S)}{(R_T + R_S)^2}}. \quad (4.39)$$

Thereby, T_S is the temperature of the shunt resistance. To reduce the contribution of the shunt as much as possible, the shunt resistance is installed in a place with the temperature of the heat bath. The contribution of this noise is independent of the frequency (see figure 4.6) and was determined in [92] to be in the order of $\mathcal{O}(1 \text{ pA}/\sqrt{\text{Hz}})$ in the CRESST main setup at Gran Sasso⁹.

Johnson-Nyquist Noise of the SQUID

The Josephson junctions of dc-SQUIDs have intrinsic thin film shunt resistors in parallel, which generate a white flux noise in the SQUID loop. This Johnson-Nyquist noise depends on the SQUID and cannot be influenced by modifications on the detector. For the dc SQUIDs used in the CRESST experiment the noise of the SQUIDs was determined to be $\sqrt{\langle |I_{SQ}|^2 \rangle} = 1.2 \text{ pA}/\sqrt{\text{Hz}}$ [75].

1/f Noise

Another noise source is the $1/f$ noise which seems to be connected to local resistance fluctuations in the thermometer film on microscopic scale [111]. Locally varying resistances can originate from defects [112, 113] or stress in the lattice [114].

This noise term is frequency dependent and is described as a fluctuation of the value of the film resistance [115]:

$$\left(\frac{\Delta R_T}{R_T} \right)_{1/f} \propto \frac{1}{\sqrt{\omega}}. \quad (4.40)$$

This results in a thermometer response to the $1/f$ noise of [92]

$$\sqrt{\langle |I_{1/f}|^2 \rangle} = \frac{I_B R_T R_S}{(R_T + R_S)^2} \left(\frac{\Delta R_T}{R_T} \right)_{1/f}. \quad (4.41)$$

This noise source is as well illustrated in figure 4.6.

In [92] it was shown that $1/f$ noise is the dominant contribution for low frequencies and that is increased for operating points low in the superconducting transition. For this reason, an operating point in the upper part of the transition is typically preferred¹⁰.

⁹The only difference to the test setup in Munich is a slightly different temperature of the shunt resistance T_S due to a slightly higher temperature of the heat bath in the test setup. However, as the shunt resistance R_S is the same, this noise contribution is not significantly different in both setups.

¹⁰Actually the preferred operating point has a high signal-to-noise ratio. However, it is observed that the noise in the lower part of the transition increases more than the signal.

Other Noise Sources

The noise sources discussed up to now depend only on the thermometer itself or on the SQUID and are independent of the remaining setup. However, there are additional noise terms induced by the setup, such as external disturbances like temperature fluctuations of the heat bath, vibrations or electrical interferences. These external noise sources can be suppressed by a careful design of the experimental setup and an active temperature control. For the CRESST setup at Gran Sasso as well as for the test setup in Munich large efforts are done to reduce the noise as much as possible (e.g. Faraday cage and mechanical decoupling of the cryostat).

4.4 Measured Noise Contribution

Within the present work measurements done in different setups are compared. It is observed that the noise contributions in the CRESST main setup and a test setup significantly vary.

4.4.1 Baseline Noise

The relevant quantity that is typically determined to describe the noise contribution for CRESST detectors is the baseline noise. Within the present work the latter is determined from empty baselines, i.e. records triggered randomly by the DAQ. To determine the baseline noise a template pulse of fixed height is superimposed to these empty baselines and the resulting artificial pulse is fitted with the template [74]. The width σ of the resulting Gaussian peak in the amplitude distribution is determined. It equals the baseline noise, since only the baseline noise contributes to the uncertainty of the pulse height.

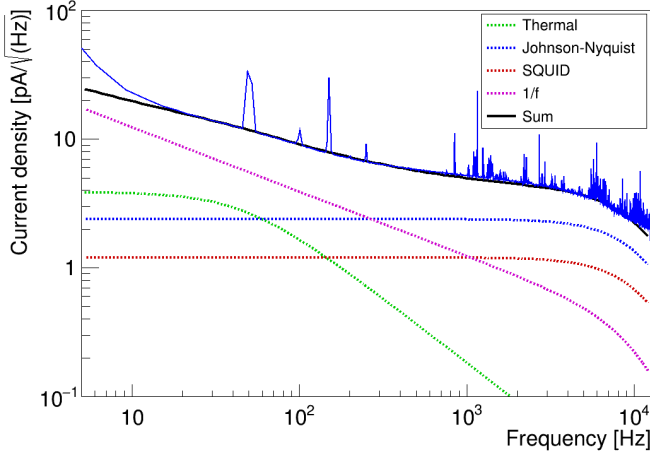
Typically the absolute measured baseline-noise level in terms of voltage is observed to be similar for all detectors operated in the CRESST setup. This is expected as the parameters defining the noise sources discussed before are similar or equal for all detectors.

For example the phonon detector with the lowest energy threshold in CRESST-II phase 2 named Lise has a baseline noise of $\sigma_{P,0}^U = 0.9$ mV. The phonon detector with the best overall performance in CRESST-II phase 2 named TUM40 has a baseline noise of $\sigma_{P,0}^U = 0.7$ mV. In CRESST-II phase 2 the baseline noise of the different phonon detectors varies by a factor of ~ 3 between the best and the worst detector. For light detectors the baseline noise is in average slightly larger compared to phonon detectors. The lowest baseline noise for a standard light detector measured in CRESST-II phase 2 (with the detector named Leon) is $\sigma_{L,0}^U = 1.4$ mV. Also for the light detectors the noise varies by a factor of ~ 3 between the best and the worst detector.

However, it is observed that the noise level measured in the test setup in Munich is considerably larger by a factor of up to ~ 10 (for examples see chapter 7).

4.4.2 Measured Noise Spectra

The noise spectra measured in the different setups are compared in the following. To determine the noise spectra empty baselines are exploited, as they are a sample of the



(a) TUM40

Parameter	Value
R_T	110 m Ω
R_S	40 m Ω
T_e	18.5 mK
T_b	7 mK
T_S	7 mK
G_{eb}	7.4 nW/K
I_B	20 μ A
m	100 m Ω /mK
$(\frac{\Delta R_T}{R_T})_{1/f}$	10^{-5}
τ_{in}	21.1 μ s

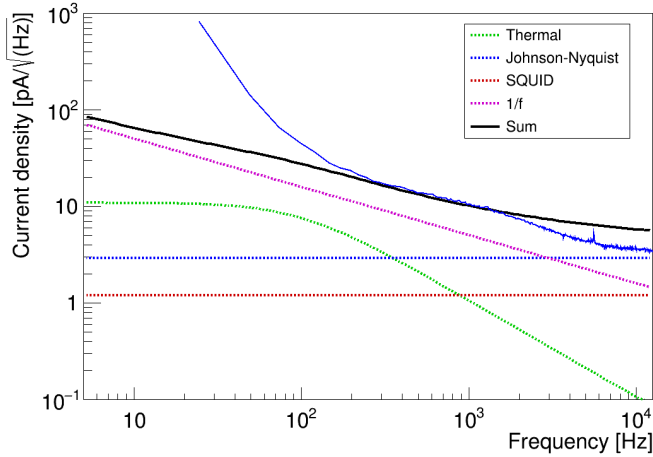
(b) Values for TUM40

Figure 4.7: Noise spectrum of the phonon detector TUM40 (a). The frequency spectrum of empty baselines measured in the main CRESST setup is shown in blue, while the expected noise spectrum is shown in black. The latter is the sum of the individual noise contributions due to thermal noise (green dotted), Johnson-Nyquist noise of the thermometer and the shunt (blue dotted), SQUID noise (red dotted) and $1/f$ noise (magenta dotted). The individual contributions are calculated with the parameter values determined for TUM40 as given in (b). The amplitude of the $1/f$ noise is varied to obtain best matching with the observed spectrum.

noise. The frequency spectra of empty baselines measured with TUM40 in the main CRESST setup in Gran Sasso is shown in figure 4.7a in blue. In this spectrum many sharp lines are visible. They can be attributed to electric interferences (e.g. at 50 Hz) or to mechanical vibrations induced by the cryogenic facility¹¹. At high frequencies the spectral density drops due to an anti-aliasing filter with a cut-off frequency set at 10 kHz during CRESST-II phase 2.

The expected noise spectrum (black line) is the sum of the individual noise contributions due to thermal noise (green dotted), Johnson-Nyquist noise of the thermometer and the shunt (blue dotted), SQUID noise (red dotted) and $1/f$ noise (magenta dotted). They are calculated with the parameters given in figure 4.7b according to the equations given in section 4.3. The parameters are determined from the pulse shape of TUM40 (τ_{in} , G_{eb}) or from a measurement of its superconducting transition (R_T , T_e , m). The bias current I_B is chosen for the detector at the beginning of the measurement and the temperatures of the SQUID T_S and the heat bath T_b are given by the setup. The only parameter that is not known a priori is the amplitude of the $1/f$ noise $(\frac{\Delta R_T}{R_T})_{1/f}$. The latter was varied to obtain best matching with the observed spectrum. Over a wide frequency-range the expected and the observed noise spectrum match well. Only at low

¹¹In a dilution refrigerator, as used in CRESST, a precooling is achieved by pumping on a volume of liquid helium. In this way, this volume is cooled to a temperature of 1 K and the helium becomes superfluid. The continuous refilling from a bath with liquid helium can induce a noise contribution at discrete frequencies in the high-frequency range similar to the one observed in figure 4.7a [116]. The test setup in Munich was modified similar to the solution proposed in [116]. This might explain why fewer of such noise peaks are observed in the test setup (see figure 4.8).



(a) TUM26-b

Parameter	Value
R_T	58 m Ω
R_S	40 m Ω
T_e	18 mK
T_b	10 mK
T_S	10 mK
G_{eb}	113 pW/K
I_B	22 μ A
m	13 m Ω /mK
$(\frac{\Delta R_T}{R_T})_{1/f}$	$3 \cdot 10^{-5}$
τ_{in}	10.3 μ s

(b) Values for TUM26-b

Figure 4.8: Noise spectrum of the phonon detector TUM26-b (a). The frequency spectrum of empty baselines measured in the a test setup is shown in blue, while the expected spectrum is shown in black. The latter is the sum of the individual noise contributions due to thermal noise (green dotted), Johnson-Nyquist noise of the thermometer and the shunt (blue dotted), SQUID noise (red dotted) and $1/f$ noise (magenta dotted). The individual contributions are calculated with the parameter values determined for TUM26-b as given in (b). The amplitude of the $1/f$ noise is varied to obtain best matching with the observed spectrum.

frequencies ($\lesssim 10$ Hz) a small additional contribution is observed.

A noise spectrum measured in a test setup in Munich with the detector TUM26-b is shown in figure 4.8a (blue line). Compared to the spectrum measured in the main CRESSST setup only a few less pronounced lines at large frequencies are visible. This indicates that the detectors in the test setup are less influenced by electric interferences and mechanical vibrations.

Also for this detector the expected noise contributions (dotted lines) are calculated with the parameters given in figure 4.8b. Due to the measurement conditions the parameters determined in the transition measurement exhibit large uncertainties. Details on this detector and its parameters can be found in chapter 7. Similar to the noise spectrum of TUM40 the amplitude of the $1/f$ noise $(\frac{\Delta R_T}{R_T})_{1/f}$ was varied to obtain best matching of the total expected spectrum (black) with the observed spectrum. In this case the amplitude of the $1/f$ noise is higher by a factor of 10 compared to the amplitude in the detector TUM40. The contribution from the Johnson-Nyquist noise as well as the SQUID noise are similar. Due to the relatively high bias current of 22 μ A together with the low thermal coupling G_{eb} the amplitude of the thermal noise is significantly higher.

For high frequencies $\gtrsim 200$ Hz the measured noise spectrum is well described by the expectations. The slightly higher expectations in the kHz region is due to a filter, which is not modeled in the expected spectrum. However, for small frequencies below ~ 200 Hz a large additional noise contribution is observed. Hence, there must be an additional noise source that causes a difference in the low-frequency range where also

the signal contribution is expected. This additional contribution is more pronounced in the test setup compared to the main CRESST setup. The test setup is located above ground and, thus, the observed event rate is significantly higher compared to the main setup at Gran Sasso. A high rate leads to events where the detector has not completely relaxed back to its operating point. Therefore, the resulting record features a pulse located on top of a non-flat baseline. Records with a non-flat baseline reduce the quality of the template fit and, thus, introduce larger uncertainties in the determination of the energy¹². In the case of empty baselines, the resulting records feature a signal component and appear in the low-frequency range of the noise spectrum just as the signal.

This can explain the rise of the spectrum determined from empty baselines measured in the test setup at low frequencies. It also indicates, that the higher noise contribution is mainly determined by the experimental site. Thus, the noise is expected to be smaller in the main CRESST setup at Gran Sasso.

4.5 Signal-to-Noise Ratio and Threshold

The signal-to-noise ratio defines the sensitivity of a detector. An increased signal-to-noise ratio is beneficial for the energy resolution and reduces the achievable threshold. Thus, for an improvement of the detector performance, the aim is to maximize the signal (see section 4.2) and/or reduce the noise (see section 4.3). Within the present work the focus is on the maximization of the signal. The parameters defining the noise are aimed to keep similar.

Up to now only the voltage amplitude of the noise was discussed. However, far more interesting for the estimation of the detector performance is the noise in terms of energy. During the procedure of calibration the measured signal height is related to an energy (see section 2.5). In this procedure also the baseline noise is associated with an energy which depends on the signal of the detector. In contrast to the measured noise level in terms of voltage, the baseline noise in terms of energy strongly depends on the detector type. The reason for this is that different detector types produce a differently large signal.

For the phonon detectors with the best performance in CRESST-II phase 2 Lise and TUM40 the resulting baseline noise is determined to be $\sigma_{P,0}^E = (62 \pm 1) \text{ eV}$ and $\sigma_{P,0}^E = (73 \pm 1) \text{ eV}$, respectively¹³. For the light detectors the baseline noise depends on the calibration procedure. Within the standard procedure the light detectors are calibrated with the scintillation light that a calibration source produces in the absorber crystal. The lowest value for the baseline noise of $\sigma_{L,0}^E = (197 \pm 1) \text{ eV}_{\text{ee}}$ is determined for the light detector Leon. With an absolute calibration this corresponds to a baseline noise of $\sigma_{P,0}^{E,abs} = (3.9 \pm 0.1) \text{ eV}$.

The achievable energy threshold of a detector depends on the baseline noise as a signal can only be recognized if it is larger than the noise. However, due to the hardware trigger the measured threshold is defined by the trigger level in CRESST-II. The level

¹²Already in the CRESST setup such records influence the template fit despite the low rate. In [71, 76] methods to improve the quality of the template fit for records with non-flat baselines are investigated.

¹³The values for the baseline noise determined here are comparable to the values published in [74, 76].

of the hardware trigger is set at a value above the baseline noise level so that the amount of noise triggers is close to zero. It is chosen individually for each detector at the beginning of a measurement but cannot always be set to a value very close to the baseline noise. One example where this is not possible are detectors with a noise level varying in time, e.g. due to mechanical vibrations caused by the cryogenic facility. There the trigger level can only be set to a level above the highest observed noise level. Still, for most detectors in CRESST-II phase 2 it was possible to optimize the trigger level slightly above the noise. With the best detectors in CRESST-II phase 2, namely Lise and TUM40, an energy threshold of $E_{th} = 307 \text{ eV}$ [74] and $E_{th} = 409 \text{ eV}$ [76] was reached, respectively¹⁴. Thus, the threshold achieved corresponds to 5.0 and 5.6 times the baseline noise, respectively. Within the present work it is assumed that for the best detectors a threshold of five times the baseline noise is achievable.

¹⁴After the publication of [67] the thresholds of all detectors were further optimized and could be lowered for several detectors (among them the detector TUM40).

Chapter 5

Detector Optimization for Low-Mass Dark Matter

As discussed before, CRESST-III aims to increase the sensitivity to low-mass dark matter. In chapter 3 it is shown that the most important parameter for the sensitivity in the low-mass dark matter region is a reduction of the energy threshold of the phonon detector. An enhancement of the performance of the light detector helps to reduce the background but is rather a complementary improvement. For this reason, the focus of the detector optimization for low-mass dark matter is a reduction of the phonon detector threshold. The aim is to obtain an energy threshold of 100 eV or even lower. Therefore, the signal-to-noise ratio needs to be increased. For the present CRESST detectors a reduction of the noise seems to be hard to achieve and, therefore, the goal of the optimization is to enhance the signal level without increasing the noise.

For an enhancement of the signal, the geometry of the absorber crystal must be changed. In section 5.1 the influence of the geometry of the absorber crystal on the signal height is investigated and the expectations for an adapted geometry are estimated. An adjustment of the TES structure to the new crystal geometry is necessary to detect the best signal. A TES for the new crystal geometry is introduced in section 5.2 for a detector operated in the bolometric as well as for a detector operated in the calorimetric mode. The optimization of the crystal is expected to result in an enhancement of the light output and, additionally, an adaption of the light detector to the new crystal geometry is expected to improve the light detector performance (see section 5.3).

5.1 Absorber Crystal

In section 4.2 the model for the signal of the cryogenic calorimeters used in CRESST is explained. Based on this model, the influence of the geometry of the absorber crystal on the signal is discussed in the following.

5.1.1 Influence of the Absorber Crystal Geometry on the Signal Height

The signal measured in the calorimeters used in CRESST, consists of two components: The non-thermal and the thermal component (see section 4.2). As the thermal component of the signal is strongly suppressed, the following discussion focuses only on the amplitude of the non-thermal component A_n .

In first approximation the signal height depends on the heat capacity of the thermometer C_e in the calorimetric mode and on the coupling of the thermometer to the

heat bath G_{eb} in the bolometric mode (see equations 4.29 and 4.31, respectively). In both operation modes the size of the target crystal does not affect the non-thermal component directly. However, in both cases the amplitude A_n is proportional to the fraction of non-thermal phonons absorbed in the thermometer ε . Two processes define this fraction (see equation 4.18): The thermalization of non-thermal phonons in the absorber (described by the time constant $\tau_{crystal}$) and the thermalization in the thermometer film (described by time constant τ_{film}).

The time constant $\tau_{crystal}$ is expected to scale as the ratio V_a/A_a , where V_a is the volume of the absorber and A_a is the surface area of the absorber. For two different crystals, crystal A and crystal B , differing in size and geometry, the respective ratios of volume and surface are $(V_a/A_a)^A$ and $(V_a/A_a)^B$. The thermalization time of non-thermal phonons in the crystal $\tau_{crystal}$ differs in the following way:

$$\tau_{crystal}^B = \frac{(V_a/A_a)^B}{(V_a/A_a)^A} \cdot \tau_{crystal}^A = \delta \cdot \tau_{crystal}^A, \quad (5.1)$$

where the superscripts A and B denote the values in the respective crystal.

In order to keep the fraction of non-thermal phonons being absorbed by the thermometer constant, the time constant for the thermalization in the thermometer τ_{film} has to be adapted with the same factor δ :

$$\tau_{film}^B = \delta \cdot \tau_{film}^A. \quad (5.2)$$

As τ_{film} is proportional to V_a/A_t (see equation 4.17), this is achieved by changing the area of the thermometer A_t by the same amount as the area of the absorber A_a :

$$A_t^B = \frac{A_a^B}{A_a^A} A_t^A. \quad (5.3)$$

By this adaption of the thermometer area, the fraction of non-thermal phonons being absorbed by the thermometer is kept constant:

$$\varepsilon^B = \frac{\tau_{crystal}^B}{\tau_{crystal}^B + \tau_{film}^B} = \varepsilon^A. \quad (5.4)$$

Thereby, also the life-time of non-thermal phonons τ_n , which defines the pulse duration, is changed (see equation 4.15):

$$\tau_n^B = \delta \cdot \tau_n^A. \quad (5.5)$$

Up to now, all alterations are independent of the operation mode of the detector. The effect on the signal amplitude, has to be discussed separately for a detector operated in the bolometric and the calorimetric mode.

Bolometric Detector

The decisive requirement for an operation in the bolometric mode is that the relation $\tau_{in} \ll \tau_n$ is valid. Thus, due to the change of the decay time of the pulse τ_n , also the thermal relaxation time of the thermometer τ_{in} , which is in the case of a bolometric

detector the rise time of the pulse, must be adapted, so that this relation is always fulfilled. For τ_{in} the following relation is desired:

$$\tau_{in}^B = \delta \cdot \tau_{in}^A. \quad (5.6)$$

Due to $\tau_{in} \approx C_e/G_{eb}$ (see equation 4.27), the time constant is influenced by the previously discussed change of the heat capacity of the thermometer, which is done by the variation of its area A_t (see equation 5.3). As the thickness of the thermometer is not intended to be changed, the thermal coupling of the thermometer to the heat bath G_{eb} must be changed in order to adapt τ_{in} to the new time constant τ_n . The thermal coupling must be modified in the following way:

$$G_{eb}^B = \frac{1}{\delta} \cdot \frac{A_a^B}{A_a^A} G_{eb}^A. \quad (5.7)$$

According to equation 4.31 all the discussed changes result in the signal amplitude of the non-thermal component of a bolometric TES $S_{n,bol}$ to scale in the following way:

$$S_{n,bol}^B = \frac{A_a^A}{A_a^B} \cdot S_{n,bol}^A \quad (5.8)$$

This means, as long as the time constants and the thermometer are adapted in order to keep the collection efficiency of non-thermal phonons ε constant, the amplitude of the non-thermal component $S_{n,bol}$ only scales with the surface of the crystal for a detector operated in the bolometric mode.

Calorimetric Detector

For an operation in the calorimetric mode the relation $\tau_n \ll \tau_{in}$ must be fulfilled. Also in this case, τ_{in} is adapted by a change of the thermal coupling G_{eb} . In the calorimetric mode G_{eb} is much weaker compared to the bolometric mode. However, the value does not influence the signal height in first approximation.

With only the alterations discussed above, the amplitude of the non-thermal component (see equation 4.29) in the calorimetric mode $S_{n,cal}$ is expected to scale in the following way:

$$S_{n,cal}^B = \frac{A_a^A}{A_a^B} \cdot S_{n,cal}^A \quad (5.9)$$

Although different parameters are dominating the signal height in the calorimetric detector, also in this mode the amplitude only scales with the absorber surface.

In contrast to a bolometric detector, in the calorimetric mode further optimizations are possible. An additional reduction of the thermometer area A_t is expected to enlarge the signal further as the signal directly scales with the heat capacity of the thermometer C_e . However, also the fraction ε is also influenced by the size of the thermometer via the time constant τ_{film} as the latter scales with $1/A_t$ (see equation 4.17). A smaller thermometer area reduces the fraction ε . However, the amount by which ε is reduced, depends on the ratio of τ_{film} and $\tau_{crystal}$, whereby at least the latter is not known a priori. These time constants and the resulting expectations for the signal height are investigated further in section 7.2.3.

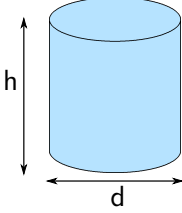
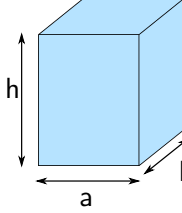
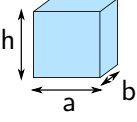
	cylindrical crystal CRESST-II phase 2 (conventional modules)	cuboidal crystal CRESST-II phase 2 (stick modules)	small crystal CRESST-III
			
measures [mm]	$h = d = 40$	$h = 40, a = b = 32$	$h = a = 20, b = 10$
mass [g]	300	249	24
V_a [mm ³]	$50.3 \cdot 10^3$	$40.96 \cdot 10^3$	$4.00 \cdot 10^3$
A_a [mm ²]	7540	7168	1600
V_a/A_a [mm]	6.7	5.7	2.5

Table 5.1: Comparison of different crystal geometries. The two large crystals were operated in CRESST-II phase 2 and are very similar in the given parameters. The small crystal is optimized for CRESST-III in order to provide an enhanced signal.

In conclusion, independent of the operation mode the amplitude of the non-thermal component A_n inversely scales with the absorber surface A_a , when the thermometer is adapted accordingly. In the calorimetric mode a further increase of the signal might be accessible by an optimization of the thermometer. This can be achieved by a reduction of the thermometer area or by the usage of phonon collectors.

5.1.2 Optimized Crystal Geometry for a Large Signal

The lowest thresholds achieved in CRESST-II phase 2 are $\sim 300 - 400$ eV [74]. To reach a threshold of 100 eV the signal must be increased by a factor of 3 – 4. As discussed, this is expected for an absorber crystal with a surface reduced by a factor of 3 – 4 compared to the crystals utilized in CRESST-II phase 2.

Therefore, for CRESST-III a cuboidal shaped absorber crystal with a size of $20 \times 20 \times 10$ mm³ is planned to be used. This size corresponds to a mass of ~ 24 g. In table 5.1 the different crystal geometries used in CRESST-II phase 2 are compared to the geometry of the small crystal for CRESST-III.

The area of the small crystal is reduced by a factor of ~ 4.5 to the cuboidal shaped crystal and ~ 4.7 compared and the cylindrical crystal operated in CRESST-II. The mass of this crystal is smaller by a factor of ~ 10 and ~ 12 compared to the cuboidal shaped and the cylindrical crystal, respectively.

With these changes, independent of the operation mode the signal amplitude S_n achievable with such a small crystal and an adapted TES structure is expected to be enhanced by a factor of ~ 4.5 compared to the large cuboidal shaped crystal and ~ 4.7 compared to the large cylindrical crystal. Assuming the same noise conditions as before

such an increase of the signal height can possibly reduce the threshold from the lowest thresholds measured in CRESST-II of $\sim 300 - 400$ eV to thresholds of $\sim 60 - 90$ eV.

5.2 Phonon Detector Thermometer

While the two crystal geometries utilized in CRESST-II have a similar ratio of crystal volume and surface and, thus, work well with the same TES structure, the small crystal has a very different ratio of volume and surface. Thus, for the new geometry the TES has to be adapted to be able to measure a large signal.

Due to the long life-time of the non-thermal phonons τ_n of 10–20 ms in the large crystals they have to be operated in the bolometric mode. An operation in the calorimetric mode would have implied very long pulses, which increases the probability for pile-up events, i.e. records with more than one pulse inside the record window. As the energy reconstruction might be spoiled for such records, this is not desirable.

Compared to the large crystals operated in CRESST-II in the small crystals the time constant for the phonon thermalization in the crystal $\tau_{crystal}$ is expected to be smaller by a factor of ~ 2.5 due to the different geometry. Therefore, the life time of non-thermal phonons τ_n is as well shorter which is why the calorimetric mode is easily accessible for the small crystals.

In contrast to the large phonon detectors operated in CRESST-II, the small crystals can be operated in the bolometric or in the calorimetric mode. The operation mode depends on the TES structure. Therefore, in the following, possible structures for each mode are discussed.

5.2.1 TES Structure for a Detector Operated in Bolometric Mode

In order to keep the same collection efficiency of non-thermal phonons ε the area of the tungsten film has to be reduced for a smaller crystal according to equation 5.3. Thus, with an area of the TES on the large crystal of 7.5×5.9 mm² (see figure 4.1) and the respective values for the crystal volume and area (see table 5.1), the area of the thermometer on the small crystal corresponds to $A_t \approx 9.6$ mm². The relation of length and width defines the resistance of the thermometer. Previous CRESST detectors typically had a resistance of 150–300 m Ω . In [110] it is shown that a small thermometer resistance can be beneficial for the signal level. For this reason compared to the structure operated in CRESST-II the resistance is slightly reduced to ~ 100 –200 m Ω by using an area of 4.8×2 mm².

In figure 5.1 an exemplary structure for a bolometric TES is depicted. This structure is very similar to the bolometric structure of the large crystals (see figure 4.1) with the necessary changes to operate it on the small crystal.

In order to adapt the rise time of the pulse τ_{in} , the thermal coupling to the heat bath G_{eb} also has to match. The TES of the large crystals have a thermal coupling of $G_{eb} = 18$ nW/K at a temperature of 20 mK which is achieved by a gold wire of ~ 2 mm length and a diameter of 25 μ m (see section 4.1). For the small bolometric thermometer the thermal coupling has to be reduced by a factor of ~ 1.8 (see equation 5.7). This can be achieved by a thinner gold bond wire e.g. a with a commercially available wire

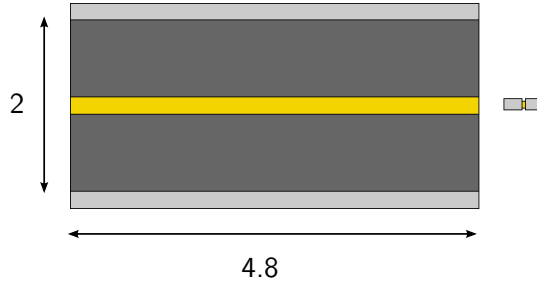


Figure 5.1: Possible structure of a bolometric TES with an area of the tungsten film (dark grey) of $4.8 \times 2 \text{ mm}^2$ for the small crystal with a size of $20 \times 20 \times 10 \text{ mm}^3$. The thermal coupling to the heat bath is given by a bond wire with a diameter of $12 \mu\text{m}$ attached to the gold stripe (yellow). The heater shown right of the thermometer is separated in order to reduce the noise. The aluminum structures (light gray) are used to attach the bond wires. All measures are given in millimeters.

with a diameter of $12 \mu\text{m}$ and a length of $\sim 1 \text{ cm}$, which is bonded on the gold stripe of the thermometer.

With such a TES a pulse with a rise time of $\sim 1 \text{ ms}$ and a decay time of $\sim 10 \text{ ms}$ are expected. Both are faster than pulses of the phonon detectors of CRESST-II but similar to the light detector pulses operated in CRESST-II.

In [66] it is shown that an electrically separated heater reduces the noise compared to a heater electrically connected to the TES. To obtain the lowest possible noise contribution a separated heater is employed in this design.

5.2.2 TES Structure for a Detector Operated in Calorimetric Mode

In contrast to the bolometric TES, for the calorimetric thermometer additional enhancements are viable. One possible additional improvement is a further reduction of the thermometer area A_T and, thus, its heat capacity C_e . At the same time, a smaller thermometer area increases the thermalization time τ_{film} and, thus, reduces the collection efficiency of non-thermal phonons ε (see equations 4.17 and 4.18). As the signal amplitude is proportional to ε/C_e (see equation 4.29), in total a signal increase is expected but the amount depends on the dependence of ε on the thermometer area A_T . However, to determine the actual dependence of the signal amplitude on the thermometer area, the parameters of the thermalization need to be known. The thermalization of phonons is investigated in section 7.2.3.

Another advantage of the calorimetric thermometer is the possible usage of phonon collectors (see section 4.2.7), which increase the area that is able to transport energy into the thermometer but do not increase the heat capacity.

In the design of a calorimetric TES for the small crystal both enhancements are exploited. Two different thermometer structures have been designed. The first design is depicted in figure 5.2a and has an area of the tungsten film of $3.4 \times 1.2 \text{ mm}^2$ and a total area of, which is a reduction by a factor of ~ 10 compared to the bolometric structure of the large crystals (see figure 4.1). Similar to the bolometric TES structure for the small crystal a resistance of $\sim 100\text{--}200 \text{ m}\Omega$ is expected.

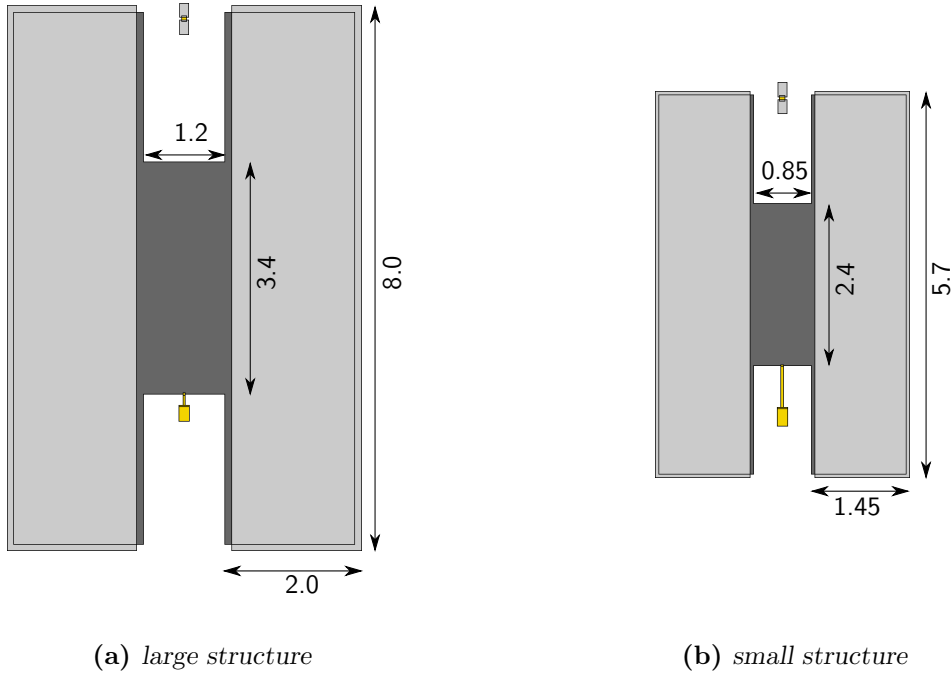


Figure 5.2: Possible structures for a calorimetric TES for an absorber crystal with a size of $20 \times 20 \times 10 \text{ mm}^3$. The areas of the tungsten film (dark gray) as well as the phonon collectors (light gray) differ by a factor of 2 and, thus, the length of these parts differs by a factor of $\sqrt{2}$. The thermal coupling is given by a gold structure (yellow). The heater on top of the picture is thermally and electrically separated. All measures are given in millimeters.

The calorimetric TES design exploits large phonon collectors. In [107] a diffusion length of the aluminum films used in CRESST detectors in the order of $\mathcal{O}(\text{mm})$ is measured. The design in figure 5.2a uses phonon collectors with a distance of up to $\sim 3 \text{ mm}$ to the tungsten film.

In order to operate a thermometer in the calorimetric mode, the thermal coupling to the heat bath has to be reduced drastically, so that the relaxation time of the thermometer is much larger than the life-time of non-thermal phonons ($\tau_{in} \gg \tau_n$). τ_n is expected to be in the order of $\mathcal{O}(1 \text{ ms})$. Therefore, the time constant of the thermometer τ_{in} should be in the order of $\mathcal{O}(10 \text{ ms})$. For such a decay time a coupling of G_{eb} in the order of $\mathcal{O}(100 \text{ pW/K})$ is necessary. This is achieved with a gold structure attached to the tungsten film, which is a thin stripe with a length of $150 \mu\text{m}$ and a width of $40 \mu\text{m}$.

In order to investigate the influence of the thermometer size, a second calorimetric TES structure with the area scaled down by a factor of ~ 2 was designed (see figure 5.2b). The tungsten film of the thermometer employs a size of $2.4 \times 0.85 \text{ mm}^2$. Also the size of the phonon collectors was scaled by the same amount. As the area and, thus, the heat capacity of the thermometer was reduced also the thermal coupling to the heat bath needs to be reduced which is achieved by a longer gold stripe.

Similar to the bolometric TES, also the calorimetric TES structures are equipped with a separated heater.

5.2.3 Operation Mode for the Phonon Detector with a small Crystal

To summarize, in the present work TES structures for the phonon detectors of the small crystal are designed. In contrast to CRESST-II, for the small crystals it is possible to operate the detector in the bolometric as well as in the calorimetric mode. However, each mode has certain advantages and disadvantages.

The structure for the calorimetric mode exploits additional features compared to the necessary changes discussed in section 5.1. On the one hand the area of the thermometer and, thus, the heat capacity was reduced further compared to the adaption necessary for the crystal geometry. On the other hand it is equipped with phonon collectors in order to increase the area able to absorb phonons without increasing the heat capacity. Both features increase the signal compared to the estimation given in section 5.1. Thus, according to the pulse model a lower threshold can be achieved with a TES operated in the calorimetric mode compared to one operated in the bolometric mode.

Energy depositions directly in the thermometer film, so-called *direct hits*, can cause records without a corresponding light signal. Thus, such an event cannot be discriminated from signal events in the light-yield parameter. As this is an instantaneous energy deposition in the thermometer film, in the bolometric mode the decay time is extremely short and such pulses can be discriminated by their peculiar pulse shape. In contrast, in the calorimetric mode a direct hit results in a faster rise time. As the latter is already in the $\mathcal{O}(1\text{ ms})$ for a particle pulse, a pulse with an even faster rise time is hard to distinguish especially for small pulses. In addition, a calorimetric TES features phonon collectors and an energy deposition in those is also possible. Due to the delayed energy transport from the aluminum into the tungsten film, such pulses can have rise times similar to normal pulses. Therefore, the pulse shape is very similar to absorber pulses. During CRESST-II phase 2 the number of observed direct hits for each phonon detector were in the order of $\mathcal{O}(100)$. With the planned size reduction of the calorimetric thermometer structures in the order of $\mathcal{O}(10)$ direct hits in the tungsten film are expected for each detector. However, as soon as some energy is deposited not only in the thin thermometer film but also in the crystal, such events can be distinguished by the scintillation light output. It was concluded, that the the expected direct hit events that cannot be distinguished is small.

In conclusion, in the calorimetric mode a larger signal is expected compared to the bolometric mode. A disadvantage might be the possibility of direct hits of the thermometer structure that do not produce light and can possibly not be distinguished. However it is expected, that their rate is negligible. Therefore, the small crystals are equipped with a calorimetric TES. Measurements with both structures shown in figure 5.2 are discussed in chapter 7.

5.3 Implications for the Light Channel

The reduction of the size of the absorber crystal is expected to result also in improvements in the light channel.

5.3.1 Light Output of the Crystal

Not all the light produced in the scintillating crystal can escape. Instead, the light output of the crystal is influenced by scattering and absorption of the light inside the crystal [117]. As the light produced in the small crystal has to cover a shorter distance more light is expected to escape the crystal.

A Monte-Carlo simulation performed in [118] confirmed that in a module with the small crystal more light can be absorbed by the light detector compared to a module with a cubic crystal operated in CRESST-II phase 2. Depending on the absorption length of the crystal up to two times more light can be collected.

However, this effect is decreased due to the direct evaporation of the tungsten film on the crystal. As mentioned in section 4.1, during the evaporation process the crystal is heated up, which results in a reduced light output of the crystal [59]. Therefore, in CRESST-II phase 2 most of the crystals were equipped with small TES-carrier crystals glued to the main absorber. However, the discrimination of TES-carrier events turned out to be difficult in particular for small energy depositions [76]. As the aim is to reduce the threshold of the phonon detector the TES are produced directly on the absorber crystal in order to avoid a TES carrier. A measurement of the light output before and after heating the crystal to the typical evaporation temperature of $\sim 450^\circ\text{C}$ showed a reduction of the light output of $\sim 20\%$ [119].

In total, it is expected that the light output of the small crystal is increased by a factor of ~ 1.5 compared to the crystals operated in CRESST-II phase 2.

5.3.2 Light Detector Geometry

Besides this effect further improvements are possible in the small module design. It is reasonable to match the size of the light absorber to the size of the crystal. In CRESST-II phase 2 a SOS light absorber with a diameter of 40 mm was used. For the optimized small crystal a light absorber with a size of $20 \times 20 \text{ mm}^2$ is foreseen, which results in a reduction of the light absorber volume by a factor of π compared to the light detectors operated in CRESST-II.

For the light detector no adjustment of the TES structure is required. The change of the absorber size influences the thermalization of phonons and, thus, the fraction of phonons being absorbed in the thermometer ε . The signal of the calorimetric thermometer is proportional to this fraction. In [66] it is shown that $\varepsilon \approx 5\%$ for light detectors. Thus, the time constant for the thermalization due to absorptions in the thermometer τ_{film} is 19 times longer than the time constant for the thermalization in the absorber $\tau_{crystal}$ (see equation 4.18). Therefore, it is possible to estimate the change of ε caused by the adjustment of the light detector.

The reduction of the volume of the light absorber by a factor of π implies a reduction of the surface by the factor $\sim 2\pi$. Due to these changes, the thermalization of phonons in the crystal with the time constant $\tau_{crystal}$ is expected to become longer by a factor of 2 (see equation 4.16). Additionally, the time constant describing the thermalization due to absorption in the film τ_{film} is expected to be shortened by a factor π (see equation 4.17). This results in τ_{film} being only three times larger than $\tau_{crystal}$ in the small light absorber and, hence, ε is expected to be around 25%. The enlargement of ε corresponds

to an increase of the signal amplitude¹ of the non-thermal component by a factor of $\sim 4 - 5$.

In conclusion, due the size reduction of the absorber crystal also the light detector improves its performance. On the one hand an additional light output of the crystal is expected and on the other hand the size reduction of the light absorber is expected to result in an increase of the signal amplitude. In total an increase of the signal amplitude by a factor of $\sim 6 - 7$ is expected.

¹This does not completely translate into an increase of the signal height, since also the life-time of non-thermal phonons τ_n increases and, thus, the rise time of the pulse. As long as the decay time of the pulse does not change, the actual increase of the signal might be slightly lower.

Chapter 6

The CRESST-III Low-Mass Dark Matter Detector Module

CRESST-III recently started to operate ten detector modules explicitly designed for low-mass dark matter searches. The optimizations of the detectors for a low threshold (< 100 eV) are discussed in chapter 5. Additionally, a major change of the detector geometry requires a new concept for the detector holder. In CRESST-II phase 2 three different fully-scintillating detector holders were operated successfully [76, 81] and, thus, they serve as conceptual basis for the new holding scheme. Moreover, with an ultra-low threshold new challenges arise for the holder. Backgrounds with even lower energy depositions have to be considered and new solutions to discriminate them have to be found.

In the present chapter an overview of the small module optimized for a low threshold is given. The detectors that are based on the optimization discussed in chapter 5 are described in section 6.1. The fully-scintillating detector holder for these optimized detectors is based on scintillating CaWO_4 sticks holding the detectors. The requirements and the concept for this detector holder are discussed in section 6.2. With a reduced energy threshold of the phonon detector even a fully-scintillating detector holder can cause backgrounds at lowest energies. In order to veto low-energetic events originating from energy depositions in the holding sticks, the sticks of the phonon detector are instrumented (see section 6.3).

6.1 Detectors

The design of the phonon detector results from the optimization discussed in chapter 5. The CaWO_4 absorber crystal optimized for a low threshold has a size of $20 \times 20 \times 10$ mm³, which corresponds to a mass of ~ 24 g. It is equipped with a TES operated in the calorimetric mode (see figure 5.2). For CRESST-III phase 1 three phonon detectors are equipped with the larger version of the calorimetric TES structure designed within the present work (see figure 5.2a) and seven phonon detectors are equipped with the smaller version (see figure 5.2b). In both cases the tungsten film is evaporated directly on the crystal in order to avoid events occurring in a TES-carrier.

To enhance the light output, the crystal is roughened on five sides [59]. The side where the thermometer is placed needs to be polished as a polished surface improves the quality of the evaporated tungsten film. The absorber crystal has small hatches where the CaWO_4 holding sticks are pressed onto (see figure 6.1). In order to avoid micro-fractures of the crystal, these hatches are spherically polished.

The size of the light detector is adapted to the reduced size of the absorber crystal. Therefore, the light detector consists of a SOS wafer with a size of $20 \times 20 \text{ mm}^2$ and a thickness of 0.46 mm and is equipped with a small calorimetric TES (see figure 4.2). Due to the reduction in size an increase of the signal height is expected. Additionally, an increased light output of the crystal is expected to increase the amount of detected light (see section 5.3).

6.2 Detector Holder Concept

With the optimized detectors being much smaller than the detectors operated in CRESST-II, also a new holding scheme is required.

6.2.1 Requirements for the Detector Holder

The new detector holder must fulfill certain requirements:

- In order to veto background induced by surface- α events the module housing needs to be fully-scintillating. In CRESST-II phase 2, different alternative designs with a fully-scintillating detector holders were successfully operated and showed that they are able to efficiently veto α -induced backgrounds. The new design is based on one particular design, namely the detector holder with the absorber crystal held by CaWO_4 sticks. For more details see e.g. [69].
- Mechanical stress on the CaWO_4 crystals causes stress-relaxation events, which are low-energetic events without a light signal. As such events can appear in the region of interest for dark-matter search, they need to be prevented. Such events were observed in the past due to a too tight clamping of the crystal [120] as well as in modifications of the clamps with scintillating plastic materials [63]. Another source for no-light events was observed due to a strong pressure on a roughened crystal surface, which might cause micro-fractures of the crystal [69]. This can be prevented or at least reduced by polishing all crystal surfaces in areas where pressure is applied to the crystal.
- In order to avoid external backgrounds all materials must be as radiopure as possible.
- The light collection and transportation to the light detector has to be ensured for a maximization of the detected light.
- The thermal coupling of the crystal via the holding structure must not be too strong in order to allow an operation of the detector as cryogenic calorimeter.
- The detectors have to be held in a stable position at mK temperatures in order to minimize mechanical vibrations, that can induce additional noise.

The modules are mounted in the carousel, which was designed for 33 cylindrical modules with an absorber crystal mass of $\sim 300 \text{ g}$. As the plan for future phases of CRESST is to mount 100 detector modules in the present CRESST setup [84], it is desired to design the outer dimensions of the module that allow for close packing.

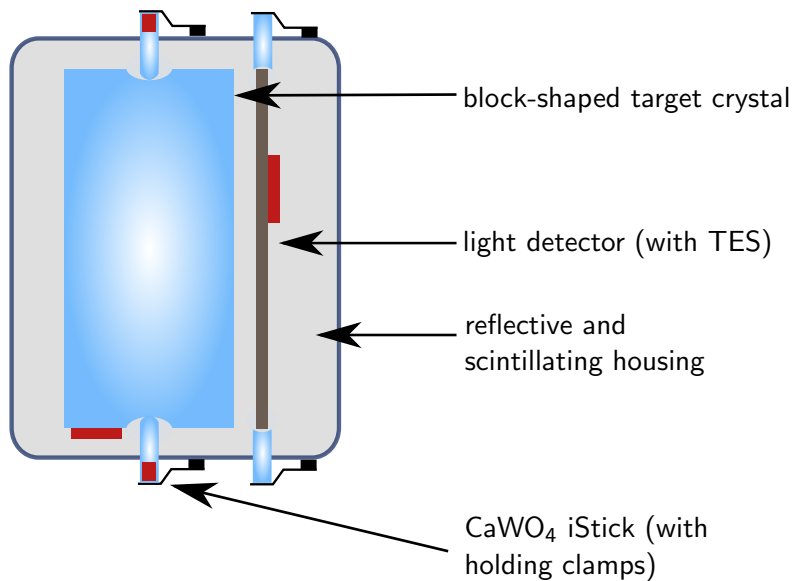


Figure 6.1: Schematic drawing of the small detector module. The phonon detector is depicted on the left side, while the light detector is shown on the right side of the housing. Both detectors are equipped with TES, which are depicted as red rectangles. The two detectors are enclosed by a scintillating and reflective surrounding. The phonon detector is held by scintillating CaWO_4 sticks, which are pressed against the crystal from outside the module by bronze clamps. The iStick TES are located outside the housing (red rectangles). The light detector is also held by CaWO_4 sticks.

6.2.2 Fully-Scintillating Housing

In the new holding scheme both detectors, the crystal as well as the light detector, are held by CaWO_4 sticks that are pressed against the crystal with bronze clamps from outside the housing. These bronze clamps maintain their flexibility also at mK temperature and, thus, can keep the detectors in a stable position without introducing mechanical stress. A schematic drawing of the module is shown in figure 6.1, while a photograph of an opened module is shown in figure 6.2.

Due to the small size and low weight of the CaWO_4 crystal, three CaWO_4 sticks are enough to hold it in position. Two sticks are pressed against the bottom of the crystal, while one is pressed against the top. The sticks have a polished spherical ending to provide a point-like contact to the absorber crystal (see figure 6.3a). They have a length of 12 mm and a diameter of 2.5 mm. In order to prevent sideways motions of the crystal, the latter features small hitches, where the sticks are pressed into. With this holding scheme, the crystal is held stable enough to rotate the module in any direction, which simplifies the mounting of the complete module.

Additionally, also the light detector is held by three CaWO_4 sticks. Similar to the crystal, it is held by two sticks on the bottom and one stick on the top of the detector. In order to stabilize the detector they are rounded concavely, such that the thin wafer cannot move sideways.

All copper parts are covered with scintillating and reflective foil on the inside of the housing. Thus, all parts inside the housing are either scintillating or active. The

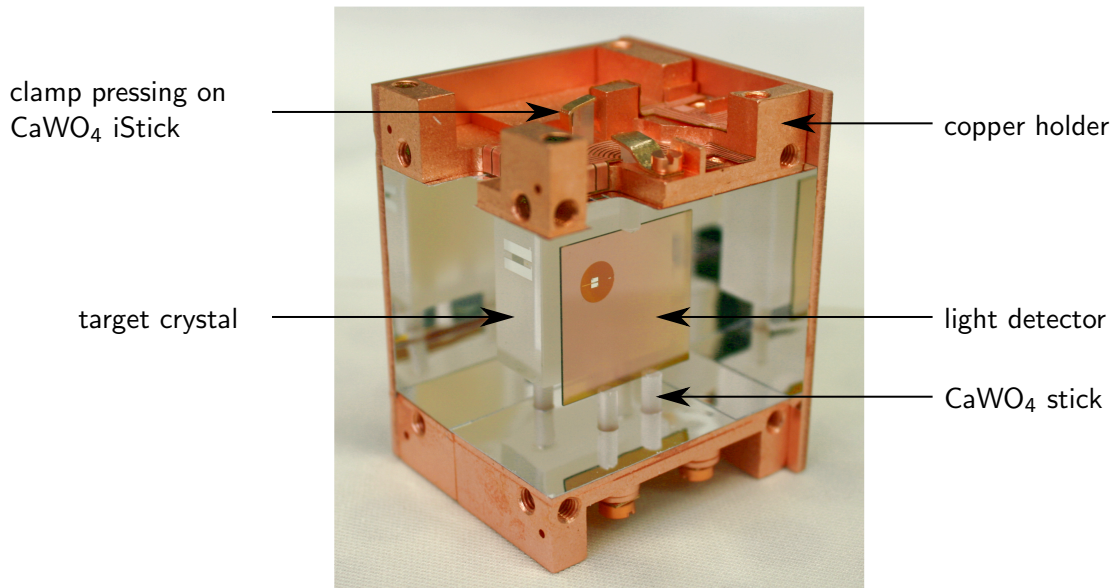


Figure 6.2: Photograph of an assembled detector module, where two sides of the housing are opened. The target crystal with its TES is visible in the back. In the foreground the brownish SOS light detector with its small TES can be seen. The darker circle around the TES is a silicon dioxide layer, that is evaporated on the light detector below the tungsten film in order to improve the film quality. Both detectors are held by CaWO₄ sticks. All three CaWO₄ sticks holding the light detector are visible. Only one of the bottom iSticks holding the phonon detector and the top iStick outside the copper housing can be seen. The clamps pressing the top sticks are visible outside the copper housing. The copper holder is surrounding the module on all sides. Each side can be opened individually. The reflective and scintillating foil is glued to the copper parts.

reflective and scintillating foil encloses the detectors completely except for openings where the sticks and the bondwires are fed through. The foil is cut in a way that such openings are minimized.

The top and the bottom of the housing are each made of a copper structure, with holes where the sticks are fed through. Additionally, the clamps to hold the sticks are screwed to these structures and the bond pads are glued onto them. The sides are each closed with a copper sheet with a thickness of 2 mm. These copper sheets are screwed to the top and bottom part and can be opened individually. A photograph of a fully-mounted detector module with two sides opened is shown in figure 6.2. The closed module with the outer dimensions of $55 \times 40 \times 35 \text{ mm}^2$ is block shaped, which allows a close packing of the modules.

6.3 Instrumented Holding Sticks

An energy deposition in the scintillating holding sticks produces phonons. A fraction of these phonons can be transferred into the absorber crystal via the point-like contact between stick and absorber crystal causing a low-energetic signal in the phonon detector. Additionally, as in the absorber crystal also in the CaWO_4 sticks scintillation light is produced. Events occurring in the scintillating sticks can be discriminated by the light signal as they appear in a band at quenching factors of ~ 20 -30 in the light yield - energy plane [69].

However, α -events induced by a surface contamination of the stick surface outside the scintillating housing can cause a dangerous background. Such a contamination can cause nuclear recoil events in the sticks with a deposited energy of 100 keV and below. Phonons produced during an energy deposition in a stick are partly transmitted via the point-like contact to the absorber crystal. Therefore, a nuclear recoil in a stick results in a degraded signal in the phonon channel with an energy of $\lesssim 1 \text{ keV}$ together with a very small light signal of $\lesssim 1 \text{ keV}_{ee}$. Such events can appear in the ROI for dark matter search and can cause a background. If they cannot be discriminated such events can limit the sensitivity of CRESST-III in particular for low dark-matter particle masses.

In order to be able to discriminate such a background in the new small module design the scintillating sticks holding the phonon detector are instrumented with a TES to directly measure the energy depositions in the sticks. This allows to veto all events occurring in the instrumented scintillating sticks, referred to as *iSticks*.

In [69] the energy-degradation effect through the interface of sticks to the absorber crystal is determined. The factor that quantifies the reduction of energy deposited in the sticks and energy measured in the crystal is found to be ~ 100 . Thus, an energy deposition of 10 keV in the stick, leads to an event of $\sim 100 \text{ eV}$ in the absorber crystal. Due to the energy degradation effect, the *iSticks* need an energy threshold of ~ 100 times the energy threshold of the crystal in order to veto all events efficiently. With the threshold estimated for the small phonon detector of 60 – 90 eV (see chapter 5) the *iSticks* require a threshold of $\mathcal{O}(1 \text{ keV})$ to veto all holder related background.

All small modules mounted for CRESST-III phase 1 are equipped with *iSticks*. While in the following the technical details of the *iSticks* are described, their performance is investigated in section 7.4.

6.3.1 Realization

Each of the three scintillating sticks holding the phonon detector is equipped with a TES. As discussed, the threshold required for the iSticks is $\mathcal{O}(1 \text{ keV})$. As this is not very challenging with such a small device and additionally a number of iSticks need to be produced (three per module), an easily producible realization was necessary.

For an easy manufacturing, about 100 TES are produced at once on one silicon wafer. Afterwards, this wafer is cut into small pieces with a size of $3 \times 3.5 \text{ mm}^2$ with each containing a single TES. Each CaWO_4 stick is equipped with one of these TES-carriers with a tiny glue spot of epoxy resin. With this technique, plenty of iSticks can be produced at once. A photograph of a complete iStick is depicted in figure 6.3a.

A schematic drawing of the iStick TES is depicted in figure 6.3b. Similar to the light detector TES (see figure 4.2), the thermometer consists of a small tungsten film with an area of $680 \times 140 \text{ }\mu\text{m}^2$ (dark gray in figure 6.3b) and utilizes phonon collectors with an area of $500 \times 1000 \text{ }\mu\text{m}^2$ each (large light gray areas). The thermal coupling is also provided by a thin gold structure with a length of $750 \text{ }\mu\text{m}$ and a width of $40 \text{ }\mu\text{m}$ (yellow stripe).

As the three iStick TES are connected electrically in their readout scheme (see section 6.3.2), the heater must be separated electrically to prevent electrical disturbances. However, compared to a heater electrically connected to the tungsten film, with a separated heater more heat is transferred in the absorber crystal for a certain heat input in the thermometer. Therefore with two or more detectors in direct contact, as it is the case for the absorber crystal and the iSticks, a part of the phonons produced in one detector can be transferred to the other. If these detectors do not have transition very close temperatures (within $\sim 5 \text{ mK}$), heating the detector with the higher transition temperature can heat the other detector out of its transition. In the measurements with the prototype of the small module it was observed, that the thermal coupling between the detectors is too strong to operate all four detectors (phonon detector + three iSticks) with a separated heater. A separated heater on the iSticks can heat the phonon detector out of its transition and vice versa.

As for the phonon detector an optimal signal-to-noise ratio is desired, also for this detector a separated heater is necessary as it reduces the noise. For this reason, the heating scheme of the iStick TES must be adapted. For the iSticks a heater providing a strong thermal coupling to the tungsten film without creating an electrical contact was designed. The heater film is produced on a layer of silicon (blue in figure 6.3b), which is sputtered on the tungsten film (dark gray in figure 6.3b). At low temperatures this layer is electrically insulating. It is not possible to bond directly on this thin film since the isolation layer can break due to the applied pressure. In this case an electrical contact between the bond pads and the tungsten film can appear. Therefore, the heater is contacted over thin aluminum lines (light gray in figure 6.3b) connecting the heater film (yellow) and the bond pads placed directly on the substrate. To prevent an electrical contact between these lines and the tungsten film, the silicon layer extends the tungsten film. With such a heater it is possible to operate the phonon detector as well as the iSticks at the same time.

An opened module mounted with three iSticks is shown in figure 6.3c. The crystal in the middle is only held by the three iSticks pressed against it with bronze clamps

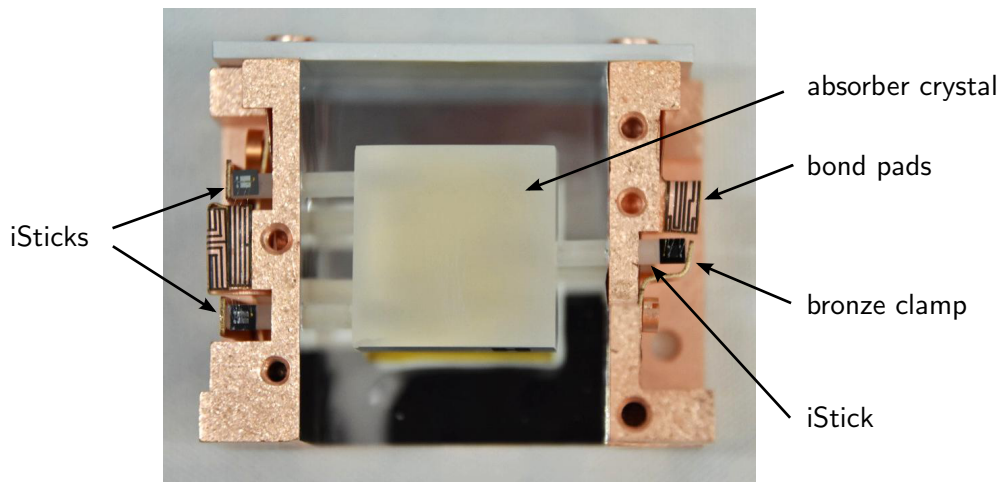
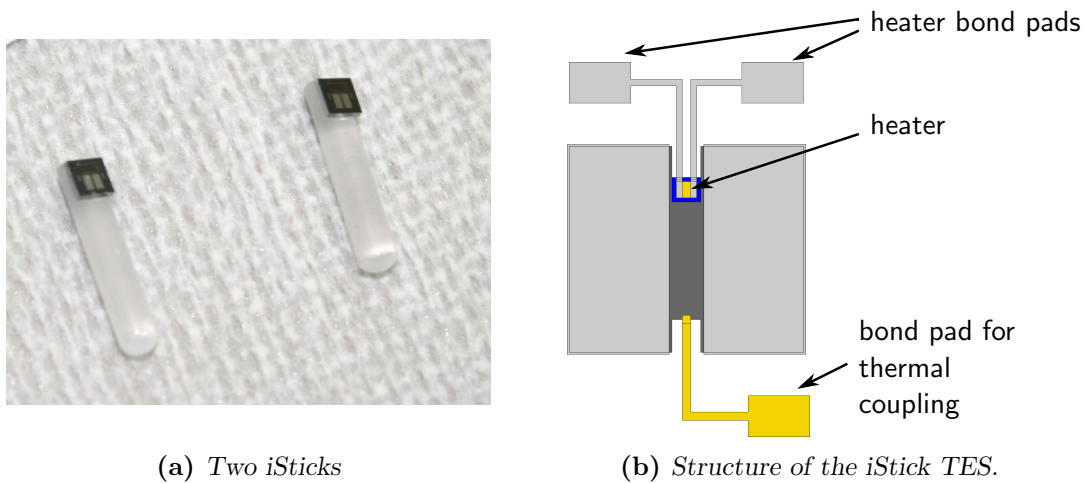


Figure 6.3: Realization of the iSticks consisting of a CaWO_4 stick and a silicon carrier with a TES glued to the latter is depicted in (a). A schematic drawing of the iStick TES is shown in (b). The tungsten film is depicted in dark gray, all aluminum parts in light gray and the parts made of gold in yellow. To strongly couple the thermometer heater to the tungsten film of the TES, it is placed on top of a sputtered silicon layer (blue). The bond pads for the heater are located next to the TES and are connected via lines of aluminum (light grey). In (c) a photograph of an opened detector module with the crystal in the middle which is only held by the three iSticks (left and right) is shown. The latter are pressed against the crystal with bronze clamps from outside the housing.

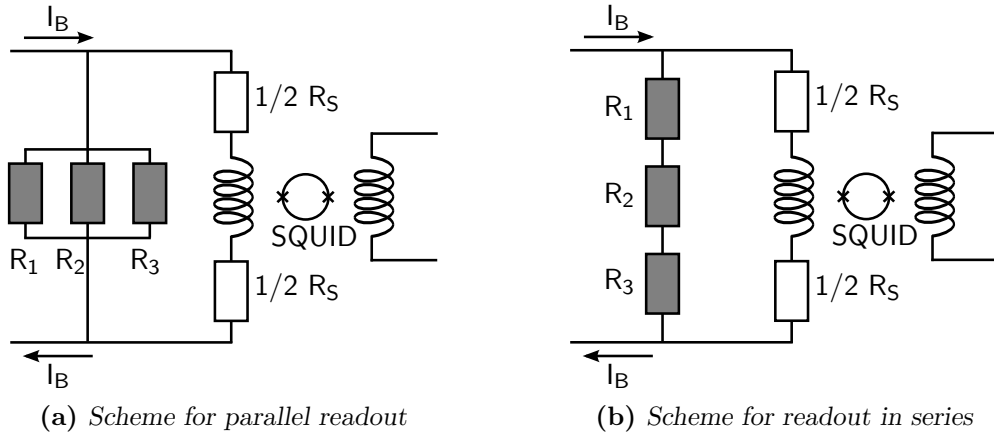


Figure 6.4: Readout circuits used for the readout of three iSticks with one SQUID. Similar to the standard readout of CRESST detectors one branch contains the SQUID and the shunt resistances while the other contains the thermometers. The three thermometers of the iSticks can be operated either in parallel (a) or in series (b). The operation in a parallel readout circuit is more stable compared to an operation the readout circuit in series. For details see text.

located outside the housing. The three iSticks with their silicon carriers and TES are visible right and left of the crystal. Next to carriers the bond pads used to contact the thermometers can be seen.

6.3.2 Readout Scheme

The number of readout channels in the present CRESST setup is limited to 37¹. Up to now, typically each module required two readout channels, one for the phonon detector and one for the light detector. Therefore, in CRESST-II phase 2 a total of 18 modules were operated. The new small module design features three additional thermometers for the iSticks. If each of them utilizes a separate channel each module requires five readout channels and, thus, in total only seven modules could be operated.

As discussed, for the iStick channel a moderate energy threshold of $\mathcal{O}(1 \text{ keV})$ is necessary. Although this might reduce the performance of the veto channel it is possible to read out all iSticks of one module with one SQUID and still meet these requirements. In order to read out the three iStick TES with one SQUID they can be connected either in a series or in a parallel circuit. The readout schemes for both modes are shown in figure 6.4. As in the standard readout scheme of CRESST detectors (see figure 2.11) the readout circuits consists of two branches. In one branch the SQUID and the shunt resistances are connected and in the other the detectors.

In both readout schemes, the three detectors influence each other due to electrothermal feedback. A change of the resistance of one thermometer causes a change of the current through the other two thermometers. During operation a single detector can increase its resistance due to a heat input. When operating the three detectors in parallel (figure 6.4a) an increase of the resistance in one of them, reduces the bias current

¹The CRESST setup is constructed for 66 readout channels. However, only 37 of them are currently fully functional.

through the branch of this thermometer, while in the other branches the bias current increases accordingly. An increase of the bias current leads to a temperature rise and, thus, increases the resistance of the thermometer. Vice versa a reduction of the bias current reduces the resistance. Therefore, in the parallel readout circuit the change of current through the branches acts against the change of resistance and this results in a stabilization of the thermometers.

In contrast, when operating the three detectors in series (figure 6.4b), an increase of resistance in one thermometer reduces the bias current through all three thermometers. Thereby, the resistance of all three thermometers is reduced. In this case the three thermometers can only go back to their operating point with a heat input from the thermometer heater but not by themselves.

During the development of the small module, iSticks were operated in both readout modes and as expected an operation in parallel proved to be more stable. Motivated by this in [102] the stability due to thermal feedback effects is studied theoretically and estimated quantitatively. It is as well concluded that a parallel readout scheme can be operated more stable which agrees with the observations.

Chapter 7

First Measurements with a Prototype Module

Within the present work a prototype of the detector module optimized for low-mass dark matter search (see chapter 5 and 6) was produced and measured in a test setup in Munich. The aim is to verify that all requirements for the detector performance as well as the new holding scheme are met. The main goal is to determine if an energy threshold of $\lesssim 100$ eV is achievable with the suggested phonon detector design. Also the performance of the iStick channel is investigated. Only after the confirmation of all demands it is reasonable to install these modules in the main CRESST setup.

The measurements have been performed in a cryostat above ground, where a higher rate and a noise contribution larger than in the CRESST setup degrade the measurement conditions (section 7.1). Still, it has been possible to successfully operate all three channels of the module and to calibrate them. The performance of the phonon detector is explored in section 7.2, while the results of the light detector are presented in section 7.3. The iStick channel and its ability to veto events occurring in the sticks is investigated in section 7.4.

7.1 Measurements and Data Analysis

In order to study and optimize the performance of the small detector module and the design of the detector holder a series of measurements has been performed in a dilution refrigerator (cryostat 1) at Max-Planck-Institute for Physics in Munich. In the present work measurements of two different phonon detectors in a complete prototype detector module are discussed. The crystals were produced by the crystal laboratory of TUM [82]. Within the present work each was equipped with a calorimetric TES of a different design. The performance of these two phonon detectors is investigated in two separate measurement campaigns (called runs hereafter¹) presented in the following in detail:

Run 126 The phonon detector TUM26-b was operated together with the light detector WI-531/2 and three iSticks connected in parallel with a live time of 30.24 h (after application of the stability cut). The calorimetric TES of the phonon detectors has a total area of $A_t = 36 \text{ mm}^2$ with the dimensions as shown in figure 5.2a.

Run 127 For this measurement the phonon detector was exchanged. The detector TUM56-f was operated in the same detector holder and with the same light de-

¹The runs are labeled according to the number of the measurements performed with the respective cryostat.

detector as well as the same iSticks. This detector is equipped with a TES structure covering an area of $A_t = 19 \text{ mm}^2$ with the dimensions as shown in 5.2b. The live time in this measurement is 46.56 h (after application of the stability cut).

The signal level for a certain energy depends on the chosen operating point in the transition and on the bias current. The signal is proportional to the bias current as well as the transition slope [66, 110]. Moreover, a larger bias current leads to a reduction of transition slope and, thus, during the detector setup the best compromise for the largest signal is chosen. In both measurements the detectors were optimized in terms of signal level².

The SQUIDs used for the measurements can output a maximum amplitude of $\sim 10 \text{ V}$. To readout larger pulses it can be operated in a less sensitive range. As the phonon detectors as well as the iSticks measured here exhibited a large signal, it was necessary to operate them in a less sensitive range compared to other detectors (e.g. most detectors operated in CRESST-II phase 2). Within the present work all amplitudes are scaled to the same range for better comparison .

Due to the high rate observed during the measurements the threshold of the hardware trigger was set at a higher energy than the actual energy threshold of the detector to allow for a stable operation³. As explained before with stable noise conditions, the best achievable threshold is the 5σ baseline noise. The latter is determined from empty baselines, i.e. records triggered randomly by the DAQ (see section 4.3).

The basic concepts of the data analysis are explained in section 2.5. In contrast to the measurements in the main CRESST setup, in the measurements presented here ^{55}Fe sources were used for the calibration. ^{55}Fe decays via electron capture to ^{55}Mn and, thereby, produces lines at energies of 5.9 keV and 6.5 keV [121]. At these energies the detectors operated are still in the linear region of the transition. In the test measurements one ^{55}Fe source causing a rate of $\sim 5 \text{ Hz}$ was placed inside the scintillating housing in line-of-sight to the phonon detector. Additionally, outside the housing three sources each in line-of-sight with one iStick were installed.

7.2 Phonon Detector Performance

The focus of the optimization of the detector module for CRESST-III is on the reduction of the energy threshold of the phonon detector. The crystal as well as the TES structure are optimized to increase the signal height (see chapter 5). In the following the performance of the phonon detectors is investigated in detail with the results from the two measurements performed in the test setup. All parameters derived for the two phonon detectors TUM26-b and TUM56-f are summarized in table 7.2 at the end of the present section.

²The detectors are aimed to be optimized for the best signal-to-noise level. However, the noise did not change significantly throughout the transition and, thus, was assumed to be constant.

³Control pulses, necessary for the stabilization, are only sent when the detector did not trigger for a certain time range. If the trigger threshold is set too low there is not enough time between two triggers to send control pulses. Thus, it is not possible to stabilize the respective detector reliable.

7.2.1 Calorimetric Detector Operation

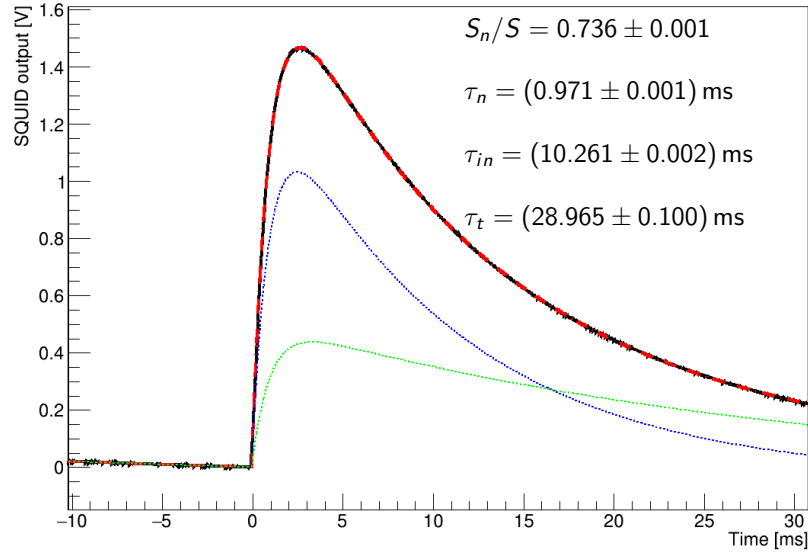
Both small crystals were equipped with a TES structure optimized for a calorimetric operation. The two structures have a similar geometry, however, the area covered differs by a factor of ~ 2 .

Due to the change of the crystal geometry as well as the TES structure, the time constants describing the pulse shape are expected to be different compared to the other thermometers formerly used in CRESST-II (see section 5.1). Template pulses describe the pulse shape with a reduced influence of the noise (see section 2.5). For the creation of the templates shown here pulses of the ^{55}Fe source with an energy of 5.9 keV are used. In figure 7.1 the template pulses of both detectors investigated, TUM26-b (a) and TUM56-f (b), are depicted in black. Also drawn in red is a fit of the pulse model for the calorimetric operation mode to the respective pulse (see equation 4.22). The non-thermal and the thermal component of the pulse model are depicted as blue-dashed and green-dashed lines, respectively. For both detectors the observed pulse shape is described very well by the pulse model of a calorimetric detector. The errors given on the fit parameters are statistical errors (1σ).

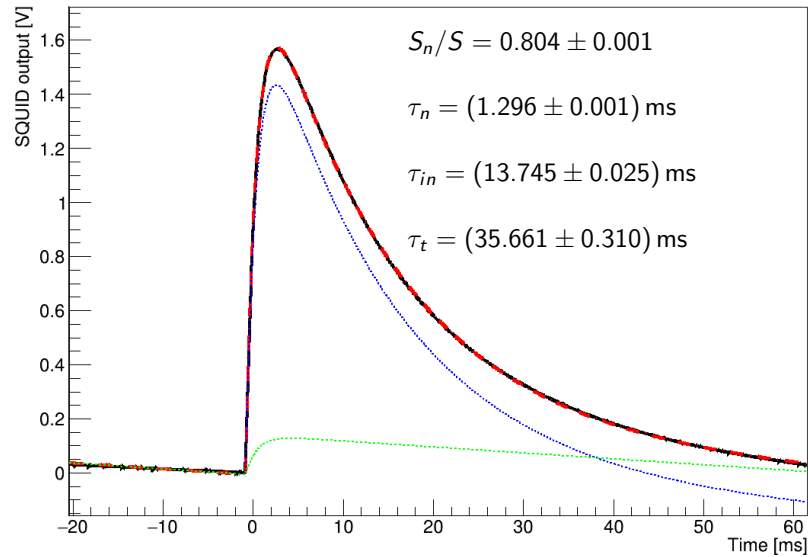
The high trigger rate observed in the test setup causes plenty of pile-up events. To reduce the number of records with more than one pulse the record time is decreased. However, the recording window should be long enough to capture the complete pulse shape. Thus, in both measurements a compromise between these two demands was chosen. Therefore, a time window of 40.94 ms in run 126 and of 81.88 ms in run 127 is recorded. As can be observed in figure 7.1 the template pulses, which describe the averaged pulse shape, are not completely relaxed back to the baseline level present before the pulse at the end of the record window. This reduces the quality of the pulse-model fit especially for the thermal component and increases the error on this component.

From the pulse-model fit the following results are obtained:

- The fraction of the non-thermal component of the total pulse amplitude $S_n/S = S_n/(|S_n| + |S_t|)$ dominates for both detectors. Values of $S_n/S = (73.6 \pm 0.1)\%$ for TUM26-b and $S_n/S = (80.4 \pm 0.1)\%$ for TUM56-f are obtained in the fit. These values are similar to the values observed for CRESST-II detectors of typically $\sim 80\%$ (see section 4.2).
- For the rise-time of both components, which is equivalent to the life-time of non-thermal phonons, values of $\tau_n = (0.971 \pm 0.001)$ ms in TUM26-b and $\tau_n = (1.296 \pm 0.001)$ ms in TUM56-f are determined. Compared to the phonon detectors operated in CRESST-II (see an exemplary pulse in figure 4.5) the life-time of non-thermal phonons τ_n is shorter by a factor of > 10 . The thermalization of non-thermal phonons is discussed later in section 7.2.3.
- The thermal relaxation time of the thermometer τ_{in} is determined by the pulse model fit to be $\tau_{in} = (10.261 \pm 0.002)$ ms in TUM26-b and $\tau_{in} = (13.745 \pm 0.025)$ ms in TUM56-f. Compared to the phonon detectors operated in CRESST-II this time constant is longer by a factor of ~ 4 . It is ~ 2 times longer than in the light detectors operated in CRESST-II. This agrees well with the expectations from the thermal coupling of the thermometers to the heat bath.



(a) Template pulse of the 5.9 keV line in TUM26-b.



(b) Template pulse of the 5.9 keV line in TUM56-f.

Figure 7.1: Template pulses (black) created from pulses of the 5.9 keV line for the two phonon detectors TUM26-b (a) and TUM56-f (b). Both detectors feature a small CaWO_4 crystal ($20 \times 20 \times 10 \text{ mm}^3$) as absorber and are operated in a prototype holder for the new small module design. The crystals are equipped with different thermometer structures. The area of the thermometer is smaller by a factor of two on the detector TUM56-f compared to the TES of TUM26-b. A fit of the pulse model (according to equation 4.22) to the templates is shown as red-dashed line. The non-thermal component is depicted in blue while the thermal component in green. The fit values are as well given. Note that the record window was different in both measurements.

- Slight differences between both detectors are observed in the thermal relaxation time of the absorber $\tau_t \approx C_a/G_{ab}$ (see equation 4.27). As already explained, due to the relative short record window there are relatively large uncertainties in the values determined from the fit. A value of $\tau_t = (28.965 \pm 0.100)$ ms (TUM26-b) and $\tau_t = (35.661 \pm 0.310)$ ms (TUM56-f) are obtained from the pulse model fit. The different values can be explained by a difference in the strength of the thermal coupling between the absorber and the heat bath G_{ab} . This coupling is determined by the holding scheme of the crystal which is realized by three CaWO_4 stick pressed against the crystal by bronze holding clamps (see section 6.2). Each of these clamps can be tightened individually and differences in the pressure influence the thermal coupling G_{ab} .

As required for a calorimetric thermometer the life-time of non-thermal phonons τ_n (the rise time of both pulse components) is much shorter than the thermal relaxation time of the thermometer τ_{in} (the decay time of the non-thermal component) ($\tau_n \ll \tau_{in}$). Moreover, the amplitude of the non-thermal component is much larger than the thermal component. Also the decay time of the thermal component τ_t is not too long for an operation in the CRESST setup. While in the measurement above ground a short record window had to be selected, in the CRESST setup a longer record window (327.62 ms in CRESST-II) is chosen as the rate is drastically lower (by a factor of ~ 100) in the underground setup. Hence, the detectors work as desired and the requirements for a detector operated in the calorimetric mode are fulfilled.

7.2.2 Energy Threshold

In order to achieve an energy threshold of 100 eV or below the increase of the signal height without a change the noise has been the main goal for the new small phonon detector. To determine the enhancement of the signal height, pulses of the ^{55}Mn peaks induced by the ^{55}Fe sources are investigated.

The high overall event rate leads to a degradation of the energy resolution due to a unstable operating point and the non-linearity of the transition. Moreover, it results in many records with non-flat baselines and, thus, reduces the quality of the template fit. Strong cuts on the RMS of the template fit were applied to remove such distorted events. The resulting amplitude spectra in the energy region around the ^{55}Mn peaks are shown in figure 7.2 for both detectors. A resolution of $\sigma = (134.4 \pm 1.2)$ eV and $\sigma = (125.1 \pm 1.8)$ eV at an energy of 5.9 keV is determined for TUM26-b and TUM56-f, respectively. With this resolution the K_α and K_β line of ^{55}Mn can be separated. The pulse amplitude of the 5.9 keV line is determined to be $\Delta U = 1.34$ V and $\Delta U = 1.49$ V for TUM26-b and TUM56-f, respectively.

For Lise, the phonon detector with the lowest energy threshold in CRESST-II phase 2, the amplitude of the 5.9 keV line⁴ is determined to be $\Delta U = 0.09$ V. Thus, the signal level for the two small phonon detector measured here is increased by a factor of ~ 15 and ~ 17 , respectively. This is also visible in figure 7.3 where two pulses with an energy

⁴In CRESST-II phase 2 ^{55}Fe sources were used for an absolute energy calibration of several light detectors. Normally, these sources are mounted so that they cannot be seen by the phonon detectors. The phonon detector Lise was accidentally irradiated with such a source [74].

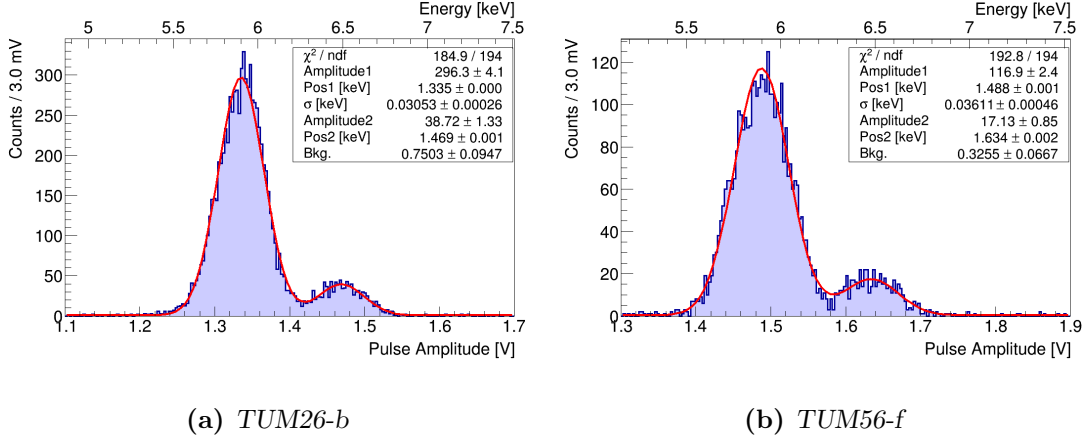


Figure 7.2: Amplitude spectrum of particle pulses around the peaks resulting from the ^{55}Fe source in the phonon detectors TUM26-b (a) and TUM56-f (b). The two peaks due to the ^{55}Mn can be clearly identified. Both detectors can resolve the two X-ray lines of ^{55}Mn at 5.9 keV and 6.5 keV. A fit of two Gaussian functions plus a constant background to the spectrum is shown in red.

of 5.9 keV of the detector TUM56-f (black) and the detector Lise (red) are compared. The pulse of Lise was measured in the CRESST setup at Gran Sasso, while the pulse of TUM56-f was measured in cryostat 1 at MPI Munich.

The baseline noise of both prototype detectors operated in Munich is determined to be $\sigma_{P,0} = (6.75 \pm 0.12)$ mV (TUM26-b) and $\sigma_{P,0} = (9.71 \pm 0.28)$ mV (TUM56-f) (see appendix A). This corresponds to $\sigma_{P,0}^E = (27.21 \pm 0.47)$ eV and $\sigma_{P,0}^E = (39.06 \pm 1.11)$ eV for TUM26-b and TUM56-f, respectively. With this baseline noise an energy threshold of $E_{thr} = 136.05$ eV and $E_{thr} = 195.3$ eV, respectively, is achievable with these detectors in the test setup in Munich.

In the CRESST main setup noise levels of 0.7–3.0 mV have been achieved (see section 4.3). Assuming the noise level of the CRESST setup and the signal level measured with TUM26-b and TUM56-f thresholds in the range of 16 – 60 eV are in reach for CRESST-III detectors. This is well below the aimed goal of a 100 eV threshold and, thus, it is feasible to meet or even outreach the design goal of CRESST-III.

7.2.3 Thermalization of Non-Thermal Phonons

In order to further optimize the detectors in the future it is necessary to understand the process of the thermalization of non-thermal phonons in the crystal. As discussed in section 4.2.5, two processes are competing - the thermalization in the absorber (described by the time constant $\tau_{crystal}$) and the thermalization due to absorption in the thermometer film (described by the time constant τ_{film}). These two time constants cannot be measured directly. Instead only the total life time of non-thermal phonons τ_n , which is the rise time of both components in a calorimetric thermometer, can be determined from measured pulses via the pulse model fit. As a reminder, the time constants for thermalization determine the life-time of non-thermal phonons in the following way

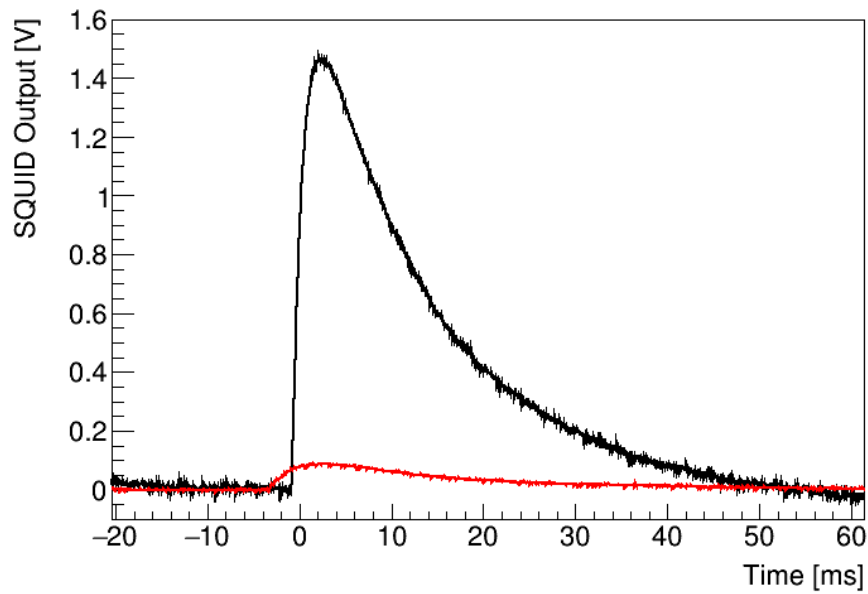


Figure 7.3: The black pulse with a deposited energy of 5.9 keV ($^{55}\text{Mn } K_{\alpha}$) is measured with the detector TUM56-f in cryostat 1 in Munich. It is compared to a 5.9 keV pulse measured in the CRESST setup with the detector Lise, the phonon detector with the lowest energy threshold in CRESST-II phase 2 (red). The amplitude of the pulse of TUM56-f is larger by a factor of ~ 17 compared to the amplitude of the pulse of Lise. This illustrates the improvement of the optimized CRESST-III phonon detector.

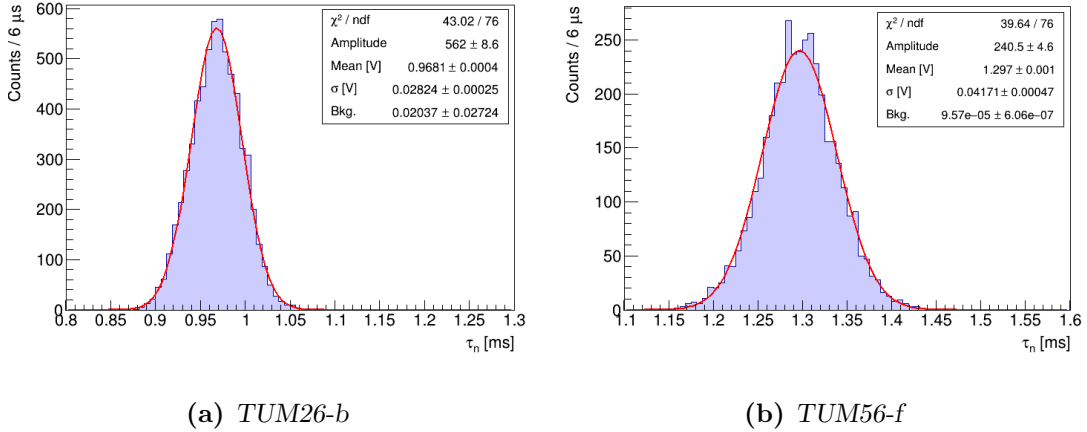


Figure 7.4: Distribution of the life-time of non-thermal phonons τ_n from a parametric fit to a set of pulses of the phonon detectors TUM26-b (a) and TUM56-f (b). The resulting distribution of τ_n is fitted with a Gaussian function (red) to determine the mean. The values obtained for τ_n are in agreement to the values determined from the fit of the pulse model to the template pulse (see figure 7.1).

(see section 4.2):

$$\frac{1}{\tau_n} = \frac{1}{\tau_{film}} + \frac{1}{\tau_{crystal}} \quad (7.1)$$

To derive the parameters of the thermalization an exact knowledge of τ_n is required. However, the value of τ_n which is determined from a fit of the pulse model to the template pulse (see figure 7.1) might be distorted as many pulses are summed for the creation of the template pulse. Thus, the pulse model was individually fitted to a set of pulses in the linear range of the respective detector. From these individual fits, the mean for τ_n is determined by a fit of a Gaussian function to the obtained distribution (see figure 7.4). Values of $\tau_n = 0.97$ ms for TUM26-b and $\tau_n = 1.30$ ms for TUM56-f are determined. They agree within 2% with the ones determined from the fit of the template pulse. Hence, the error due to the creation of the template is negligible.

The two detectors TUM26-b and TUM56-f both have a crystal of the same size. For this reason, it is expected that the thermalization in the crystal has the same time constant $\tau_{crystal}$ (see equation 4.16). The area of the thermometer differs by a factor of ~ 2 . As the time constant for the thermalization in the film τ_{film} inversely scales with the thermometer area A_t (see equation 4.17), it is expected to be smaller by a factor of two for the detector with a larger TES (TUM26-b) than for the one with the smaller TES (TUM56-f). In total also the life-time of non-thermal phonons τ_n is expected to be smaller for the detector with the large TES structure. However, the difference of the value depends on the relation of τ_{film} and $\tau_{crystal}$ (see equation 7.1). For the two detectors measured, as expected the value of τ_n is smaller for TUM26-b by a factor of ~ 1.3 .

In order to determine the thermalization time constants τ_{in} and $\tau_{crystal}$ two different methods are performed and explained in the following.

Method 1: Direct calculation of τ_{film} With the first method all time constants are determined individually for each detector. As discussed in section 4.2.5 the time

detector A_t [mm ²]	TUM26-b		TUM56-f	
	Method 1	Method 2	Method 1	Method 2
τ_n [ms]	0.9681		1.297	
τ_{film} [ms]	2.410	2.017	4.683	4.034
$\tau_{crystal}$ [ms]	1.603	1.843	1.734	1.843
ε [%]	40.0	47.7	27.0	31.3

Table 7.1: Time constants determined with two different methods for the detectors TUM26-b and TUM56-f. Method 1 relies on the direct calculation of the time constant τ_{film} . In method 2 two different phonon detectors with crystals of the same size and differently sized TES structures are compared. The time constant τ_n is determined from the fit of the pulse model to pulses in the linear range. For details see text.

constant for the thermalization in the thermometer film τ_{film} can be calculated directly according to equation 4.17. However, this relies on the assumption that longitudinal non-thermal phonons are completely absorbed in the tungsten film, while transverse phonons do not interact at all. In [93] it is shown that this is a good assumption for the transmission of non-thermal phonons from silicon to an iridium/gold film. However, up to now this has not been confirmed for the transmission from CaWO₄ into a tungsten film.

With the calculated values of τ_{film} and the values for the life-time of non-thermal phonons τ_n , the time constant $\tau_{crystal}$ can be determined with equation 7.1. All resulting values are shown in table 7.1 for both detectors as method 1. With this method for the time constant τ_{film} values of 2.4 ms (for TUM26-b) and 4.6 ms (for TUM56-f) are determined. Values of $\tau_{crystal} = 1.6$ ms for TUM26-b and $\tau_{crystal} = 1.7$ ms for TUM56-f are derived. As the two values agree well, this hints that the assumption for the absorption probability of non-thermal phonons in the tungsten film is valid. This corresponds to a fraction of non-thermal phonons absorbed in the thermometer of $\varepsilon = 40.0\%$ for TUM26-b and $\varepsilon = 37.0\%$ for TUM56-f.

As method 1 relies on certain assumptions, which might not be fulfilled for the investigated detectors a second method is performed.

Method 2: Comparison of two crystals In contrast to the first method, the second method needs inputs from both measurements and compares them. It exploits the relations of the time constants τ_{film} and $\tau_{crystal}$ expected from the geometry of the crystals and the thermometers. As mentioned above, τ_{film} is expected to be twice as long in the detector TUM56-f with the smaller thermometer compared to TUM26-b. Additionally, $\tau_{crystal}$ is expected to be the same in both detectors.

Combining this, the two time constants (τ_{film} and $\tau_{crystal}$) can be determined with equation 7.1 from the life time of non-thermal phonons τ_n of both measurements. The resulting values are also shown in table 7.1. A value of $\tau_{crystal} = 1.8$ ms is determined for both crystals. For the time constant τ_{film} a value of 2.0 ms for TUM26-b and a value of 4.0 ms for TUM56-f are resulting. This corresponds to a

fraction of non-thermal phonons absorbed in the thermometer of $\varepsilon = 47.7\%$ for TUM26-b and $\varepsilon = 31.3\%$ for TUM26-a.

The values for the time constants determined with both methods differ by $\sim 10\text{-}20\%$ but are roughly consistent. This is an indication that the assumptions made for the direct calculation of the time constant τ_{film} are valid for the transmission of non-thermal phonons into a tungsten film.

One uncertainty which influences both methods in the same way is the usage of phonon collectors in the thermometer structures described here. The energy transport through the phonon collectors might be delayed compared to the absorption of non-thermal phonons directly in the tungsten film and, thus, might influence the rise time of the pulse. In [106] the time constant for this process was found to be $\mathcal{O}(10\ \mu\text{s})$ (for an aluminum film with a length of 4 mm) and, thus, short compared to the pulse rise time. Moreover, this uncertainty affects both methods in the same way. The absolute values can be distorted due to these uncertainties but it is valid to compare them. To investigate the parameters in a further measurement the usage of thermometers without phonon collectors would be beneficial.

The model for the time constants τ_{film} and $\tau_{crystal}$ allows to calculate the expected time constants for the large crystals operated in CRESST-II phase 2. The time constant τ_{film} can be directly calculated. According to equation 4.17 it is $\tau_{film} \approx 23\ \text{ms}$. From the known relation of $\tau_{crystal} \propto V_a/A_a$ and the values of the time constant determined for the small crystal, a value of $\tau_{crystal} \approx 5\ \text{ms}$ is expected for the large crystals. With these values, a life-time of non-thermal phonons of $\tau_n = 4.1\ \text{ms}$ is expected (see equation 7.1).

However, CRESST-II phonon detectors with a bolometric TES evaporated directly on the large crystal feature a life time of non-thermal phonons of $\tau_n \approx 12\ \text{ms}$. Due to equation 7.1 τ_n must always be shorter than each of τ_{film} and $\tau_{crystal}$. Thus, the expected value for τ_{film} of 23 ms fits well to the measured value of τ_n . However, the expected value for $\tau_{crystal} \approx 5\ \text{ms}$ is too small.

There are several possible explanations for this discrepancy:

- The crystal surface might influence the thermalization of non-thermal phonons in the crystal and, thus, the value of $\tau_{crystal}$. While on the large crystals operated in CRESST-II usually only one side is roughened and the other sides are polished, on the small crystal five sides are roughened. A dedicated measurement with crystals of the same geometry with differently treated surfaces could investigate this influence.
- As mentioned above, the influence of the phonon collectors increases the uncertainty of the method. As the bolometric TES of the large crystal does not feature phonon collectors, it might not be valid to transfer the time constants.
- The expected dependence of $\tau_{crystal}$ on the absorber volume V_a and the absorber area A_a (see equation 4.16) might not be valid. The thermalization of non-thermal phonons in the crystal could to be influenced by additional effects. For example the geometry of the crystal plays a role as it influences the mean scattering length of non-thermal phonons in the crystal. This is investigated further in [102] but the determined results cannot explain the discrepancies found here.

7.2.4 Thermometer Area

From the two time constants describing the thermalization, τ_{film} and $\tau_{crystal}$, the fraction of non-thermal phonons absorbed by the thermometer ε was calculated for both thermometer structures with equation 4.18 (see table 7.1). The signal level of the non-thermal component S_n is proportional to ε/C_e , where C_e is the heat capacity of the thermometer (see section 4.2). Thus, from the values determined for ε (see table 7.1) it is expected that the signal level of TUM56-f (small thermometer structure) is larger by $\sim 33\%$ compared to TUM26-b (large thermometer structure).

For the 5.9 keV line a voltage amplitude of 1.34 V for TUM26-b and 1.56 V for TUM56-f was measured, respectively. Thus, the voltage signal of TUM56-f is larger by 16% compared the voltage signal measured with TUM26-b. For a conversion of the voltage signal in the temperature signal additional measurements are necessary, as the high rate observed in the test setup did not allow an exact measurement of the transition slope. However, as both TES structures only differ in size, the difference in signal height is expected to be caused by the TES area. Thus, this measurement hints that a smaller thermometer area increases the signal.

It should be noted, that also the area of the phonon collectors differs by a factor of two for the two TES structures, just as the area of the tungsten film. As long as the phonon collectors are efficient over the whole area, they lead to the same signal increase in both structures. In [107] the diffusion length of the quasi particles was determined to be $\mathcal{O}(1\text{ mm})$. The phonon collectors of the large structure on TUM26-b have a maximum distance to the tungsten film of $\sim 3\text{ mm}$. If the diffusion length is smaller than this distance, part of the signal might be lost and a smaller temperature rise might be measured. Further measurements are necessary to determine the diffusion length more precisely or to measure the influence of the size reduction of the tungsten film and the phonon collectors separately.

For CRESST-III phase 1 in total ten of the optimized phonon detectors have been mounted. Both thermometer structures for the phonon detector investigated in the present work are exploited. Seven phonon detectors are equipped with the larger TES structure (see figure 5.2a) including TUM26-b, while three are equipped with the smaller TES structure (see figure 5.2b). With data from more detectors, the difference in the signal level obtained with the two structures can be investigated in detail. If it is confirmed that the size reduction increases the signal level, it might even be worth to investigate a further reduction of the TES size for future detectors.

7.3 Light Detector Performance

Besides the phonon detector also the light detector has been changed in the optimized module. An enhanced light output of the CaWO_4 crystal together with a change of the light detector geometry are expected to increase the signal level in the light detector by a factor of $\sim 6 - 7$ (see section 5.3). The same light detector, named WI-531/2, was operated in both runs. As it performed similar in both, in the following only data obtained in run 126 is discussed.

Also the light detector was affected by the high rate and the high noise contribution in the test setup. It was not directly calibrated with a separate source, as this would

crystal		TUM26-b	TUM56-f
measurement		Run 126	Run 127
live time after stability cut [h]		30.24	46.56
W film evaporation number		WI-540/2	WI-549/2
total thermometer area	A_t [mm ²]	36.08	18.57
bias current	I_B [μ A]	22	13
normal conducting resistance	R_n [m Ω]	143 ± 1	131 ± 1
resistance at operating point	R_T [m Ω]	57.8 ± 1.2	57.0 ± 1.7
amplitude 5.9 keV	ΔU [V]	1.34	1.56
resolution at 5.9 keV	σ [mV]	30.52 ± 0.03	36.08 ± 0.05
	σ^E [eV]	134.4 ± 1.2	125.1 ± 1.8
baseline noise	$\sigma_{P,0}$ [mV]	6.75 ± 0.12	9.71 ± 0.28
	$\sigma_{P,0}^E$ [eV]	27.21 ± 0.47	39.06 ± 1.11
pulse shape parameters	S_n/S	0.736 ± 0.001	0.804 ± 0.001
	τ_n [ms]	0.971 ± 0.001	1.296 ± 0.001
	τ_{in} [ms]	10.261 ± 0.002	13.745 ± 0.025
	τ_t [ms]	28.965 ± 0.100	35.661 ± 0.310

Table 7.2: Parameter including statistical errors of the detectors TUM26-b and TUM56-f measured in run 126 and run 127, respectively. The pulse shape parameters are determined from the fit of the pulse model to the template pulse of the 5.9 keV line as shown in figure 7.1.

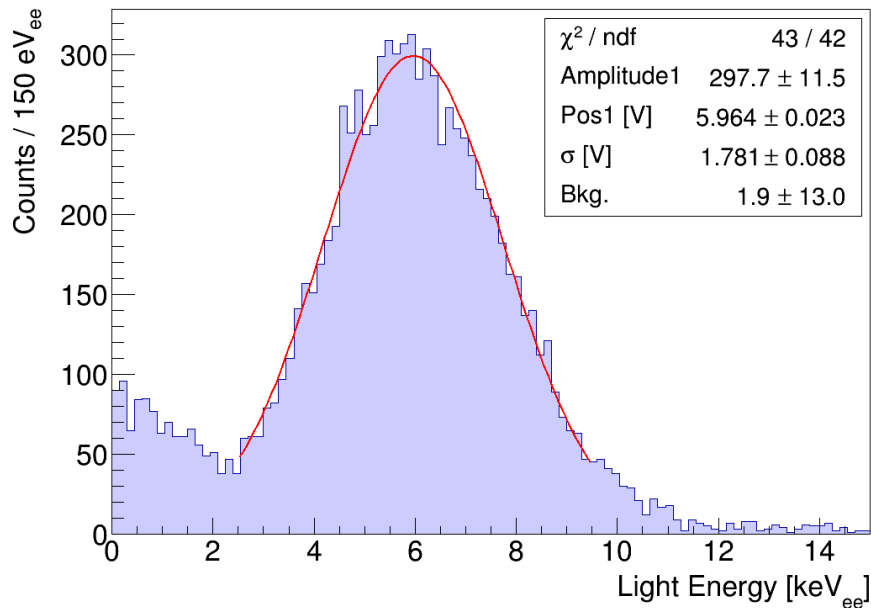


Figure 7.5: Spectrum of particle pulses in the light detector WI-531/2 measured in run 126. The resolution is not good enough to separate the K_α and K_β peak of ^{55}Mn and, thus, the spectrum was fitted with one Gaussian function (red line).

have increased its rate further. Instead, the light detector is calibrated with scintillation events from the ^{55}Fe source hitting the crystal, as it is done within the CRESST experiment. Thus, the determined energy is given in units of keV_{ee} considering that the calibration is performed with γ -rays inducing electron recoils in the crystal.

The spectrum measured with the light detector in run 126 is shown in figure 7.5. As the resolution is not good enough to separate the K_α and K_β lines of ^{55}Mn the spectrum is fitted with one Gaussian function. The fit yields a resolution of $\sigma = (1.78 \pm 0.09) \text{keV}_{ee}$ at 5.9keV_{ee} . A baseline noise slightly higher than in the phonon detector of $\sigma_{L,0} = (8.64 \pm 0.17) \text{mV}$ was achieved (see appendix A). Due to the low fraction of energy transformed into scintillation light this corresponds to $\sigma_{L,0}^E = (838.42 \pm 16.51) \text{eV}_{ee}$. With the baseline noise measured in the CRESST setup the resolution would correspond to a noise contribution of $(100\text{--}300) \text{eV}_{ee}$, which is similar to the light detectors operated in CRESST-II phase 2.

The improvements expected for the light detectors with the changed absorber geometry cannot be confirmed with this measurement. However, as only one light detector was measured within the present work and the range in the performance of light detectors has always been large, more measurements are necessary to evaluate the average performance of these light detectors. Moreover, the light detector performance does not affect the sensitivity to low-mass dark matter strongly (see chapter 3). Nevertheless, a dedicated study should be performed with data from CRESST-III for a better understanding of the new light detectors.

7.4 iStick Channel

In the small module design the phonon detector is held by three scintillating CaWO_4 sticks. Together with the scintillating and reflective foil they provide a fully-scintillating housing. The latter allows to reject nuclear recoils from a possible α -contamination on any inner surface of the module. However, α -events on the stick surface outside the housing can cause nuclear recoils in the sticks without a light signal from the α -particle. Due to an energy transfer via the stick-crystal interface they can cause low energetic events in the ROI. To be able to veto such events each stick is instrumented with a TES (see section 6.3).

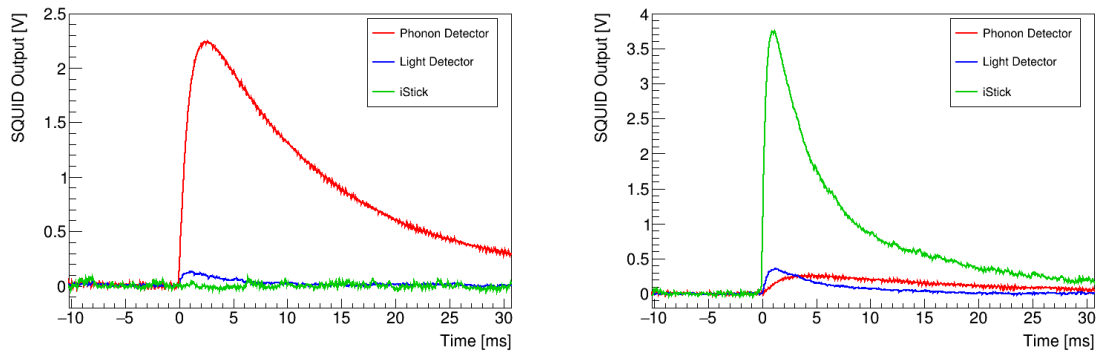
The three iStick thermometers of each module are connected in parallel to one readout channel. Thus, the operation of instrumented holding sticks requires only one additional readout channel per module. With the operation of three iSticks in one channel, for the first time more than one detector was operated in one readout channel within the CRESST experiment.

A reduction of the performance of the individual detectors is expected as three detectors are contributing to the noise. However, the performance of the channel must be good enough to veto all events occurring in the sticks and producing a measurable signal in the phonon detector. As the identical iSticks were operated in both measurements, the performance of the iStick channel was similar in both measurements. Thus, this channel is investigated only with data of run 126 in the following.

7.4.1 Setup of the iStick Channel

During the setup of a detector the bias current and the operating point within the transition are chosen to obtain the largest signal. In the iStick channel three detectors have to be optimized during the setup. Due to the readout scheme with the three iSticks operated in parallel (see figure 6.4a) a variation of the readout current influences all three detectors. Moreover, the change of the operating point, i.e. of the resistance of one detector also affects the readout current through all three detectors. Due to the stabilizing properties of the parallel readout circuit (see section 6.3.2) a simplified procedure can be applied for the setup of the iStick channel. Instead of adjusting each TES individually, it is possible to heat all TES into transition by applying a high bias current to the channel. The TES with the lowest resistance automatically obtains the highest bias current due to the splitting of the current in the parallel circuit. With a variation of the heater current of each TES, it is possible to find the best operating point for each TES.

Moreover, during the setup of the iStick channel it has to be considered that the sticks and the phonon detector can influence each other as well. A heat input in one of the iSticks can heat the phonon detector and vice versa. Thus, it has to be ensured that while setting up one channel the other one is stabilized at a constant temperature, i.e. is heated with a constant current input in the heater. As both channels, the phonon and the iStick channel, experience an additional heat input from the other channel the transition temperature of these detectors should be well above the temperature of the heat bath. Otherwise it can happen that a thermometer is heated above its transition temperature by a heat input from the other channel.



(a) Event with an energy deposition of ~ 10 keV in the absorber crystal.

(b) Event with an energy deposition of ~ 70 keV in one iStick.

Figure 7.6: Pulses recorded with TUM26-b of events occurring in the absorber crystal (a) and in one iStick (b). In (a) an e^-/γ -event with an energy of ~ 10 keV deposited in the absorber crystal is shown. While the phonon detector shows a large pulse (red), no pulse is visible in the iSticks (green). The corresponding light signal is depicted in blue. In the event shown in (b) an energy of ~ 70 keV was deposited in one iStick. The light produced in the iStick is detected by the light detector (blue) and, additionally, a pulse in the phonon detector (red) with an energy of ~ 1 keV is recorded.

7.4.2 Signal of the iStick Channel

An energy deposition in one phonon detector holding stick is detected by a signal in the stick TES and by a degraded signal in the phonon channel. For an energy deposition in the absorber crystal the situation is reverted. Therefore, the ratio of the two signals can be used for a discrimination of any type of event occurring in the sticks.

A typical e^-/γ -event with an energy deposition of ~ 10 keV occurring in the absorber crystal is shown in figure 7.6a. It exhibits a large signal in the phonon detector (red) and additionally a smaller corresponding signal in the light detector (blue). No pulse is visible in the iStick channel (green), which means that too few phonons are transmitted to the iSticks to produce a measurable signal. In figure 7.6b an energy deposition of ~ 70 keV in one iStick is shown. For the calibration of the iSticks the module was equipped with several ^{55}Fe sources, so that each stick is in line-of-sight with one source. In this event the pulse of the iStick channel (green) is largest, while the light produced in the iStick is detected by the light detector (blue). Due to phonons transmitted in the absorber crystal, also a small signal in the phonon detector is visible (red). This pulse corresponds to an energy of ~ 1 keV measured in the phonon detector.

This shows that energy depositions occurring in the iSticks and in the absorber crystal can be distinguished by the ratio of pulse heights in the different detectors. Most events occurring in the sticks can be distinguished by their light signal since for such events more light is detected. However, events occurring due to a surface α -contamination of the stick can produce a nuclear recoil in the sticks and transfer phonons in the absorber crystal but they produce only a very small light signal. Such events can only be vetoed by the signal of the iStick channel.

The relation of the pulse heights measured in both detectors is investigated in figure

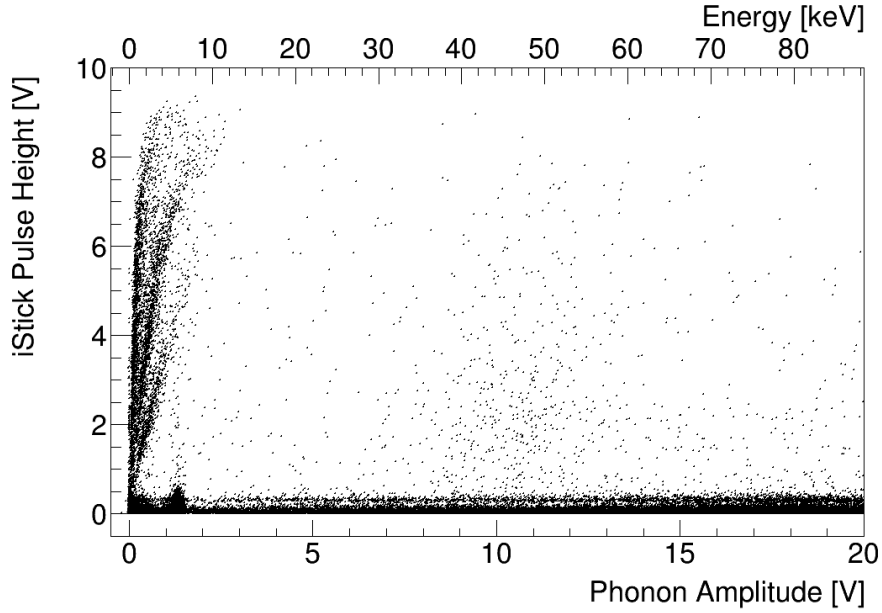


Figure 7.7: Measured iStick pulse height against amplitude measured in the phonon detector TUM26-b. Amplitudes measured with the phonon detector of up to 20 V corresponding to an energy of ~ 90 keV are displayed. Different populations of events can be observed. Energy depositions occurring in the absorber crystal appear at an iStick pulse height of $\lesssim 0.1$ V. Events in the iSticks appear at high iStick pulse heights and simultaneously a small energy signal in the phonon detector of $\lesssim 2$ V (corresponding to ~ 9 keV) is recorded. The few events with a high signal in both detectors are random coincidences.

7.7. While for the phonon detector the amplitude determined in the template fit is shown (x-axis), for the iStick channel the pulse height parameter is drawn (y-axis) instead of the amplitude, as the latter depends on the pulse shape of the individual iStick. The pulse height parameter is the maximum of the record shaped by a moving average filter with a width of 50 samples and, thus, independent of the actual pulse shape. Different populations are visible: Most events exhibit a small pulse height in the iStick channel ($\lesssim 1$ V) while featuring a pulse height of any value in the phonon detector. These events are energy depositions occurring in the absorber crystal. Even for energies well above the ROI for dark matter search ($\gtrsim 10$ V), no signal above threshold is produced in the iStick channel. The events exhibiting a small pulse height in the phonon detector ($\lesssim 2$ V corresponding to ~ 9 keV) combined with any pulse height in the iStick channel occurred in one of the iSticks⁵.

7.4.3 Energy Threshold and Resolution of the iStick Channel

In figure 7.8 the pulse height spectrum measured in the iStick channel is depicted. To reduce the influence of events occurring in the phonon detector only events with an

⁵The few events with a large signal in the iSticks as well as the phonon detector are random coincidences, where usually the signals occur at a different time in the record window.

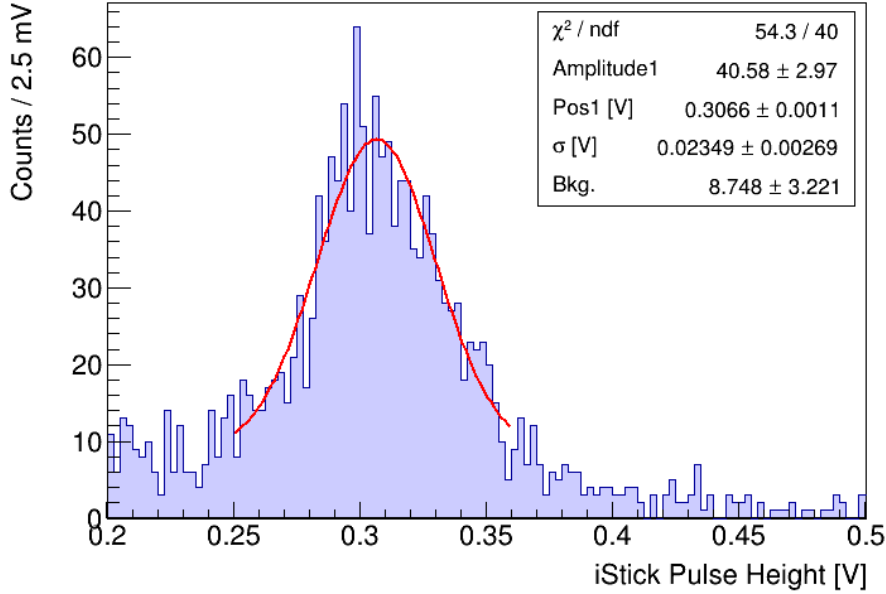


Figure 7.8: Spectrum of particle pulses in the iStick channel measured in run 126, whereby only events with an energy below threshold measured in the phonon detector are shown. Only one peak appears at a pulse height of ~ 0.3 V from the three ^{55}Fe sources irradiating the iSticks. For a rough calibration the spectrum is fitted with one Gaussian function (red line).

energy below threshold measured in the phonon detector are displayed. Also here the pulse height parameter is shown on the x-axis.

As mentioned before, all three iSticks are irradiated with an ^{55}Fe source. Therefore, it is expected that each iStick TES exhibits a double-peak structure in its spectrum and in the total spectrum of the iStick channel up to three double peak structures could be observed. However, only one broad peak is visible at a pulse height of ~ 0.3 V in the measured spectrum. Thus, the difference of the pulse heights for a certain energy deposition in the three iSticks cannot be resolved with the given resolution. This indicates that in this energy range the iSticks have a similar energy scale. However, from the peak it cannot be concluded on the physical resolution of the iStick channel, as the observed peak might be broadened due to slightly different positions of the three peak structures. Due to this the calibration of the iSticks has a rather high uncertainty.

As a separation of the different expected peaks is not possible the observed structure is fitted with a single Gaussian function (red). The fit yields a mean of (306.6 ± 1.1) mV and a resolution of $\sigma = (23.5 \pm 2.7)$ mV which corresponds to a resolution of $\sigma^E = (452.2 \pm 51.9)$ eV.

The determined baseline resolution of the veto channel is $\sigma_{S,0} = (13.92 \pm 0.22)$ mV which corresponds to $\sigma_{S,0}^E = (270.59 \pm 4.28)$ eV (see appendix A). A higher noise level is expected in this channel compared to a single detector as three detectors are contributing to the noise. With this baseline resolution the 5σ energy threshold is determined to be $E_{thr} = (1.35 \pm 0.02)$ keV. The rejection of iStick events is investigated in the following.

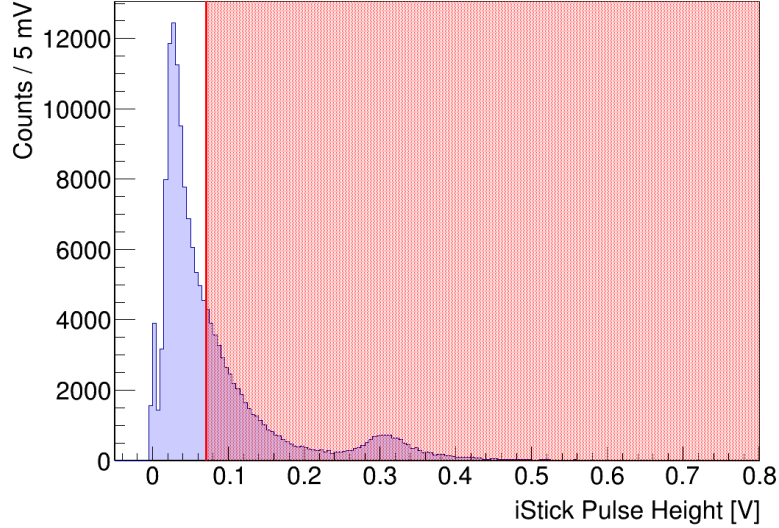


Figure 7.9: Spectrum of particle pulses measured in the iStick channel in run 126. At low pulse heights a large peak due to events occurring in the absorber crystal is visible. The small peak at a pulse height of ~ 0.3 V appears due to the ^{55}Fe sources in line-of-sight with the iSticks. The red line indicates the cut value of 71 mV (corresponding to an energy of 1.34 keV). All events above are rejected by the iStick cut (red-shaded area).

7.4.4 Discrimination of Events Occurring in the iSticks

In figure 7.7 it is shown that events occurring in the absorber crystal with energies of $\lesssim 100$ keV do not result in a measurable signal in the iStick channel. Therefore, within the present work an one-dimensional cut on the iStick pulse height is performed to veto events occurring in the iSticks. The pulse height spectrum of all particle pulses measured in the iStick channel is shown in figure 7.9. All events with a pulse height measured in the iSticks of more than the value of the 5σ threshold (71 mV corresponding to 1.35 keV, red line) are rejected (red-shaded area). In total $\sim 40\%$ of all events recorded are removed by this cut.

With the cut on the iStick signal all events with an energy above the iStick channel threshold $E_{thr,S}$ are rejected. Thus, with this cut all events with a ratio of energy measured in the iStick channel E_S and energy measured in the phonon detector E_P

$$\frac{E_S}{E_P} \geq \frac{E_{thr,S}}{E_P} = \frac{1.35 \text{ keV}}{E_P} \quad (7.2)$$

are vetoed. This corresponds to a ratio of pulse height measured in the iStick channel P_S and pulse height measured in the phonon channel P_P of

$$\frac{P_S}{P_P} \geq \frac{P_{thr,S}}{P_P} = \frac{71 \text{ mV}}{P_P}. \quad (7.3)$$

The relation of the signals measured in the iStick and in the phonon channel is investigated in figure 7.10. The ratio of pulse heights measured in the iStick and in the phonon channel is shown against the energy measured in the phonon detector for

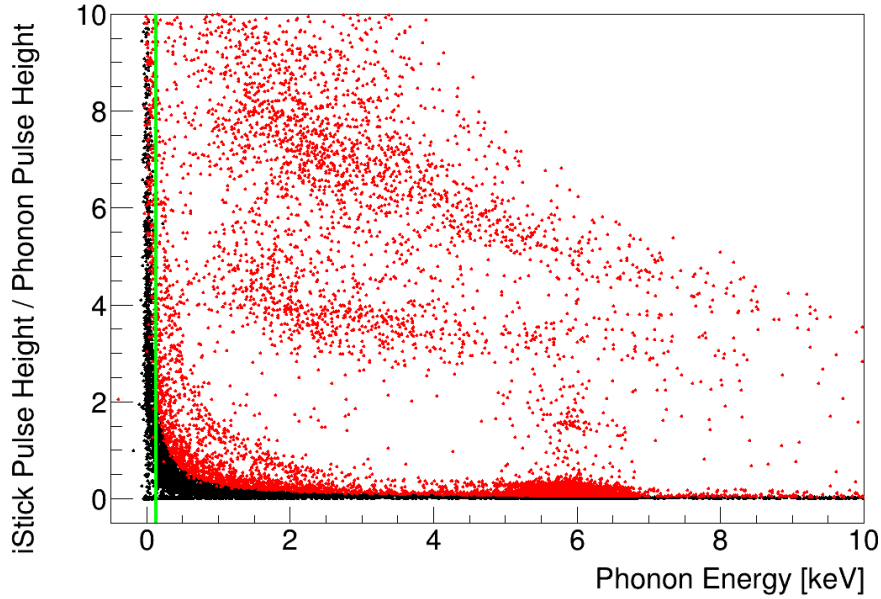


Figure 7.10: Ratio of pulse height measured in the iStick channel and pulse height measured in the phonon channel versus energy measured in the phonon channel. Events occurring in the absorber crystal are depicted in black. Events rejected in the iStick cut are marked in red. The green line marks the energy threshold of the phonon detector of $E_{thr,P} = 0.136$ keV.

each event. Thereby, events surviving the iStick cut are marked in black, while events rejected by this cut are drawn in red. The energy threshold of the phonon detector of $E_{thr,P} = 0.136$ keV is marked in green. Events occurring in the absorber crystal exhibit a very small pulse height in the iStick channel and, thus, appear in a population very small pulse height ratio.

As in figure 7.7 also in figure 7.10 the different bands of iStick events are visible. They appear in a nearly horizontal population at a pulse height ratio of $\gtrsim 3$. To reject all events with a pulse-height ratio of $\gtrsim 3$ down to threshold, an iStick threshold of ≤ 101 mV (corresponding to an energy threshold of ≤ 1.9 keV) is necessary. With the iStick threshold reached in the measurement of 71 mV (corresponding to an energy threshold of 1.34 keV) all events with a pulse height ratio of 2.2 are rejected down to threshold. Thus, in this measurement the bands of iStick events can be removed down to threshold.

However, many events also appear between the population of absorber events and iStick events. These can be random coincidences of energy depositions in an iStick and in the absorber crystal but they can also arise from Compton scatters. In an underground setup such as the main CRESST setup a lower rate and, thus, less coincidences are expected. With data obtained in the CRESST setup further investigation is possible to determine the origin of these events.

For dark matter search the expected rate of possible signal events is small and, therefore, the cut should remove as few events as possible. A more elaborated cut e.g.

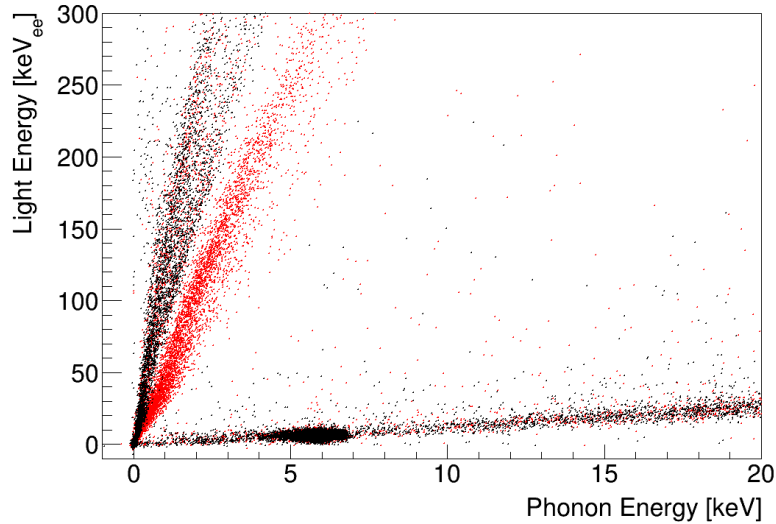


Figure 7.11: Energy measured in the light detector against energy measured in phonon detector TUM26-b. Events rejected in the iStick cut (see figure 7.9) are colored in red, while events surviving this cut are drawn as black points. The events that are removed in the cut on the iStick pulse height are mainly located in one band with a larger signal in the light channel compared to the lower band of black dots, which is the e^-/γ -band. The band of black dots with an even larger signal in the light channel are energy depositions in the CaWO_4 sticks holding the light detector.

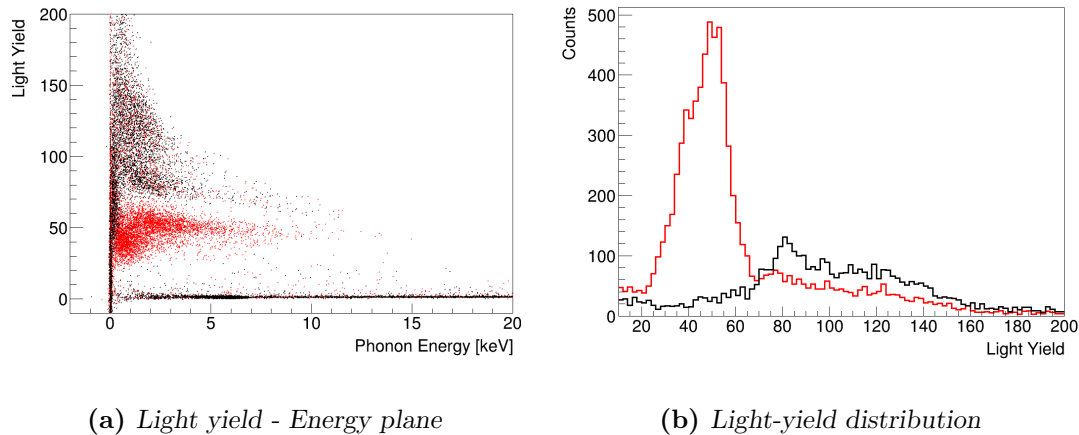
including the time difference of the pulse onset⁶, might be required. However, within the present analysis the efficiency of this cut is not relevant.

7.4.5 Light Signal of Stick Events

Events occurring in the CaWO_4 sticks also produce scintillation light. In figure 7.11 the energy measured in the light detector is depicted against the energy measured in the phonon detector for the low-energy region of TUM26-b. Events rejected by the cut on the iStick pulse height are colored in red, while events surviving this cut are drawn as black points. The band with the smallest slope is the e^-/γ -band consisting of energy depositions in the absorber. The iStick events appear in a band with a larger slope (red). However, a population of events with an even larger light signal survives this cut. These events can be attributed to energy depositions in the light detector holding sticks and are discussed in section 7.4.7.

In figure 7.12a all events are shown in the light yield - energy plane. The e^-/γ -band appears at a light yield of one. The iStick events appear in a roughly horizontal band expanding until an energy of ~ 14 keV. For energies above ~ 150 eV they are well separated from the e^-/γ -band. However, at low energies the bands overlap due to the

⁶Random coincidences of an event occurring in the absorber crystal and in one iStick happen more likely at different times in the record. However, in the cut exploited in the present work such records are rejected. A cut rejecting only events with pulses in both channels that occur within a short time period would maintain these records.



(a) Light yield - Energy plane

(b) Light-yield distribution

Figure 7.12: Similar to figure 7.11 events rejected in the iStick cut (see figure 7.9) are colored in red, while surviving this cut are drawn in black. In (a) all events are shown in the light yield - energy plane. The events in the iSticks are located at a light yield of ~ 30 – 60 and are well separated from the e^-/γ -band at a light yield of 1 for phonon energies above ~ 150 eV. At higher light yields of ~ 80 – 150 a broad band of events in the light detector holding sticks is located. In (b) a histogram of the light-yield distribution of all events is depicted. The red histogram illustrates the light yield distribution of events with a pulse height above the threshold of the iStick channel, while the black histogram shows the light yield distribution of events with a pulse height below the iStick channel threshold.

finite energy resolution of the detectors. This shows that for e^-/γ -events occurring in the holding sticks the signal in the light detector is a good discrimination parameter especially for high energies.

In figure 7.12b the light yield distribution of these events is displayed. The events rejected by the iStick cut (red) appear mainly at a light yield of ~ 30 – 60 , i.e. ~ 30 – 60 times more light is detected compared to events occurring in the absorber crystal. Also here a distribution of events not rejected by the iStick cut appears at higher light yields of > 70 .

7.4.6 Discrimination of the individual iSticks

It is observed that the pulse shape of different detectors slightly varies despite the same geometry and the same production process. The three iStick thermometers measured in the present work were produced on the same silicon wafer and processed simultaneously (see chapter 6). The pulse shapes observed in the iStick channel are investigated in the following.

In figure 7.13 the decay time parameter of all iStick events is shown against the pulse height measured in the iStick channel. The decay time parameter is calculated by the analysis software and describes the time of a pulse necessary to decay from the maximum sample to $1/e$ of the total pulse height. For pulse heights $\gtrsim 1$ V (corresponding to an energy of ~ 20 keV) three clearly separated populations are visible in the decay time parameter calculated for the pulses measured in the iStick channel. For smaller pulse heights a high noise contribution increases the uncertainty of the decay time parameter.

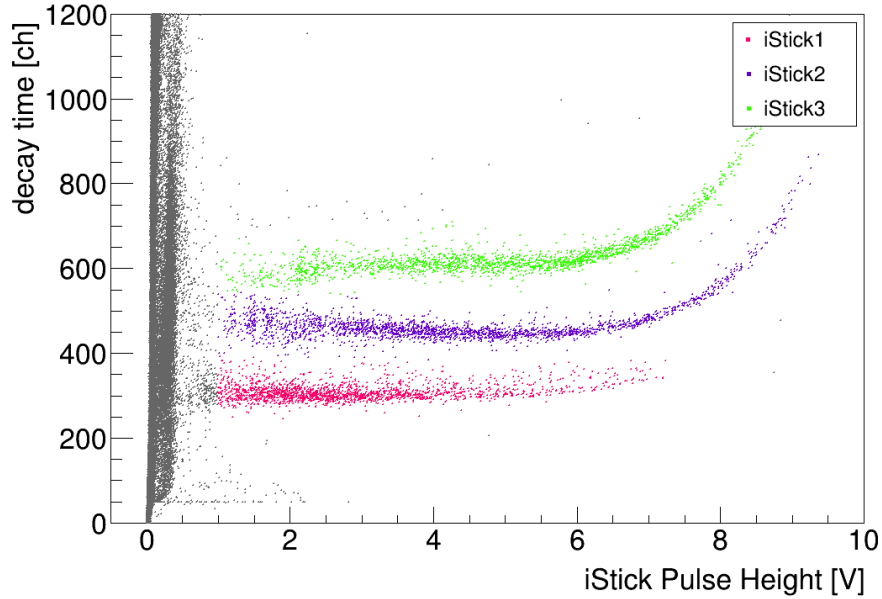


Figure 7.13: Decay time parameter of *iStick* events versus the pulse height measured in the *iStick* channel. For pulse heights above ~ 1 V (corresponding to an energy of ~ 20 keV) three populations can be discriminated. In total 1798 events are marked in magenta, 2176 events in violet and 1889 in green. The similar number hints that the energy scale of the three *iSticks* is roughly similar.

A more elaborated pulse-shape analysis⁷ might improve the discrimination for smaller pulse heights.

The three populations are marked in colors for pulse heights $\gtrsim 1$ V. They contain a similar amount of events of 1798 events (magenta), 2176 events (violet) and 1889 events (green). This hints that the energy scale of the three *iSticks* is roughly similar.

For each distribution a standard event is produced from pulses with a pulse height of ~ 3 V and is shown in figure 7.14. The standard events of the three different populations are well distinguishable by eye. They slightly differ in their rise time ($\tau_{n,1} = 0.4$ ms, $\tau_{n,2} = 0.6$ ms, $\tau_{n,3} = 0.7$ ms) and strongly in their decay time ($\tau_{film,1} = 2.7$ ms, $\tau_{film,2} = 4.4$ ms, $\tau_{film,3} = 8.8$ ms). The differences are explainable by discrepancies in the thermal couplings. A difference in the glue spot connecting the TES-carrier to the CaWO_4 stick can cause a difference in the rise time. The decay time can be influenced by differences in the thermal coupling to the heat bath, which varies due to differences in the bonding process of the gold wire providing the thermal coupling. Moreover, the thermal coupling between the stick and the holder can vary, due to a difference in the pressure of the clamp pressing the stick against the absorber crystal.

The amplitude of a pulse determined in the template fit depends on the template

⁷Several parameters can be used to distinguish pulses with different shapes. In CRESST-II phase 2 a pulse-shape analysis has been performed to distinguish pulses from the main absorber crystal and the TES-carrier. The discrimination power of several single parameters as well as a pulse-shape analysis based on artificial neural networks was investigated in [76].

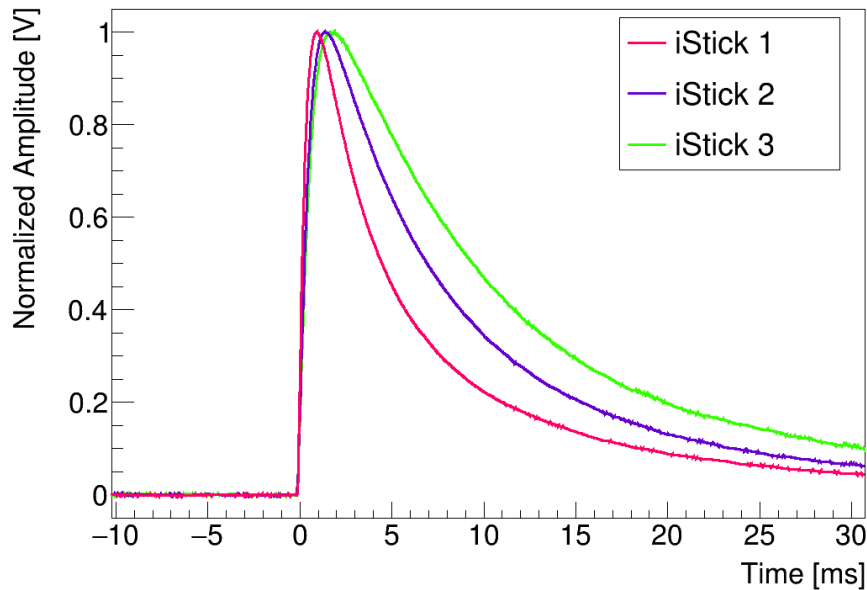


Figure 7.14: Template pulses of the three iSticks with an amplitude normalized to one. Each standard event is generated from one of the three populations visible in figure 7.13 of pulses with a pulse height of ~ 0.3 V. A clear difference in the pulse shape can be seen. The rise time differs slightly ($\tau_{n,1} = 0.4$ ms, $\tau_{n,2} = 0.6$ ms, $\tau_{n,3} = 0.7$ ms), while the decay time varies strongly ($\tau_{film,1} = 2.7$ ms, $\tau_{film,2} = 4.4$ ms, $\tau_{film,3} = 8.8$ ms).

used. For this reason the correct amplitude can only be determined if pulses from the different sticks can be separated⁸. As it is not necessary to know the exact amplitude in a veto channel, the pulse height parameter can be used as estimator for the amplitude.

In figure 7.15 the pulse height measured in the iStick channel against the amplitude measured in the phonon detector is shown for all events. The events are colored according to figure 7.14 for iStick pulse heights of $\gtrsim 1$ V, so that the events occurring in each stick are shown in different colors. Events of each iStick appear in a wide distribution with the largest density occurring in two bands. This means that for a certain energy deposited in one iStick a different amount of energy is transferred into the phonon detector. This can be explained by a difference in the thermal coupling of different parts of the stick. The feedthrough of the housing for the sticks couples the middle of the stick to the housing and, thus, to the heat bath. For this reason, phonons produced in the part of the stick inside the housing are more likely to be transferred into the absorber crystal than in the iStick TES. In contrast, phonons produced in the outer part of the stick are more likely to be transferred into the iStick TES than in the absorber crystal. In conclusion, it seems that events occurring close to the absorber crystal transfer a larger amount of energy in the absorber crystal compared to events

⁸A fit with different templates is also a method to discriminate events with different pulse shapes. Typically, the RMS from the fit is low if the template describes the pulse shape well. When a pulse is fitted with different templates, the template that results in the smallest RMS value is the best estimator for the true pulse shape.

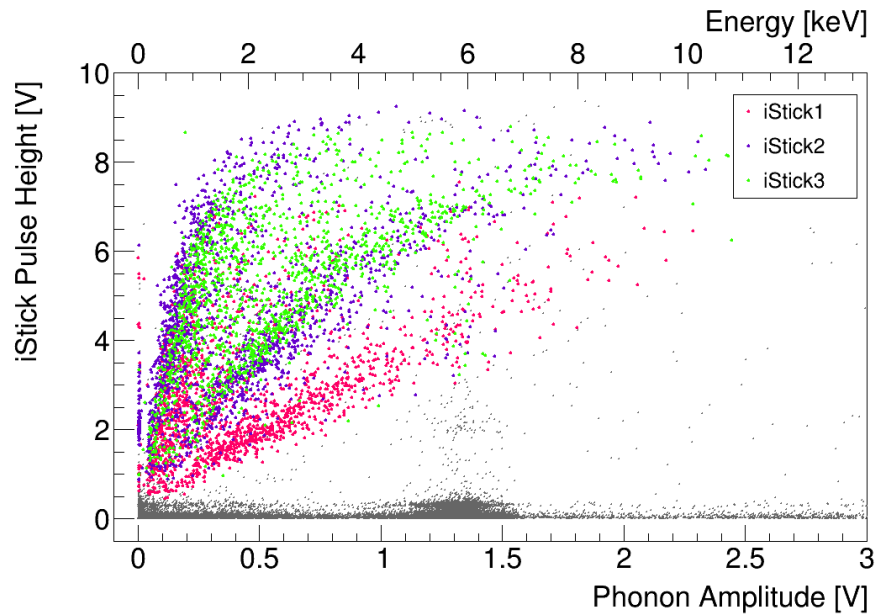


Figure 7.15: Distribution of events of the respective iSticks. The same events as in figure 7.11 are shown here but with different colors. The iStick events are colored as the respective populations shown in figure 7.13. While the distribution of events of the two iSticks with the longer decay times overlap (green and violet), the distribution of the iStick 1 (magenta) is observed at lower pulse heights in the iStick channel. All three distributions of the respective iSticks seem to appear in two bands, which probably correspond to events occurring inside or outside the housing. All events which could not be attributed to one iStick are shown in gray color.

close to the TES-carrier.

The distributions of two iSticks overlap (iStick 2 in violet and iStick 3 in green), while the distribution of iStick 1 (magenta) appears at smaller pulse heights measured in the iStick channel. The reason for this can be either a worse performance of one iStick thermometer or a difference in the transfer of phonons into the absorber crystal, e.g. due to a different pressure between the absorber crystal and one iStick.

In contrast to the phonon signal, there is no visible difference in the light signal of events in the three iSticks. It seems that the produced photons are distributed more evenly in the stick than the phonons after an energy deposition.

It is not necessary to discriminate the individual detectors of the iStick channel to act as a veto channel. However, these results demonstrate that it is possible to discriminate events from several detectors operated with only one SQUID. A more sophisticated analysis of the pulse shape might discriminate events occurring in the different iSticks to even lower energies. Such an analysis is possible with CRESST-III data as it exhibits a smaller pile-up component.

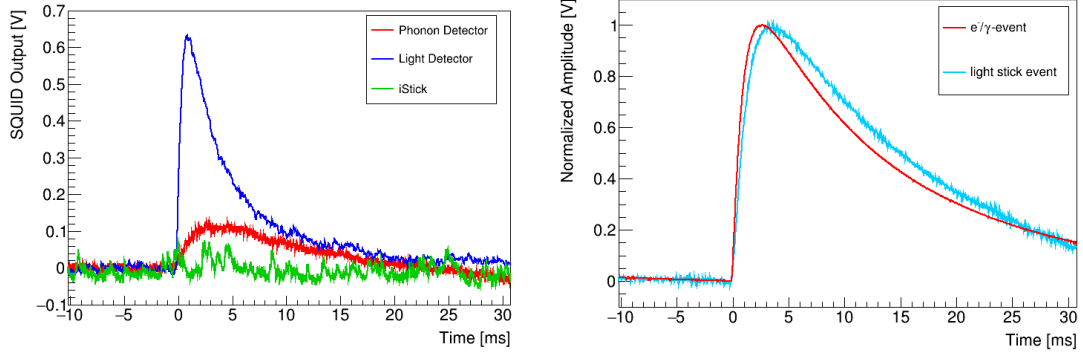
7.4.7 Light Detector Holding Sticks

After removing events occurring in the iSticks by a cut on the iStick pulse height, a band of events with a high signal in the light channel remains (see figure 7.11). As can be seen in figure 7.12a these events features a large light signal and appears at light yields of $\gtrsim 70$.

A typical record of this population is shown in figure 7.16a. No signal is visible in the iStick channel since otherwise this event would be rejected in the cut on the iStick pulse height. However, a large light signal and a small signal in the phonon detector are visible. A more precise view on the pulse shape observed in the phonon detector reveals that it is slightly different compared to pulses from absorber events (see figure 7.16b). The template of the population with high light yield (light blue) is slower compared to the template of absorber events (red) with a light yield of one. In the light detector no difference in the pulse shape is observed.

These observations hint that these events are energy depositions in non-active but scintillating part of the module. The only non-active and scintillating parts are the light detector holding sticks and the reflective foil surrounding the detectors. Events in the foil produce less light than events occurring in the absorber crystal [63]. Therefore, these events must be occurring in the light detector holding sticks. On the one hand such events produce a light signal (just as events occurring in the iSticks) and, additionally, they can transfer phonons into the light absorber. Moreover, a small signal is observed in the phonon detector, which is attributed to light absorbed either by its crystal or by its sensitive TES.

The difference in the pulse-shape observed in the phonon channel is caused by the scintillation time of CaWO_4 ($\tau_s \approx 400 \mu\text{s}$ [103]) that slows down the energy input in the phonon detector thermometer. The resulting pulse shape is expected to be a convolution of the pulse shape of the phonon detector and the scintillating component. However, with the present measurement this is hard to investigate quantitatively due to the large pile-up component. With data taken in the main CRESST setup it should be possible to investigate this with an appropriate model of the pulse shape.



(a) Record of an event occurring in the light detector holding sticks (b) Standard templates of the phonon detector

Figure 7.16: Events occurring in the light detector holding sticks are characterized by a large light signal and a small signal in the phonon detector, while no signal in the iStick channel is visible (a). In (b) a comparison of standard templates of pulses measured in the phonon detector for events occurring in the absorber crystal (red) and in the light sticks (light blue) is shown. The difference in the pulse shape can be exploited in a pulse-shape analysis.

In figure 7.17a the light energy against the phonon energy of events remaining after the cut on the iStick pulse height are shown. The events in the remaining band are marked in blue⁹. The same events are shown in the light yield - energy plane in figure 7.17b. It can be seen that the light stick events are distributed at a light yield of more than ~ 30 and mainly at light yields of $\sim 70 - 150$. For energies above ~ 100 eV they are well separated of the e^-/γ -band and, thus, can be discriminated via the signal in the light detector. However, at very low energies they might leak to lower light yields. In the present measurement the light stick events can be rejected by the light signal down to an energy of ~ 100 eV.

Further investigation is necessary to determine if it is necessary to improve the discrimination. The difference in the pulse shape can be exploited in a pulse-shape analysis to distinguish events occurring in the light detector holding sticks to even lower energies. Another possibility is to instrument the light detector holding sticks as well with a TES for an enhanced discrimination.

7.5 Summary

The measurements discussed in the present work exhibit large uncertainties mainly induced by the high rate occurring in the detector in a setup above ground. Despite the high rate it is possible to investigate the performance of all three channels (phonon, light and iStick channel) of the optimized module. It has been confirmed that all requirements for a measurement in the main CRESST setup are fulfilled. In the following the main results are summarized:

⁹The events visible at a phonon energy as well as a light energy of ~ 0 can mainly be attributed to noise triggers.

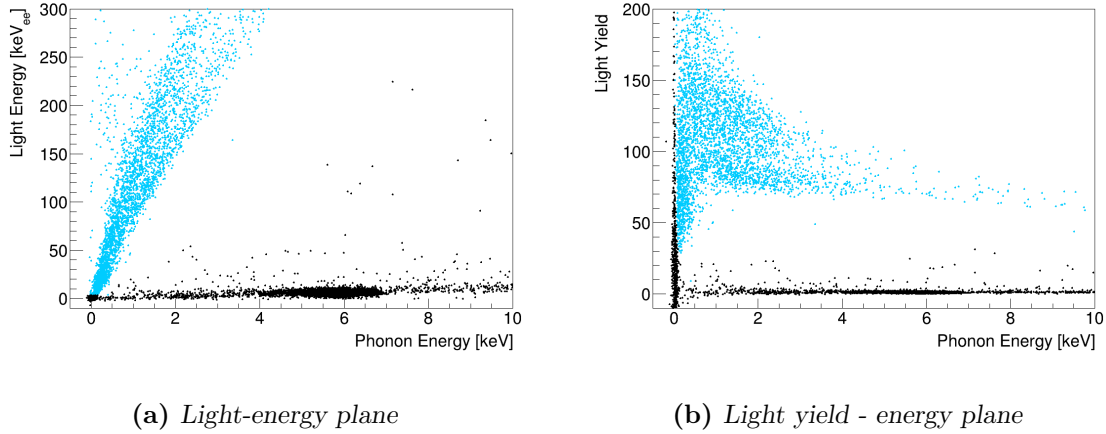


Figure 7.17: Low-energy region in the light-energy plane (a) and the light yield - energy plane of run 126. The events remaining after the application of the iStick cut are shown. Events appearing in the remaining band with a light energy of $\gtrsim 50$ eV are marked in blue in both figures. In the light yield - energy plane they appear at light yields $\gtrsim 30$ and can be separated down to an energy of ~ 100 eV.

- The phonon detector operated in the calorimetric mode is expected to reach a threshold of 16–60 eV in the CRESST setup, which is well below the design goal of 100 eV. With the investigation of the parameters for the thermalization of non-thermal phonons a further optimization might be in reach.
- For the light detector an improvement in the signal amplitude of a factor 6 – 7 compared to light detectors operated in CRESST-II phase 2 was expected due to the design changes in the optimized module. However, with the single light detector measured within the present work this was not observed. Due to the typically large range in the performance of light detectors further measurements are required to evaluate the influence of the design changes.
- The three iSticks were successfully operated in one readout channel. With a threshold of 1.35 keV the iStick channel is expected to be able to veto all events occurring in the iSticks including the dangerous background due to α -induced events.

In total, ten optimized detector modules have been mounted in the CRESST setup for CRESST-III phase 1. With future data obtained in the CRESST setup more detailed investigations are possible.

Chapter 8

Conclusion and Perspectives

The CRESST experiment aims to directly detect dark matter via nuclear recoils in a target material consisting of scintillating CaWO_4 crystals. The previous data taking phase CRESST-II phase 2 (2013-2015) demonstrated the outstanding potential of low-threshold CRESST detectors to explore the low-mass region of the parameter space for elastic spin-independent dark matter nucleon interaction. With the detector Lise an energy threshold of 307 eV was reached and a sensitivity for dark matter particles down to a mass of $0.5 \text{ GeV}/c^2$ was achieved. For dark matter particle masses of $\lesssim 1.7 \text{ GeV}/c^2$ a world leading exclusion limit was set.

The parameters determining the sensitivity of the CRESST experiment for low-mass dark matter are investigated in chapter 3. It is found that an enlargement of the exposure and a reduction of the observed background only play a minor role for the near future of CRESST. In contrast, a reduction of the phonon detector threshold to 100 eV or even lower can drastically increase the sensitivity to low-mass dark matter by more than four orders of magnitude. Moreover, it allows to investigate dark matter particle masses down to $\sim 0.1 \text{ GeV}/c^2$. To explore the low-mass dark matter region the CRESST collaboration recently started a new stage of the experiment, denoted as CRESST-III, in which phonon detectors with a threshold of $\lesssim 100 \text{ eV}$ are operated.

The main part of the present work describes the optimization of the detector modules for CRESST-III. This optimization is based on the design of the modules operated in CRESST-II. The latter consist of a phonon detector made of a scintillating CaWO_4 target crystal with a mass of $\sim 300 \text{ g}$ which is equipped with a sensitive thermometer. The measurement of the temperature change after an energy deposition is performed with transition edge sensors (TES). A separate light detector measures the scintillation light which allows to discriminate different event types on event-by-event basis. Both detectors, in combination referred to as detector module, are surrounded by a reflective and scintillating housing.

The thermal model that describes the signal formation in these detectors is explained in chapter 4. In addition to a precise knowledge of the signal, also the different noise sources must be considered. The dominant sources can be modeled to describe the total noise observed in CRESST detectors. For a better understanding of the phonon detector noise, its contributions measured in different setups are investigated and compared. While the noise observed in the CRESST setup is well described by the model, in the test setup, which is located above ground, an additional contribution at small frequencies is measured. The latter arises from the high rate observed in the test setup. Thus, the noise contribution strongly depends on the external event rate. As the measured signal is independent of the setup, it is possible to infer the performance expected in

the CRESST main setup from a measurement in the test setup.

For the optimization of the detectors the aim is to increase the signal compared to the signal of CRESST-II detectors without changing the parameters defining the noise. The dependence of the signal height on the geometry of the crystal is investigated in chapter 5. An enlargement of the phonon detector signal is achieved via a reduction of the crystal mass together with an optimized geometry and an adaption of the TES structure. The optimized phonon detector consists of a cuboidal shaped crystal with a mass of 24 g. Three different TES structures have been designed for an optimum detection of the signal in the new crystal geometry. Moreover, the change of the crystal geometry is expected to enlarge the signal in the light channel. On the one hand, the light output of the small crystal is enhanced and, on the other hand, an adjustment of the light detector geometry increases the signal measured in the light detector.

With a new geometry of the detectors also the housing needs to be adjusted. All components of the final design of the optimized module are described in chapter 6. In the new module both detectors, the phonon and the light detector, are held by scintillating CaWO_4 sticks pressed against them with bronze clamps located outside the housing. Together with the reflective and scintillating foil these sticks form a fully-scintillating housing, which effectively prevents nuclear recoil backgrounds of surface α -decays. However, with the aimed for low threshold of the new modules also an α -contamination of the stick surface, which is extended outside the housing, can cause a background in the region-of-interest for dark matter search. Phonons of a nuclear recoil occurring in the sticks can be transferred into the absorber crystal and produce a low-energetic event accompanied by little or no light signal. To veto such events, each of the three phonon detector holding sticks is instrumented with a TES similar to that of the light detector. The three instrumented sticks (called iSticks) of a module are read out in parallel in one readout channel.

First measurements with a prototype of the optimized detector module were performed in a test setup located above ground (see chapter 7). Two different phonon detectors were operated and energy thresholds of 136 eV and 195 eV were reached, respectively. Considering the much smaller noise contribution in the main CRESST setup, thresholds in the range of 16–60 keV are feasible. Moreover, an improved understanding of the detector physics was aimed for in these measurements. A comparison of a large ($A_t = 36 \text{ mm}^2$) and a small ($A_t = 19 \text{ mm}^2$) TES structure showed that the signal measured in the small structure is larger by 16 %. Moreover, it was possible to investigate the time constants describing the thermalization of non-thermal phonons in the phonon detector. The knowledge of these time constants is essential for a possible further optimization of the detector geometry. From these measurements the time constant for the thermalization of non-thermal phonons in the crystal was determined to be $\tau_{\text{crystal}} \approx 1.7 \text{ ms}$.

Furthermore, the performance of the light detector was investigated. With the single light detector that was measured, the expected improvements could not be confirmed. Due to the typically large range in the performance of light detectors, further tests are required to evaluate the influence of the design changes. Moreover, the three iStick TES were successfully operated in parallel in one readout channel. With an energy threshold of 1.35 keV reached with the iStick channel in the test setup it is possible to veto all events occurring in the iSticks. With the measurements of the prototypes it is

confirmed that all requirements for the optimized module are met and that the goals for the optimization are reached.

Due to the promising results obtained in the present work, ten of such modules have been mounted for CRESST-III phase 1. Based on the present work, with the data obtained in CRESST-III phase 1 the parameters of the new module can be determined precisely and important information can be gained:

- As the main goal of CRESST-III is to operate phonon detectors with a threshold of $\lesssim 100$ eV, the parameter of most interest is the threshold finally achieved in the CRESST setup. Within the CRESST setup the energy threshold of all installed phonon detectors can be measured directly.
- Within the present work two different TES structures for the phonon detector have been compared. The TES structures have a similar geometry but their area differs by a factor of ~ 2 . Both structures performed well in the measurements of the prototype module and, thus, both detector types have been installed in the CRESST setup. With data taken in the CRESST main setup it is possible to compare them with larger accuracy. In case it is confirmed that the small structure results in a larger signal, it might be worthwhile to investigate a further reduction of the TES area for future detectors.
- In the analysis of the measurements discussed in the present work, a simple one-dimensional cut on the iStick veto signal is performed. With cleaner data obtained in the main CRESST setup, the iStick channel can be investigated more detailed. This allows to increase the cut efficiency by including e.g. the time difference of the signal in the iStick channel and the phonon detector.
- In the present work it is assumed that the achievable threshold is the 5σ value of the baseline noise. With the hardware trigger used in CRESST-II the trigger threshold is adjusted once at the beginning of a measurement. For several detectors in CRESST-II phase 2 the trigger level was set at a higher value than the 5σ baseline noise, e.g. due to a time dependence of the noise. For CRESST-III a continuous readout has been implemented, so that the pulses can be located in the record with a software trigger (e.g. optimum filter [122]). This can possibly improve the trigger process and, thus, reduce the trigger threshold.

The measurement of the two prototypes of the optimized phonon detectors allowed for an improved understanding of the detector physics. With further optimizations of future detectors an even larger signal might be feasible. Based on the findings in the present work, the following measurements are suggested for the future:

- In the present measurements the collection of non-thermal phonons was influenced by the presence of phonon collectors. This might distort the parameters found for the thermalization of non-thermal phonons. A measurement with a dedicated detector without phonon collectors can increase the accuracy of the determined time constants. It is found that the derived time constants cannot be transferred for the two crystal geometries employed in CRESST. Additional measurements can disentangle the influence of the geometry and the surface of the crystal as well as the phonon collectors and, thus, can improve the existing model.

- The present phonon detectors in CRESST-III phase 1 are equipped with a thermometer operated in the calorimetric mode. This structure can possibly be optimized further, which allows for an even lower phonon detector threshold. Possible improvements are a reduction of the size of the thermometer or an adjustment of size of the phonon collectors.
- Within the present work also a TES structure for the bolometric mode has been designed. This structure is expected to yield a slightly smaller signal compared to the calorimetric TES structure but has advantages in the discrimination of energy depositions directly in the thermometer. An investigation of the bolometric structure allows to determine the resulting signal height and to balance the signal reduction against the discrimination power.

With the detectors developed in the present work an excellent sensitivity for low-mass dark matter is expected. With data collected in CRESST-III and in additional measurements further optimizations of the detectors for future measurement campaigns of CRESST are possible.

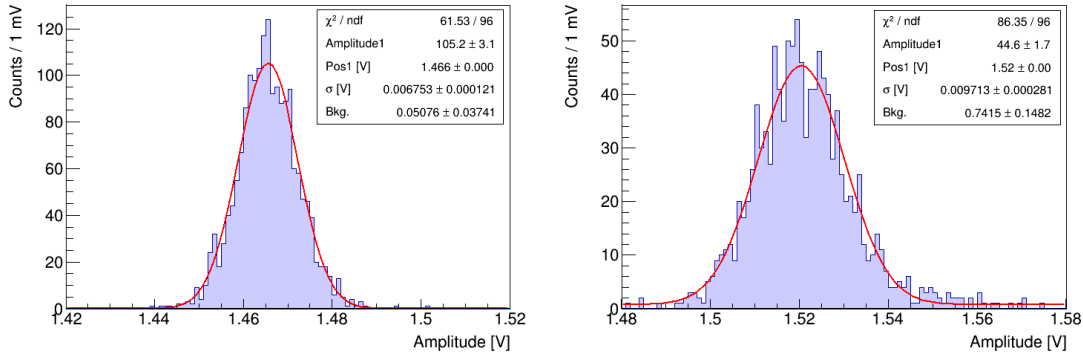
Appendix

Appendix A

Baseline Noise Determined with Artificial Pulses

Within the present work the baseline noise of a detector is determined from empty baselines, i.e. records triggered randomly by the DAQ. To determine the baseline noise a template pulse of fixed height is superimposed to these empty baselines and the resulting artificial pulse is fitted with the template [74]. The width σ of the resulting Gaussian peak in the amplitude distribution is determined. It equals the baseline noise, since only the baseline noise contributes to the uncertainty of the pulse height.

In the measurements of the prototype detector modules in the test setup in Munich (see in chapter 7) the baseline noise was determined for all detectors. The spectra of artificial pulses and the fits are shown in the following figures. For the phonon detectors TUM26-b and TUM56-f a baseline noise of $\sigma_{P,0} = (6.75 \pm 0.12)$ mV (see figure A.1a) and $\sigma_{P,0} = (9.71 \pm 0.28)$ mV (see figure A.1b) was determined, respectively. The baseline noise of the light detector was derived to be $\sigma_{L,0} = (8.64 \pm 0.17)$ mV (see figure A.2) and for the iStick channel a baseline noise of $\sigma_{S,0} = (13.92 \pm 0.22)$ mV results (see figure A.3).



(a) Spectrum of artificial pulses in TUM26-b (b) Spectrum of artificial pulses in TUM56-f

Figure A.1: Amplitude spectra of template pulses superimposed to empty baselines in the phonon detectors TUM26-b. The best fit of a Gaussian function and a constant background to the spectrum is shown in red.

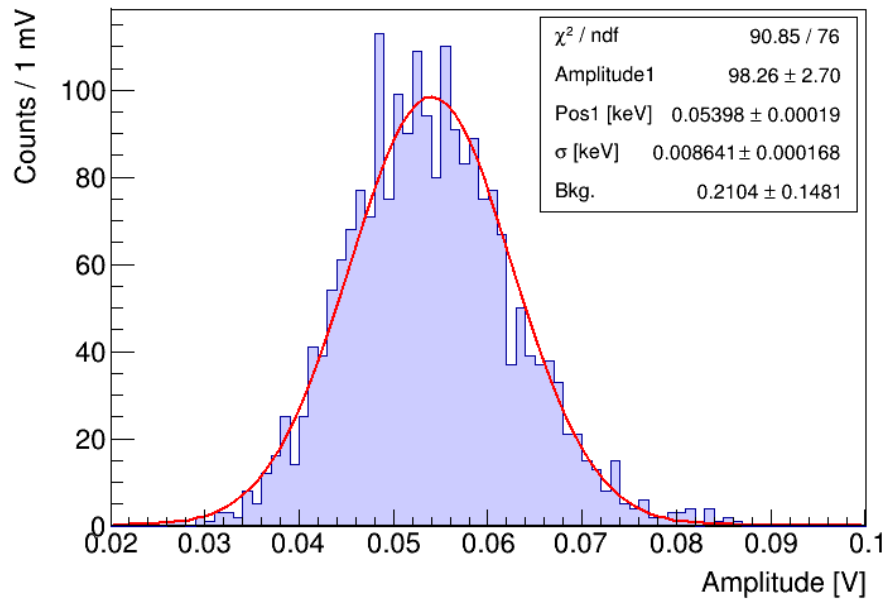


Figure A.2: Amplitude spectra of template pulses superimposed to empty baselines in the light detector WI-531/2. The best fit of a Gaussian function and a constant background to the spectrum is shown in red.

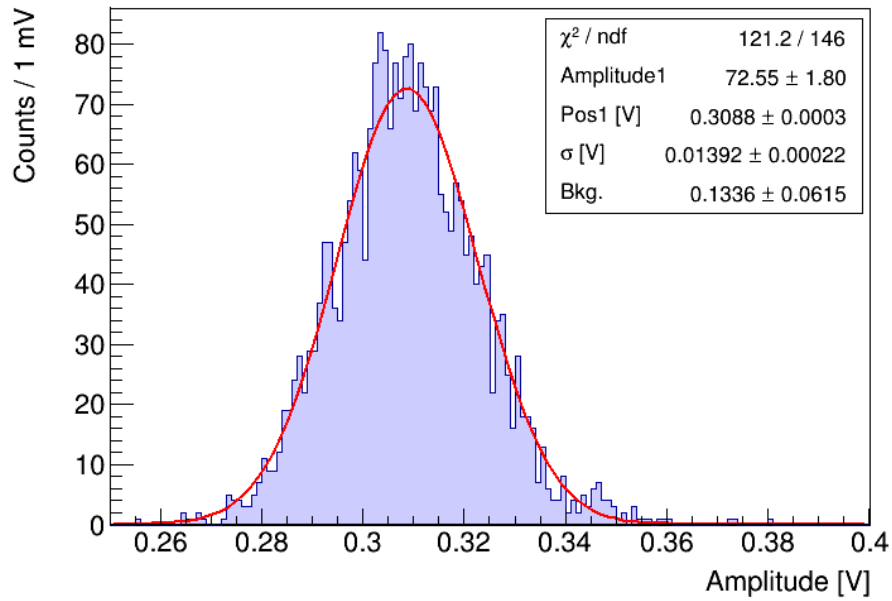


Figure A.3: Amplitude spectra of template pulses superimposed to empty baselines in the iStick channel. The best fit of a Gaussian function and a constant background to the spectrum is shown in red.

Appendix B

Parametrization of the Recoil Bands

Typically, CRESST data is displayed in the light yield - energy plane (see figure B.1a). Different types of particle events appear in roughly horizontal bands. Although, this is the common way to illustrate the data, the parametrization of the recoil bands as used in [71, 76] is described in the light - energy parameter space, where the energy measured in the light detectors L is plotted against the recoil energy E_R (see figure B.1b). In this plane the different event types appear in bands with different slopes. Basically, these bands are defined by a mean, which describes the average amount of light produced, and an energy-dependent width, which is caused by the finite detector resolution. The detector specific parameters of the bands are determined in a likelihood fit. With the knowledge of the quenching factors, with these parameters also the quenched bands can be calculated.

In the following a basic overview of the description of the e^-/γ -band is given. Details on the parametrization as well as the likelihood fit can be found in [70, 71, 76].

The mean of the e^-/γ -band is described by the function

$$L^{e^-/\gamma}(E_R) = (L_0 E_R + L_1 E_R^2) \left[1 - L_2 \exp\left(-\frac{E_R}{L_3}\right) \right], \quad (\text{B.1})$$

with the total energy deposited in the absorber crystal E_R . In first approximation the scintillator is linear, which is described by the leading term $L_0 E_R$. Due to the calibration procedure electrons and gammas have a light yield of around one and, for this reason, also the parameter $L_0 \approx 1$. The second term $L_1 E_R^2$ allows for a deviation from linearity, which is typically found to be small. This term usually is only relevant when a large energy range of > 100 keV is considered.

At small energies the mean light yield of the band drops due to the scintillator non-proportionality-effect [90]. This drop depends on the crystal of the respective detector and typically observed for energies below ~ 10 keV. This effect is taken into account by the second factor. The parameters L_2 and L_3 describe the magnitude and the typical energy scale, respectively.

The width of the band depends on the finite resolution of phonon and light detector. Typically the phonon detector resolution is much better than the one of the light detector and, thus, the latter mainly contributes to the width. Therefore, for simplicity the width of the e^-/γ -band σ is modeled only as a function of the detected light energy L , instead of the total recoil energy E_R . It is parametrized as:

$$\sigma^{e^-/\gamma}(L) = \sqrt{S_0 + S_1 L + S_2 L^2}. \quad (\text{B.2})$$

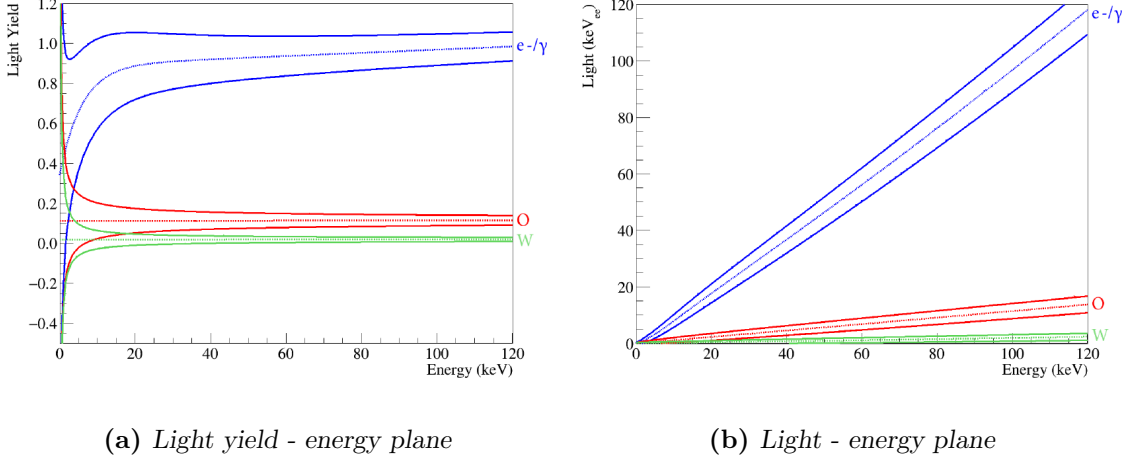


Figure B.1: Recoil bands with the same parameters for e^-/γ -events (blue), recoils off oxygen (red) and tungsten (green) shown in the light yield - energy plane (a) and in the light - energy plane (b). The dashed lines show the mean of each band, while the solid lines correspond to the 90% upper and lower boundaries. Image taken from [71].

In case the phonon detector resolution is significantly better than the light detector resolution, it is valid to assume that $\sigma^{e^-/\gamma}(L)$ is the resolution of the light detector. Thereby, the three parameters S_i describe the different effects causing a broadening of the amount of measured light. The parameter S_0 accounts for the energy-independent baseline noise of the light detector. The parameter S_1 describes the uncertainty due to the statistical fluctuation in the number of detected photons. Other uncertainties that are proportional to the amount of light produced (e.g. possible position dependencies of the light output from the crystal [117]) are taken into account by the parameter S_2 . This parameter is usually small and can be neglected.

In general, also the finite resolution of the phonon detector σ_P has to be taken into account in addition to the light detector resolution σ_L . Approximately, the resolutions of both detectors are statistically independent and, thus, the width of the band can be described as:

$$\sigma^{e^-/\gamma}(L) = \sqrt{\sigma_L^2(L) + [QF_{e^-/\gamma} \cdot \sigma_P(E)]^2}, \quad (\text{B.3})$$

with the quenching factor of the e^-/γ -band $QF_{e^-/\gamma}$. In chapter 2 the quenching factor was described to be constant over a large part of the ROI for dark matter search. However, with low energy thresholds, the energy dependency of the quenching factor observed at low energies has to be considered. For electron recoils the quenching factor is described by the second factor of equation B.1 [81]:

$$QF_{e^-/\gamma}(E_R) = \left[1 - L_2 \exp\left(-\frac{E_R}{L_3}\right) \right]. \quad (\text{B.4})$$

As the consideration of the phonon detector resolution is usually only a small correction, the energy dependency is dropped. This results in an energy-independent resolution of the phonon detector corresponding to the baseline noise $\sigma_{P,0}$. Thus, the energy-independent part of bandwidth can be described by $S_0 = \sigma_{P,0}^2 + \sigma_{L,0}^2$. To improve the convergence of the fit of the e^-/γ -band, the parameter S_0 is usually fixed to

Parameter	Value
L_0	0.978
L_1 [keV ⁻¹]	0*
L_2	0.343
L_3 [keV]	8.888
S_0 [keV ² _{ee}]	0.0667*
S_1 [keV _{ee}]	0.561
S_2	0*

Table B.1: Values for the parameters describing the position of the e^-/γ -band in the light - energy plane for TUM40. The parameters marked with * have been fixed in the fit.

the value derived from the baseline noise of the phonon detector $\sigma_{P,0}$ and the one of the light detector $\sigma_{L,0}$.

To properly describe the e^-/γ -band another class of events has to be considered. In many detectors it is found that especially at low energies events with a light yield higher than expected appear. These events originate most likely due to external electrons penetrating the module and, thereby, producing scintillation light in the foil before being absorbed in the crystal [71]. In this way, more light, than from an interaction in the crystal alone, is produced. Therefore, these events are called *excess light events*. The formal description used to account for the excess light events is discussed in [70].

All free parameters are determined by using a maximum likelihood fit. The values of the parameters for TUM40 determined within the present work are given in table B.1. The parameter S_0 is determined directly from the baseline noise of the phonon and the light detector and fixed in the fit. Moreover, the parameter L_1 and S_2 are typically observed to very small and, thus, are fixed to 0 in the fit. The parameters are in agreement with the values derived in [71, 76].

Bibliography

- [1] Planck Collaboration, R. Adam *et al.*, Planck 2015 results. I. Overview of products and scientific results, *A&A***594**, A1 (2016), arXiv:1502.01582.
- [2] F. Zwicky, Die Rotverschiebung von extragalaktischen Nebeln, *Helvetica Physica Acta* **6**, 110 (1933).
- [3] E. Corbelli, Dark matter and visible baryons in M33, *Mon. Not. Roy. Astron. Soc.* **342**, 199 (2003), arXiv:astro-ph/0302318.
- [4] P. R. Hague and M. I. Wilkinson, The Degeneracy of M33 Mass Modeling and Its Physical Implications, *ApJ***800**, 15 (2015), arXiv:1408.4452.
- [5] D. Clowe *et al.*, A direct empirical proof of the existence of dark matter, *Astrophys. J.* **648**, L109 (2006), arXiv:astro-ph/0608407.
- [6] D. Harvey, R. Massey, T. Kitching, A. Taylor, and E. Tittley, The non-gravitational interactions of dark matter in colliding galaxy clusters, *Science* **347**, 1462 (2015), arXiv:1503.07675.
- [7] Planck Collaboration, Map of CMB temperature from SMICA, 2015, <http://www.cosmos.esa.int/web/planck/picture-gallery>.
- [8] D. J. Fixsen, The Temperature of the Cosmic Microwave Background, *ApJ***707**, 916 (2009), arXiv:0911.1955.
- [9] G. Bertone, D. Hooper, and J. Silk, Particle dark matter: Evidence, candidates and constraints, *Phys. Rept.* **405**, 279 (2005), arXiv:hep-ph/0404175.
- [10] Planck Collaboration, Ade, P. A. R. *et al.*, Planck 2015 results. XIII. Cosmological parameters, *A&A***594**, A13 (2016), arXiv:1502.01589.
- [11] SDSS, D. G. York *et al.*, The Sloan Digital Sky Survey: Technical Summary, *Astron. J.* **120**, 1579 (2000), arXiv:astro-ph/0006396.
- [12] V. Springel *et al.*, Simulating the joint evolution of quasars, galaxies and their large-scale distribution, *Nature* **435**, 629 (2005), arXiv:astro-ph/0504097.
- [13] V. Springel *et al.*, The large-scale structure of the Universe, *Nature* **440**, 1137 (2006).
- [14] Particle Data Group, K. A. Olive *et al.*, Review of Particle Physics, *Chin. Phys.* **C38**, 090001 (2014).

- [15] J. L. Feng, Dark Matter Candidates from Particle Physics and Methods of Detection, *ARA&A* **48**, 495 (2010), arXiv:1003.0904.
- [16] B. W. Lee and S. Weinberg, Cosmological lower bound on heavy-neutrino masses, *Physical Review Letters* **39**, 165 (1977).
- [17] K. Petraki and R. R. Volkas, Review of asymmetric dark matter, *Int. J. Mod. Phys.* **A28**, 1330028 (2013), arXiv:1305.4939.
- [18] K. M. Zurek, Asymmetric Dark Matter: Theories, Signatures, and Constraints, *Phys. Rept.* **537**, 91 (2014), arXiv:1308.0338.
- [19] T. Cohen, D. J. Phalen, A. Pierce, and K. M. Zurek, Asymmetric Dark Matter from a GeV Hidden Sector, *Phys. Rev.* **D82**, 056001 (2010), arXiv:1005.1655.
- [20] R. D. Peccei and H. R. Quinn, Constraints imposed by CP conservation in the presence of pseudoparticles, *Phys. Rev. D* **16**, 1791 (1977).
- [21] M. Klasen, M. Pohl, and G. Sigl, Indirect and direct search for dark matter, *Prog. Part. Nucl. Phys.* **85**, 1 (2015), arXiv:1507.03800.
- [22] W. B. Atwood *et al.*, The Large Area Telescope on the Fermi Gamma-Ray Space Telescope Mission, *ApJ* **697**, 1071 (2009), arXiv:0902.1089.
- [23] HESS, A. Abramowski *et al.*, Constraints on an Annihilation Signal from a Core of Constant Dark Matter Density around the Milky Way Center with H.E.S.S., *Phys. Rev. Lett.* **114**, 081301 (2015), arXiv:1502.03244.
- [24] F. Halzen and D. Hooper, The indirect search for dark matter with IceCube, *New Journal of Physics* **11**, 105019 (2009), arXiv:0910.4513.
- [25] J. Conrad, Indirect Detection of WIMP Dark Matter: a compact review, in *Interplay between Particle and Astroparticle physics London, United Kingdom, August 18-22, 2014*, 2014, arXiv:1411.1925.
- [26] Y. Zhao and K. M. Zurek, Indirect Detection Signatures for the Origin of Asymmetric Dark Matter, *JHEP* **07**, 017 (2014), arXiv:1401.7664.
- [27] D. G. Cerdeño and A. M. Green, *Direct detection of WIMPs* (Cambridge University Press, 2010), p. 347.
- [28] J. Lewin and P. Smith, Review of mathematics, numerical factors, and corrections for dark matter experiments based on elastic nuclear recoil, *Astroparticle Physics* **6**, 87 (1996).
- [29] J. Bovy and S. Tremaine, On the Local Dark Matter Density, *ApJ* **756**, 89 (2012), arXiv:1205.4033.
- [30] F. Donato, N. Fornengo, and S. Scopel, Effects of galactic dark halo rotation on WIMP direct detection, *Astropart. Phys.* **9**, 247 (1998), arXiv:hep-ph/9803295.

-
- [31] R. H. Helm, Inelastic and elastic scattering of 187-mev electrons from selected even-even nuclei, *Phys. Rev.* **104**, 1466 (1956).
- [32] J. Engel, Nuclear form factors for the scattering of weakly interacting massive particles, *Physics Letters B* **264**, 114 (1991).
- [33] F. J. Kerr and D. Lynden-Bell, Review of galactic constants, *MNRAS***221**, 1023 (1986).
- [34] M. C. Smith *et al.*, The RAVE survey: constraining the local Galactic escape speed, *MNRAS***379**, 755 (2007), arXiv:astro-ph/0611671.
- [35] K. Freese, J. Frieman, and A. Gould, Signal modulation in cold-dark-matter detection, *Phys. Rev. D* **37**, 3388 (1988).
- [36] P. Cushman *et al.*, Working Group Report: WIMP Dark Matter Direct Detection, in *Community Summer Study 2013: Snowmass on the Mississippi (CSS2013) Minneapolis, MN, USA, July 29-August 6, 2013*, 2013, arXiv:1310.8327.
- [37] LUX, D. S. Akerib *et al.*, Improved Limits on Scattering of Weakly Interacting Massive Particles from Reanalysis of 2013 LUX Data, *Phys. Rev. Lett.* **116**, 161301 (2016), arXiv:1512.03506.
- [38] E. Aprile *et al.*, Dark Matter Results from 225 Live Days of XENON100 Data, *Physical Review Letters* **109**, 181301 (2012), arXiv:1207.5988.
- [39] XENON1T, E. Aprile, The XENON1T Dark Matter Search Experiment, *Springer Proc. Phys.* **148**, 93 (2013), arXiv:1206.6288.
- [40] C. E. Aalseth *et al.*, CoGeNT: A search for low-mass dark matter using p-type point contact germanium detectors, *Phys. Rev. D***88**, 012002 (2013), arXiv:1208.5737.
- [41] C. E. Aalseth *et al.*, Maximum Likelihood Signal Extraction Method Applied to 3.4 years of CoGeNT Data, *ArXiv e-prints* (2014), arXiv:1401.6234.
- [42] CDEX, Q. Yue *et al.*, Limits on light WIMPs from the CDEX-1 experiment with a p-type point-contact germanium detector at the China Jinping Underground Laboratory, *Phys. Rev. D***90**, 091701 (2014), arXiv:1404.4946.
- [43] CDMS, R. Agnese *et al.*, Silicon Detector Dark Matter Results from the Final Exposure of CDMS II, *Phys. Rev. Lett.* **111**, 251301 (2013), arXiv:1304.4279.
- [44] SuperCDMS Collaboration, R. Agnese *et al.*, Search for Low-Mass Weakly Interacting Massive Particles with SuperCDMS, *Phys. Rev. Lett.* **112**, 241302 (2014).
- [45] SuperCDMS, R. Agnese *et al.*, New Results from the Search for Low-Mass Weakly Interacting Massive Particles with the CDMS Low Ionization Threshold Experiment, *Phys. Rev. Lett.* **116**, 071301 (2016), arXiv:1509.02448.
- [46] R. Bernabei *et al.*, New results from DAMA/LIBRA, *Eur. Phys. J. C* **67**, 39 (2010), arXiv:1002.1028.

- [47] J. Cherwinka *et al.*, First data from DM-Ice17, *Phys. Rev. D* **90**, 092005 (2014), arXiv:1401.4804.
- [48] PICO, C. Amole *et al.*, Dark Matter Search Results from the PICO-2L C₃F₈ Bubble Chamber, *Phys. Rev. Lett.* **114**, 231302 (2015), arXiv:1503.00008.
- [49] A. Gütlein *et al.*, Impact of coherent neutrino nucleus scattering on direct dark matter searches based on CaWO₄ crystals, *Astropart. Phys.* **69**, 44 (2015), arXiv:1408.2357.
- [50] MACRO, M. Ambrosio *et al.*, Vertical muon intensity measured with MACRO at the Gran Sasso Laboratory, *Phys. Rev.* **D52**, 3793 (1995).
- [51] C. Arpesella, Background measurements at Gran Sasso Laboratory, *Nuclear Physics B - Proceedings Supplements* **28**, 420 (1992).
- [52] A. Alessandrello *et al.*, Measurements of internal radioactive contamination in samples of Roman lead to be used in experiments on rare events, *Nuclear Instruments and Methods in Physics Research Section B: Beam Interactions with Materials and Atoms* **142**, 163 (1998).
- [53] Belli, P. and Bernabei, R. and d'Angelo, S. and de Pascale, M.P. and Paoluzi, L. and Santonico, R. and Taborogna, N. and Iucci, N. and Villorresi, G., Deep underground neutron flux measurement with large BF₃ counters, *Il Nuovo Cimento A (1965-1970)* **101**, 959 (1989).
- [54] B. Majorovits *et al.*, Production of low-background CuSn₆-bronze for the CRESST dark-matter-search experiment, *Applied Radiation and Isotopes* **67**, 197 (2009).
- [55] K. Pretzl, Cryogenic calorimeters in astrophysics and particle physics, *Nucl. Instrum. Meth.* **A454**, 114 (2000), arXiv:hep-ex/9911028.
- [56] Pobell, F., *Matter and Methods at Low Temperatures*, 3rd ed. (Springer, 2007).
- [57] M. Kiefer, *Improving the Light Channel of the CRESST-II Dark Matter Detectors*, PhD thesis, Technische Universität München, 2012.
- [58] Y. Zdesenko *et al.*, Scintillation properties and radioactive contamination of CaWO₄ crystal scintillators, *Nuclear Instruments and Methods in Physics Research Section A: Accelerators, Spectrometers, Detectors and Associated Equipment* **538**, 657 (2005).
- [59] J. Ninkovic, *Investigation of CaWO₄ Crystals for Simultaneous Phonon-Light Detection in the CRESST Dark Matter Search*, PhD thesis, Technische Universität München, 2005.
- [60] I. Bavykina, *Investigation of ZnWO₄ and CaMoO₄ as target materials for the CRESST-II Dark Matter Search*, PhD thesis, Ludwig-Maximilians-Universität München, 2009.

-
- [61] K. Zimmermann, *Study of Zinc Tungstate as Target Material for Cryogenic Dark Matter Search*, Master's thesis, Julius-Maximilians-Universität Würzburg, 2012.
- [62] R. Kleindienst, *Light Yield Measurements of Cadmium Tungstate and Titanium Doped Sapphires for the CRESST Dark Matter Search*, Diploma thesis, Technische Universität München, 2010.
- [63] K. Schäffner, *Study of Backgrounds in the CRESST Dark Matter Search*, PhD thesis, Technische Universität München, 2013.
- [64] C. Arnaboldi *et al.*, CdWO₄ scintillating bolometer for Double Beta Decay: Light and heat anticorrelation, light yield and quenching factors, *Astroparticle Physics* **34**, 143 (2010), arXiv:1005.1239.
- [65] P. Meunier *et al.*, Discrimination between nuclear recoils and electron recoils by simultaneous detection of phonons and scintillation light, *Appl. Phys. Lett.* **75**, 1335 (1999), arXiv:physics/9906017.
- [66] P. Huff, *The Detector Parameters Determining the Sensitivity of the CRESST-II Experiment*, PhD thesis, Technische Universität München, 2010.
- [67] CRESST-II, G. Angloher *et al.*, Results on low mass WIMPs using an upgraded CRESST-II detector, *Eur. Phys. J.* **C74**, 3184 (2014), arXiv:1407.3146.
- [68] R. Strauss *et al.*, Energy-dependent light quenching in CaWO crystals at mK temperatures, *Eur. Phys. J. C* **74**, 2957 (2014), arXiv:1401.3332.
- [69] R. Strauss, *Energy-Dependent Quenching Factor Measurements of CaWO₄ Crystals at mK Temperatures and Detector Prototypes for Direct Dark Matter Search with CRESST*, PhD thesis, Technische Universität München, 2013.
- [70] J. Schmalzer, *The CRESST Dark Matter Search - New Analysis Methods and Recent Results*, PhD thesis, Technische Universität München, 2010.
- [71] F. Reindl, *Exploring Light Dark Matter With CRESST-II Low-Threshold Detectors*, PhD thesis, Technische Universität München, 2016.
- [72] J. Magill, G. Pfennig, and J. Galy, *Karlsruher Nuklidkarte*, 7th ed. (, 2006).
- [73] G. Angloher *et al.*, Results from 730 kg days of the CRESST-II Dark Matter search, *Eur. Phys. J. C* **72**, 1971 (2012), arXiv:1109.0702.
- [74] CRESST, G. Angloher *et al.*, Results on light dark matter particles with a low-threshold CRESST-II detector, *Eur. Phys. J.* **C76**, 25 (2016), arXiv:1509.01515.
- [75] S. Henry *et al.*, The 66-channel SQUID readout for CRESST II, *Journal of Instrumentation* **2**, P11003 (2007).
- [76] A. Zöller, *Artificial Neural Network Based Pulse-Shape Analysis for Cryogenic Detectors Operated in CRESST-II*, PhD thesis, Technische Universität München, 2016.

- [77] A. Münster *et al.*, Radiopurity of CaWO₄ crystals for direct dark matter search with CRESST and EURECA, *JCAP* **1405**, 018 (2014), arXiv:1403.5114.
- [78] M. Kuźniak, M. G. Boulay, and T. Pollmann, Surface roughness interpretation of 730 kg days CRESST-II results, *Astroparticle Physics* **36**, 77 (2012), arXiv:1203.1576.
- [79] CUORE, D. R. Artusa *et al.*, Searching for neutrinoless double-beta decay of ¹³⁰Te with CUORE, *Adv. High Energy Phys.* **2015**, 879871 (2015), arXiv:1402.6072.
- [80] M. Sievers, *Optimizing Detectors for Dark Matter Search*, Diploma thesis, Technische Universität München, 2010.
- [81] CRESST, R. Strauss *et al.*, A detector module with highly efficient surface-alpha event rejection operated in CRESST-II Phase 2, *Eur. Phys. J.* **C75**, 352 (2015), arXiv:1410.1753.
- [82] A. Erb and J.-C. Lanfranchi, Growth of high-purity scintillating CaWO₄ single crystals for the low-temperature direct dark matter search experiments CRESST-II and EURECA, *CrystEngComm* **15**, 2301 (2013).
- [83] CRESST, R. Strauss *et al.*, Beta/gamma and alpha backgrounds in CRESST-II Phase 2, *JCAP* **1506**, 030 (2015), arXiv:1410.4188.
- [84] CRESST, G. Angloher *et al.*, Probing low WIMP masses with the next generation of CRESST detector, (2015), arXiv:1503.08065.
- [85] T. Marrodán Undagoitia and L. Rauch, Dark matter direct-detection experiments, *J. Phys.* **G43**, 013001 (2016), arXiv:1509.08767.
- [86] S. Yellin, Finding an upper limit in the presence of an unknown background, *Phys. Rev. D* **66**, 032005 (2002).
- [87] S. Yellin, Extending the optimum interval method, ArXiv e-prints (2007), arXiv:0709.2701.
- [88] F. Pröbst, private communication, 2016.
- [89] W. Moses, S. Payne, W.-S. Choong, G. Hull, and B. Reutter, Scintillator non-proportionality: Present understanding and future challenges, *Nuclear Science, IEEE Transactions on* **55**, 1049 (2008).
- [90] R. F. Lang *et al.*, Scintillator Non-Proportionality and Gamma Quenching in CaWO₄, ArXiv e-prints (2009), arXiv:0910.4414.
- [91] A. Münster, PhD thesis, Technische Universität München, in preparation.
- [92] E. Pantic, *Performance of Cryogenic Light Detectors in the CRESST-II Dark Matter Search*, PhD thesis, Technische Universität München, 2008.

-
- [93] F. Pröbst *et al.*, Model for cryogenic particle detectors with superconducting phase transition thermometers, *Journal of Low Temperature Physics* **100**, 69 (1995).
- [94] M. Gluyas, F. D. Hughes, and B. W. James, The elastic constants of calcium tungstate, 4.2-300 K, *Journal of Physics D: Applied Physics* **6**, 2025 (1973).
- [95] C. Kittel, *Introduction to Solid State Physics*, 8th ed. (John Wiley and Sons, 2005).
- [96] B. Triplett, N. Phillips, T. Thorp, D. Shirley, and W. Brewer, Critical field for superconductivity and low-temperature normal-state heat capacity of tungsten, *Journal of Low Temperature Physics* **12**, 499 (1973).
- [97] J. Bardeen, L. N. Cooper, and J. R. Schrieffer, Theory of Superconductivity, *Phys. Rev.* **108**, 1175 (1957).
- [98] J. S. Shier and D. M. Ginsberg, Superconducting transitions of amorphous bismuth alloys, *Phys. Rev.* **147**, 384 (1966).
- [99] J. Liu and N. Giordano, Electron-phonon scattering times in thin Sb films, *Phys. Rev. B* **43**, 3928 (1991).
- [100] J. F. DiTusa, K. Lin, M. Park, M. S. Isaacson, and J. M. Parpia, Role of phonon dimensionality on electron-phonon scattering rates, *Phys. Rev. Lett.* **68**, 1156 (1992).
- [101] A. Pippard, Cxxii. ultrasonic attenuation in metals, *The London, Edinburgh, and Dublin Philosophical Magazine and Journal of Science* **46**, 1104 (1955).
- [102] J. Rothe, *Achieving Low Thresholds: Cryogenic Detectors for Low-Mass Dark Matter Searches*, Master's thesis, Ludwig-Maximilians-Universität München, 2016.
- [103] V. B. Mikhailik, H. Kraus, S. Henry, and A. J. B. Tolhurst, Scintillation studies of CaWO_4 in the millikelvin temperature range, *Phys. Rev. B* **75**, 184308 (2007).
- [104] K. D. Irwin, An application of electrothermal feedback for high resolution cryogenic particle detection, *Applied Physics Letters* **66**, 1998 (1995).
- [105] M. Kurakado, Possibility of high resolution detectors using superconducting tunnel junctions, *Nuclear Instruments and Methods in Physics Research* **196**, 275 (1982).
- [106] M. Loidl, *Diffusion und Einfang von Quasiteilchen*, PhD thesis, Ludwigs-Maximilians-Universität München, 1999.
- [107] G. Angloher *et al.*, Quasiparticle Diffusion in CRESST Light Detectors, *Journal of Low Temperature Physics* **184**, 323 (2016).
- [108] J. C. Mather, Bolometer noise: nonequilibrium theory, *Appl. Opt.* **21**, 1125 (1982).

- [109] S. H. Moseley, J. C. Mather, and D. McCammon, Thermal detectors as x-ray spectrometers, *Journal of Applied Physics* **56**, 1257 (1984).
- [110] A. Tanzke, *Optimization of Light Detectors for the CRESST experiment*, Diploma thesis, Technische Universität München, 2011.
- [111] R. F. Voss and J. Clarke, $\frac{1}{f}$ Noise from Systems in Thermal Equilibrium, *Phys. Rev. Lett.* **36**, 42 (1976).
- [112] J. Pelz and J. Clarke, Dependence of $\frac{1}{f}$ Noise on Defects Induced in Copper Films by Electron Irradiation, *Phys. Rev. Lett.* **55**, 738 (1985).
- [113] D. M. Fleetwood and N. Giordano, Direct link between $1/f$ noise and defects in metal films, *Phys. Rev. B* **31**, 1157 (1985).
- [114] D. M. Fleetwood and N. Giordano, Effect of strain on the $\frac{1}{f}$ noise of metal films, *Phys. Rev. B* **28**, 3625 (1983).
- [115] M. Galeazzi and D. McCammon, A microcalorimeter and bolometer model, *J. Appl. Phys.* **93**, 4856 (2003), arXiv:astro-ph/0304397.
- [116] P. Gorla, C. Bucci, and S. Pirro, Complete elimination of 1k pot vibrations in dilution refrigerators, *Nuclear Instruments and Methods in Physics Research Section A: Accelerators, Spectrometers, Detectors and Associated Equipment* **520**, 641 (2004), Proceedings of the 10th International Workshop on Low Temperature Detectors.
- [117] M. von Sievers, *Scintillating CaWO₄ Crystals for the Direct Dark Matter Search Experiments CRESST and EURECA*, PhD thesis, Technische Universität München, 2014.
- [118] A. Langenkämper, *Increase of Light Detection Efficiency for Future Cryogenic Rare Event Searches*, Master's thesis, Technische Universität München, 2016.
- [119] R. Strauß, Measurement done at MPP, 2015.
- [120] J. Astrom *et al.*, Fracture Processes Observed with A Cryogenic Detector, *Phys. Lett.* **A356**, 262 (2006), arXiv:physics/0504151.
- [121] Firestone, F. et al., *Table of Isotopes*, 8th ed. (John Wiley and Sons, 1999).
- [122] G. Piperno, S. Pirro, and M. Vignati, Optimizing the energy threshold of light detectors coupled to luminescent bolometers, *JINST* **6**, P10005 (2011), arXiv:1107.5679.

Acknowledgments

An dieser Stelle möchte ich mich bei allen Personen bedanken, die diese Arbeit möglich gemacht haben. Zuallererst möchte ich mich bei Prof. Allen Caldwell bedanken, der es mir ermöglicht hat, diese Arbeit in der CRESST Gruppe anzufertigen.

Bei Dr. Franz Pröbst möchte ich mich für die konstante Unterstützung und das Erklären jedes noch so kleinen Details bedanken. Danke, dass du dir trotz jeder Menge anderer Arbeit für meine Fragen Zeit genommen hast.

Vielen Dank an Dr. Raimund Strauß, ohne dessen Überblick über alle Entwicklungen und das gleichzeitige Organisieren jedes noch so kleinen Details für die neuen Detektoren diese Arbeit nicht möglich gewesen wäre. Auch für das Interesse und das Lesen der Arbeit möchte ich mich bedanken.

Bei Dr. Karoline Schöffner und Dr. Federica Petricca möchte ich mich bedanken, dass ich insbesondere während der gemeinsamen Zeit im Reinraum in der Zusammen- und Einbauphase für Run33 viel über die Handhabung von Detektoren gelernt habe. Dr. Patrick Huff möchte ich dafür danken, dass er mir während meiner Diplomarbeitszeit alles über Kryostaten und Messungen darin beigebracht hat.

Ein besonderer Dank geht auch an Dieter Hauff für die Hilfe beim Produzieren von Detektoren und auch für die Betreuung von allen technischen Geräten, die es erst ermöglicht, dass vieles so reibungslos funktioniert. Danke auch an Marc Wüstrich, der mit mir an mehreren Kryostaten gearbeitet hat und mich jederzeit bei allen Kryostatenproblemen unterstützt hat.

Danke an Dr. Wolfgang Seidl für den realistischen Einblick in die Welt der Wissenschaft sowie für viele praktische Tipps. Bei meinem Bürokollegen Nahuel Ferreira möchte ich mich für das gute Arbeitsklima bedanken. Danke auch für die Hilfe bei den Messungen und das Kabeldesign für das neue Modul. Danke an Dr. Florian Reindl für den technischen Support und besonders für das Programm FloP, das gar kein Flop sondern ein Hit ist ;-)

Bei Dr. Godehard Angloher möchte ich mich für die vielen kreativen und spannenden Ideen bedanken, die mich dazu motivierten Neues auszuprobieren. Danke an Dr. Achim Gütlein für das kurzfristige Berechnen des neutrino floors für kleine Massen. Vielen Dank an Dr. Antonio Bento für das Lesen eines Teils dieser Arbeit und für alle hilfreichen Kommentare.

Danke an Andrea Münster und das Kristalllabor der TUM für das Ziehen und das Bearbeiten der Kristalle. Auch bei allen Mitarbeitern der Werkstatt des Max-Planck-Instituts, die an der Produktion der vielen Teile für das Modul mitgewirkt haben, möchte ich mich bedanken. Ein besonderer Dank geht dabei an Walter Kosmale, der auch kurzfristig viele Ideen ermöglicht hat.

Bei allen anderen neuen und ehemaligen Mitgliedern der CRESST Gruppe am Max-Planck-Institut möchte ich mich für die Gespräche in den Kaffeepausen und das gute

Arbeitsklima bedanken. Auch allen anderen Mitgliedern der CRESST Kollaboration möchte ich für die gute Zusammenarbeit danken.

Ein ganz besonderer Dank geht an meine Eltern für die bedingungslose Unterstützung und die Geduld, ohne die vieles nicht möglich gewesen wäre.

Andi, du hast mich in so vielerlei Hinsicht unterstützt, dass es unmöglich wäre alles aufzuzählen. Daher schreibe ich hier nur das Wichtigste: Danke, dass du dein Leben mit mir teilst!